Genetically Engineered Sensors for Non-Invasive Molecular Imaging using MRI

by

Mikhail G. Shapiro

B.Sc. Neuroscience
Brown University, 2004

Submitted to the Department of Biological Engineering in partial fulfillment of the requirements for the degree of

Doctor of Philosophy in Biological Engineering
at the
Massachusetts Institute of Technology

September 2008

Signature of Author: ______________________________
Department of Biological Engineering
July 21, 2008

Certified by: ______________________________
Alan P. Jasanoff
Associate Professor of Biological Engineering,
Nuclear Science & Engineering and Brain & Cognitive Science
Thesis Co-supervisor

Certified by: ______________________________
Robert S. Langer
Institute Professor
Thesis Co-supervisor

Accepted by: ______________________________
Alan J. Grodzinsky
Professor of Electrical, Mechanical and Biological Engineering
Chairman, Graduate Program Committee

This thesis has been examined by a committee of the Biological Engineering Department as follows:

Chairperson, Graduate Thesis Committee _____

Angela Belcher
Germeshausen Professor of Materials Science & Engineering
and Biological Engineering

Thesis Co-supervisor, Committee Member _____

Alan P. Jasanoff
Associate Professor of Biological Engineering,
Nuclear Science & Engineering and Brain & Cognitive Science
Thesis Co-supervisor

Thesis Co-supervisor, Committee Member _____

Robert S. Langer
Institute Professor

Abstract

Technologies that provide information about the concentrations or activities of specific molecules in living subjects have the potential to greatly advance science and medicine. Magnetic resonance imaging (MRI) is a tool uniquely suited to this task because of its ability to image deep inside tissues at relatively high spatial and temporal resolution. However, the range of molecular phenomena currently accessible to MRI is limited by a lack of suitable molecular sensors. Most efforts to create such sensors have focused on synthetic contrast agents, whose complicated structures make them difficult to engineer, synthesize and deliver to target tissues. If MRI sensors could instead be made of proteins, a number of these difficulties could be mitigated. Here, we describe two platforms for the development of protein-based molecular sensors for MRI. The first is based on the heme domain of the bacterial cytochrome P450-BM3, which produces changes in T1 contrast in MRI in response to small molecule binding. We developed a high-throughput assay that allowed us to evolve this protein into a sensor of the neurotransmitter dopamine (DA). We then used it to image DA release from cultured cells and cocaine-induced changes in DA transport in the brains of living rats. The second platform is based on the human iron storage protein ferritin (Ft), which enhances T2 contrast in MRI upon self-aggregation. We developed a system to express self-assembled Ft nanoparticles incorporating multiple surface functionalities, and used it to create a sensor for protein kinase A activity. Our results provide a proof of concept for two novel platforms for protein-based MRI sensor development, and highlight some key advantages of this approach over the synthetic methods used previously.

Thesis co-advisors: Alan Jasanoff, Robert Langer

Acknowledgements

First, I would like to thank my co-advisors, Robert Langer and Alan Jasanoff, for the enthusiasm and insight with which they supported the projects described in this thesis, and for the extraordinary faith they placed in me to manage and execute this work. I am also grateful to them for creating wonderful environments in which to pursue ideas, establish collaborations and learn from other people.

I would like to thank my committee chair, Angela Belcher, for the interest she took in this thesis and the critical input she provided throughout its completion.

I am extremely grateful to Frances Arnold and her laboratory at Caltech for being incredible collaborators in the project described in chapter 3 of this thesis. Philip Romero, in particular, was an indispensable partner. Christopher Otey provided critical help at the start of this project.

I am also very grateful to Gil Westmeyer in the Jasanoff lab for taking on the challenging *in vivo* experiments that contributed greatly to the significance of our work.

Special gratitude belongs to Jerzy Szablowski, who as an undergraduate assistant exceeded all expectations and made major contributions to experimental work across this thesis.

I would also like to thank my co-authors on the theoretical publication that became chapter 1 of this thesis (Tatjana Atanasijevic, Henryk Faas, Gil Westmeyer and Alan Jasanoff) and informed my subsequent experimental work.

I am honored and grateful to have received financial support from the Fannie and John Hertz Foundation. The freedom given to me by their generosity enabled me to think big and take risks. I am also thankful to have been part of the community of Paul and Daisy Soros fellows.

Loving gratitude goes to Michelle Lam, whose intelligence, beauty and wit gave me inspiration and happiness as I faced challenges in the lab.

Finally, I would like to thank my parents, George and Larisa Shapiro for their courage and sacrifice in moving our family to the US and working tirelessly to make sure their children had access to the best education and opportunities. My accomplishments belong to them.

Table of Contents

List of Figures

1. Background and Introduction

2. Dynamic Imaging with MRI contrast agents: quantitative considerations

3. Protein-based MRI contrast agents engineered to sense neurotransmitter dynamics in vivo

4. Protein nanoparticles engineered to sense protein kinase activity in MRI

Appendix A

Appendix B

Appendix C

1. Background and Introduction

1.1 Molecular imaging: motivation and modalities

There is currently a growing appreciation that many biological phenomena, even those that result in gross phenotypes or behaviors, are mediated by interactions at the molecular level. There is therefore intense interest in the development of tools for observing the concentrations and activities of particular biological molecules in living specimens[1].

Neuroscience is a field that has placed a special emphasis on molecular sensing. Information processing in the nervous system is largely carried out by molecular signaling events that occur in precise spatial and temporal patterns. Historically, molecular-level information has only been available from in vitro biochemical assays, while spatial data came from fixed cells and tissues stained with various dyes. While this provided crucial insights, much information was lost due to spatio-temporal decoupling of events and measurements. More recently, molecular sensors have been developed that enable real-time imaging of molecular events in living specimens through fluorescence, radioactivity, or nuclear magnetic resonance.

Fluorescent reporters have been engineered to couple their fluorescent signal to the binding of specific compounds. Fluorescent sensors have been developed for DNA and RNA interactions, metal ions, pH, kinase activity, and various organic metabolites[2-4]. While these sensors often provide exquisite sensitivity and spatiotemporal resolution, their application in biological and medical imaging is severely limited by the scattering of light by tissues. This limitation has meant that most fluorescent sensors are only useful at the level of cells and small tissue specimens or optically accessible parts of living subjects (e.g. skin). This limitation is a particular problem in neuroscience since the brain is encased in an opaque skull.

Radioactive probes work in living, opaque tissues, and allow the imaging of molecular activity by tracking the concentration and distribution of radioactively labeled molecules via the products their radioactive decay. For example, positron emission tomography (PET) is often used in the clinic with ^{18}F-fluorodeoxyglucose (FDG) to image areas of elevated metabolic activity indicative of tumors[5]. In these areas, a higher than normal demand for glucose causes FDG to be locally concentrated, producing an increase in radioactive emission. Other radioactive probes are based on receptor ligands, and are used to monitor the expression and occupancy of their corresponding target receptors[6]. While these methods are sensitive, they have relatively low spatial resolution (lower than 1 mm), and because their interpretation is often based on kinetic modeling, they are best suited to studies of chronic conditions or temporal changes that occur on the time scale of many minutes or longer. A key limitation for future development of radioactive probes is their "always-on" operation. Radioactive decay occurs regardless of probes' molecular environment (whereas fluorescent sensors turn on and off in response to interactions with other molecules); thus radioactive probes cannot "sense" what is happening at their location but merely report where they are.

Magnetic resonance imaging (MRI), which captures interactions between nuclear spins and an applied magnetic field, has been a particularly useful tool for the imaging of live subjects, capturing contrast produced by both endogenous tissue elements and exogenous imaging agents. MRI is capable of providing high spatial (< 100 μm) and temporal (~1s) resolution, and works with opaque specimens[7]. Importantly, a variety of mechanisms are available by which imaging agents can produce MRI contrast, making it possible to couple the signal produced by such agents to interactions with specific molecules of interest. MRI thus combines some of the best elements of fluorescent and radioactive imaging. The fundamentals of MRI and MRI contrast agents are discussed in the next section.

1.2 Magnetic resonance imaging (MRI) and MRI contrast agents

MRI is an imaging modality that interacts with the magnetic moments of nuclear spins, typically the ^1H spins of water molecules. In the presence of a strong applied magnetic field, nuclear spins are aligned "longitudinally" – parallel to the applied field. (Fig. 1). In a typical MRI experiment, a radio frequency electromagnetic pulse rotates these spins 90° into the "transverse plane" where they produce a resonant signal which serves as the readout of MRI. The contrast observed in MRI images comes primarily from two spin relaxation mechanisms. First, transversely aligned spins that are initially in phase with each other get dephased by local inhomogeneieties in the magnetic field in a process called transverse or T2 relaxation, which causes spin orientations to cancel out and leads to a loss of signal. In a second relaxation process known as longitudinal or T1 relaxation, transverse spins re-align themselves parallel to the applied magnetic field as they dissipate their excitation energy through interactions with their local chemical environment. MRI imaging typically captures the contrast produced by spatial variation in either ^{1}H density or T2 or T1 relaxation across a tissue specimen.

Endogenous MRI contrast produced by variation in chemical properties across different tissues has found extensive utility in basic science and medicine. Abnormalities in MRI images indicative of tissue damage and tumor formation are frequently used in clinical diagnosis[8, 9]. Changes in the size or contrast of particular brain regions are used to monitor the progression of neurological disease[10]. And functional MRI (fMRI), which takes advantage of oxygenation-dependent T2 contrast changes in hemoglobin (as described in more detail below), has been used extensively to monitor gross activation of different parts of the brain during mental tasks

MRI contrast can be enhanced through the use of MRI contrast agents – magnetically active substances that typically produce image contrast by changing the T1 or T2 relaxation rates of aqueous protons (Fig. 2). For example, Gd-DTPA is an organic chelate of gadolinium(III) that is commonly used in diagnostic MRI[11]. Gd3+ is strongly paramagnetic, and its seven unpaired electrons interact with aqueous protons in a way that enhances T1 relaxation and produces an increase in signal intensity observed in T1-weighted MRI images. Another example is superparamagnetic iron oxide (SPIO), which comes in the form of iron oxide nanoparticles with diameters of approximately 10nm, coated with a biocompatible organic shell[12]. In tissues being imaged with MRI, SPIOs produce local magnetic field inhomogeneieties which enhance T2 relaxation, causing a decrease in signal intensity on a T2-weighted MRI image. Contrast agents have also been developed that work through more complex mechanisms, including chemical exchange dependent saturation transfer (CEST)[13].

Several efforts have been made to create synthetic molecular sensors based on gadolinium and SPIOs . One example is a Ca^{2+}-sensitive T1 agent made by Li et al[14]. In general, the relaxivity of T1 contrast agents depends on the ability of water molecules to coordinate to the contrast agent's paramagnetic ion. Thus if the availability of Gd^{3+} coordination sites can be made to change in response to molecular interactions, it would create a functional sensor. Li et al synthesized a molecule called DOPTA-Gd (Fig. 3a) which features two Gd^{3+} chelates and a calcium-binding BAPTA group. In the presence of calcium, the four carboxylate arms of BAPTA are occupied by calcium binding, and the two Gd^{3+} ions have open coordination sites for interactions with water. When calcium is removed, the BAPTA carboxylate groups displace the water molecules coordinated to Gd^{3+}, shutting off the mechanism of MRI contrast and causing an 80% drop in relaxivity.

Functional sensors have also been made using SPIOs. In this case, a change in T2 contrast can be produced by triggered SPIO aggregation, which enhances the dephasing effect of SPIO magnetic fields on aqueous protons. Molecular sensors based on this mechanism have been made by functionalizing the surface of SPIOs with biomolecules that bind to each other and cause aggregation in the presence of specific molecular triggers. For example, Perez et al used this strategy to create sensors for specific DNA sequences[15], while Atanasijevic et al created sensors for Ca^{2+} based on calcium-dependent binding of calmodulin to M13[16] (Fig. 3b,c).

Functional sensors based on CEST have also been proposed for the measurement of bulk environmental variables such as pH[17, 18].

Key quantitative considerations relating to the mechanisms, design and application of molecular sensors for MRI are covered in detail in Chapter 2.

1.3 Limitations of synthetic molecular sensors for MRI

Despite their theoretical appeal, several factors have delayed the development and application of dynamic molecular sensors for MRI, including complexity of design, difficulty of synthesis, and limited avenues for delivery to target biological tissues. As described above, most existing MRI sensors comprise large, complicated organic structures or supramolecular assemblies. Engineering such sensors usually requires starting from scratch and iterating through painful re-synthesis of complete structures. For example, to alter the specificity of DOPTA-Gd from calcium to another ion would likely require replacing the BAPTA substructure with another chelate, and painstakingly modifying the resulting structure one bond at a time to ensure proper spacing for water-competitive interactions with Gd^{3+}.

Secondly, both organic and SPIO-based sensors can be difficult to synthesize consistently. Chelate-based sensors have intricate organic structures that require complicated multi-step syntheses. For example, DOPTA-Gd is synthesized through 8 steps with a 0.4% total yield. SPIO-based sensors comprise supramolecular assemblies of particles displaying multiple surface functionalities. Their performance is highly dependent on the precise quantities of functional moieties on particle surfaces, which impacts their avidity for each other or target molecules and their non-specific colloidal behavior. Getting consistent functional group coverage using chemical crosslinking is an acknowledged challenge. While many synthesis difficulties could eventually be overcome with the standardization and controls introduced in industrial scale-up, they continue to impede iterative sensor development and discourage researchers from making sensors for a wider variety of imaging targets.

Finally, a major limitation for future use of synthetic MRI sensors *in vivo* is the difficulty of delivering them to target cells and tissues. Sensors based on organic metal chelates are large molecules with significant ionic charge, and SPIO-based sensors comprise assemblies of relatively large (>30nm) particles. Getting such molecules and assemblies to specific tissues commonly requires disruption of local tissue architecture, and sustained or repeated imaging would necessitate repeated administration or the engineering of special devices to prevent sensor clearance.

1.4 Basis and potential advantages of genetically engineered molecular sensors for MRI

What if molecular sensors for MRI could be made through genetic engineering of proteins? Protein-based sensors could be developed using well-established protein engineering methods. They could be synthesized easily in cultured cells. And they could be applied *in vivo* by direct delivery or in-situ synthesis in cells targeted with corresponding genetic constructs. They could thus potentially overcome some of the aforementioned challenges facing synthetic sensors.

To create MRI sensors based on proteins, one could take advantage of the magnetic properties of naturally occurring metalloproteins, which contain paramagnetic ions that can interact with water molecules to accelerate nuclear magnetic T_1 or T_2

relaxation rates and thus produce MRI contrast. Many classes of proteins contain metal elements which serve as enhancers of binding, catalysis or electron transfer.

In fact, an important precedent for protein-based MRI sensors already exists in the form of hemoglobin (Hb), the protein responsible for oxygen transport in blood. Each of Hb's four subunits houses a heme-coordinated iron(II) atom that has one coordination site available for the binding of O_2 (Fig. 4), the occupancy of which depends on local O_2 concentration[19]. In its deoxy state, Hb's Fe^{2+} ions have unpaired electrons, making the protein paramagnetic and causing it to produce T2 contrast in MRI. When oxygen is bound, Fe^{2+} electrons transition to a paired state, eliminating the protein's paramagnetism and T2 contrast. As a result, Hb functions as an MRI sensor of oxygen. This property of Hb forms the basis of fMRI, where it enables the observation of locally elevated metabolic activity in the brain during mental tasks[20].

If other proteins like Hb can be identified or created to sense various molecular targets, the resulting protein-based sensors could have three important advantages over synthetic sensors. First, their design and modification could be aided by the use of established protein engineering approaches, including rational mutagenesis, recombination and directed evolution. These approaches have been used successfully to create proteins for a variety of purposes, including protein-based fluorescent sensing, enzymatic catalysts, receptor binding and organization of inorganic materials. One advantage of these methods is the ease and low cost with which proteins' specificity can be altered. In the context of MRI sensors, this could mean that an imaging agent that senses one molecule could be modified to sense another without having to design an entirely new sensor from scratch.

A second potential advantage of protein-based MRI sensors could be ease of synthesis. Many expression systems ranging from bacteria to whole animals exist that can make proteins after transfection with the corresponding DNA. For each sensor, an appropriate system can be chosen based on codon compatibility, post-translational modifications and requirements for co-expression with other proteins. Once an expression system is established for a given sensor, derivatives of this sensor can likely use the same system.

Finally, a potential long-term advantage of genetically engineered molecular sensors is the number of delivery options they make available for in-vivo use. Both synthetic sensors and purified protein-based sensors could be delivered to target tissues in their intact form. But unlike synthetic sensors, protein-based sensors could also potentially be delivered to target cells as genes. This would allow them to take advantage of existing and future gene delivery methods, including viral and non-viral vectors. Genes could be delivered in-situ to their target tissues, or could be pre-inserted into cells (such as stem cells) destined for implantation.

1.5 Two protein platforms for the development of genetically engineered molecular sensors for MRI

This thesis explores two protein platforms for developing genetically engineered molecular sensors for MRI. Both platforms are based on naturally occurring metalloproteins that produce MRI contrast. They differ in the their contrast mechanisms (T1 vs T2), the protein engineering methods employed in modifying them to sense specific molecular targets, and the targets chosen in each case.

The first platform is based on the cytochrome P450-BM3, a water-soluble fatty acid monooxygenase from *Bacillus megaterium* (BM3). The wild-type BM3 enzyme is a soluble fatty acid hydroxylase comprising a 53 kDa heme domain fused to a 65 kDa reductase domain[21]. The heme domain (BM3h) contains a single paramagnetic iron(III) atom (mixed spin 1/2 and 5/2[22]), bound to a hemin prosthetic and axially coordinated by residue C399 on the protein. In the absence of substrate, the remaining iron coordination site is filled by a water molecule[23]. Interaction between exchanging water molecules at the axial site and the heme iron atom promotes T1 relaxation in aqueous solutions[24]. In a manner similar to DOPTA-Gd, the binding of BM3's native substrates (long-chain fatty acids) at the paramagnetic Fe3+ displaces water molecules and reduces the T1 effect, making BM3h a candidate molecular sensor. To create a sensor for interesting small molecules (for example, neurotransmitters), the binding specificity BM3h would have to be tuned away from it native substrates to the specific molecules of interest.

Conveniently, the ability to tune substrate binding in BM3h has already been demonstrated by Frances Arnold and colleagues, who used directed evolution to create BM3h-based catalysts for hydroxylation of substrates ranging from simple alkanes to pharmaceuticals[25, 26]. In this method, random mutations are introduced into BM3 and the resulting mutants are screened in high throughput for activity on a desired novel substrate. Although this activity-based screening methodology can not be used directly to evolve new specificity for MRI sensing, it suggests that a similar approach might be possible to create sensors for molecules like dopamine.

A second potential platform for genetically engineered MRI sensors is the iron storage protein ferritin (Ft). Ft comprises a 12nm protein shell and an 8nm antiferromagnetic iron oxide core containing up to 4,000 iron atoms[27]. Ft induces T2 relaxation in MRI and has been studied as an endogenous source of anatomical contrast and an exogenous marker of gene expression[28-30]. Aggregation of Ft after proteolysis[31] or chemical cross-linking[32] has been shown to enhance its T2 contrast, suggesting that Ft-based sensors could be made analogously to those previously created using synthetic iron oxide nanoparticles[15, 33, 34].

Ft nanoparticles comprise 24 heavy chain (HF) and light chain (LF) subunits which self-assemble into symmetrical nanoparticles at ratios proportional to their relative expression levels[35]. The N-termini of LF and HF are exposed at the nanoparticle surface, and can thus serve as sites for genetic fusion of surface functional groups[36]. Analogously to synthetic SPIO-based sensors, surface functional groups could be fused to Ft subunits that caused Ft nanoparticles to aggregate in response to the presence or activity of specific target molecules. A combination of fusion constructs and wild-type subunits could hypothetically be co-expressed at particular ratios to achieve desired surface properties and sensor performance, and the entire sensor would then be genetically encoded, preserving the advantages of design, synthesis and delivery of protein-based sensors.

1.6 Targets for molecular sensor development: dopamine and protein kinase A

In working towards a proof of concept for molecular sensors for MRI based on BM3h and Ft, we selected targets that were compatible with the basic operation of each sensor. This meant selecting a small molecule for BM3h and a molecule whose activity triggered the binding of two protein moieties in the case of Ft. We also chose targets that were of high value to neuroscience and for which no non-invasive sensors have previously been developed. These targets we dopamine for BM3h and protein kinase A for Ft.

Dopamine (DA) is a neurotransmitter of particular interest because of its role in learning, reward and motor coordination[37]. Dysfunction of dopaminergic systems is implicated in addiction[38] and neurodegenerative diseases[39]. Most measurements of DA release in basic research rely on invasive techniques like microdialysis[40] and voltammetry[41], which report variations of DA concentration at a single site in the brain. Positron emission tomography (PET) is used to monitor DA receptor occupancy and related variables[42]. PET methods are sensitive, but have relatively low spatial resolution (> 1 mm); and because most PET measurements are based on kinetic modeling, they are best suited to studies of chronic conditions or temporal changes that occur on the time scale of many minutes or longer. To build an understanding of how DA functions in brain processing, there is therefore a need to develop measurement techniques that could be applied at a whole-brain level, and that have significantly better spatial and temporal resolution than PET. MRI, in combination with a suitable contrast agent sensor, would help satisfy this need.

No MRI contrast agent for sensing DA (or any other neurotransmitter) has been reported to date, and the specifications for such an agent are strict. DA fluctuations in the basal ganglia of the brain, for instance, take place on the order of seconds, and involve peak DA concentrations $< 100\ \mu M$[43, 44]. A DA sensor must therefore respond quickly, reversibly, and specifically to DA fluctuations in the micromolar range. To be comparable with established functional brain imaging techniques (fMRI), the probe must also be capable of producing image signal changes in tissue on the order of 1% or more[45].

Cyclic AMP-dependent protein kinase A (PKA) plays a critical role in memory formation and is an active target of pharmaceutical development[46]. PKA forms a key connection in signaling pathways leading from activation of g-protein coupled receptors at the cell surface to transcriptional changes in the nucleus. It is activated by cyclic AMP and phosphorylates a variety of cytoplasmic and intranuclear substrates. A key substrate of PKA is the transcription factor CREB[47]. When the residue Ser133 of the kinase inducible domain (KID) of CREB is phosphorylated by PKA, CREB binds to the KIX domain of the activator protein CBP[48, 49], turning on transcription of CREB-dependent genes[50]. Phosphorylation-dependent binding of KID and KIX has been studied extensively, and fluorescent sensors of PKA activity have been made by fusing these domains to variants of green fluorescent protein[51] or β-lactamase[52]. This suggests that KID and KIX could serve as Ft-fused surface moieties in a Ft-based MRI sensor design. No MRI or other non-invasive sensor of PKA activity has been reported.

1.7 Organization of thesis

This thesis is organized in five chapters, beginning with this introduction. Chapter 2 of this thesis, titled "Dynamic imaging with MRI contrast agents: quantitative considerations" discusses quantitative theoretical considerations underlying the design of biological sensors for MRI. These considerations are applicable to both synthetic and protein-based sensors, and helped guide the experimental work described in subsequent chapters. Chapter 3, titled “Protein-based MRI contrast agents engineered to sense neurotransmitter dynamics in vivo”, describes our work on the BM3h platform for protein-based sensor development and its use to create an MRI sensor of dopamine. Chapter 4, titled “Protein nanoparticles engineered to sense protein kinase activity using MRI”, describes our work on ferritin as a platform used to develop a sensor of PKA activity. Chapter 5 provides conclusions and future directions, and is followed by three appendixes describing additional results on mammalian expression of BM3h (Appendix A), studies of the MRI effects of chemically-induced aggregation of Ft (Appendix B) and full gene and vector sequences for proteins used in this thesis (Appendix C).

FIGURE LEGENDS

Figure 1. Physical principles behind MRI. **(a)** Left: a single nuclear spin, represented by it positive charge and magnetic moment (red). Middle: spins are randomly aligned in the absence of a magnetic field and have zero net magnetization, M. Right: in the presence of an applied magnetic field, B, spins align with the field and have a net moment M parallel to B. **(b)** Left: In an applied field, spins precess about the field axis at a characteristic Larmor frequency, ω. Right: in MRI, an electromagnetic pulse at frequency ω is applied to move spin magnetization perpendicular to the applied field. **(c)** Left and middle: representation of bulk spins behaving as described in (b), with 90° spins in middle in phase with each other and emitting a radiofrequency signal. Right top: in T2 relaxation, spins stay perpendicular to the field, but lose phase coherence, resulting in a loss of net magnetization. Right bottom: in T1 relaxation, spins regain alignment parallel to the field.

Figure 2. Prototypical T1 and T2 contrast agents. **(a)** T2 contrast agents are typically iron oxide nanoparticles of 10-100nm size, with an organic coating, that produce a magnetic field in their vicinity which dephases aqueous proton spins. **(b)** T1 contrast agents typically contain paramagnetic metal ions that interact with aqueous protons in a way that enhances relaxation to longitudinal alignment.

Figure 3. Examples of previously developed MRI sensors. **(a)** Calcium sensor DOPTA-Gd from Li at al., in which sensing is accomplished through Ca^{2+}-dependent changes in

Gd^{3+} accessibility to water molecules. **(b)** DNA sensor from Perez et al., in which sensing is accomplished by DNA-mediated aggregation of complementary DNA-functionalized SPIOs. **(c)** Calcium sensor from Atanasijevic et al, in which inter-particle binding is allosterically regulated by Ca^{2+}.

Figure 4. Magnetic properties of hemoglobin. **(a)** Illustrated structure of Hb, with four heme groups containing iron. **(b)** Illustration of the Hb heme group without (left) and with (right) oxygen bound. Deoxy heme is paramagnetic and produces T2 contrast. Oxyheme is diamagnetic.

Figure 1

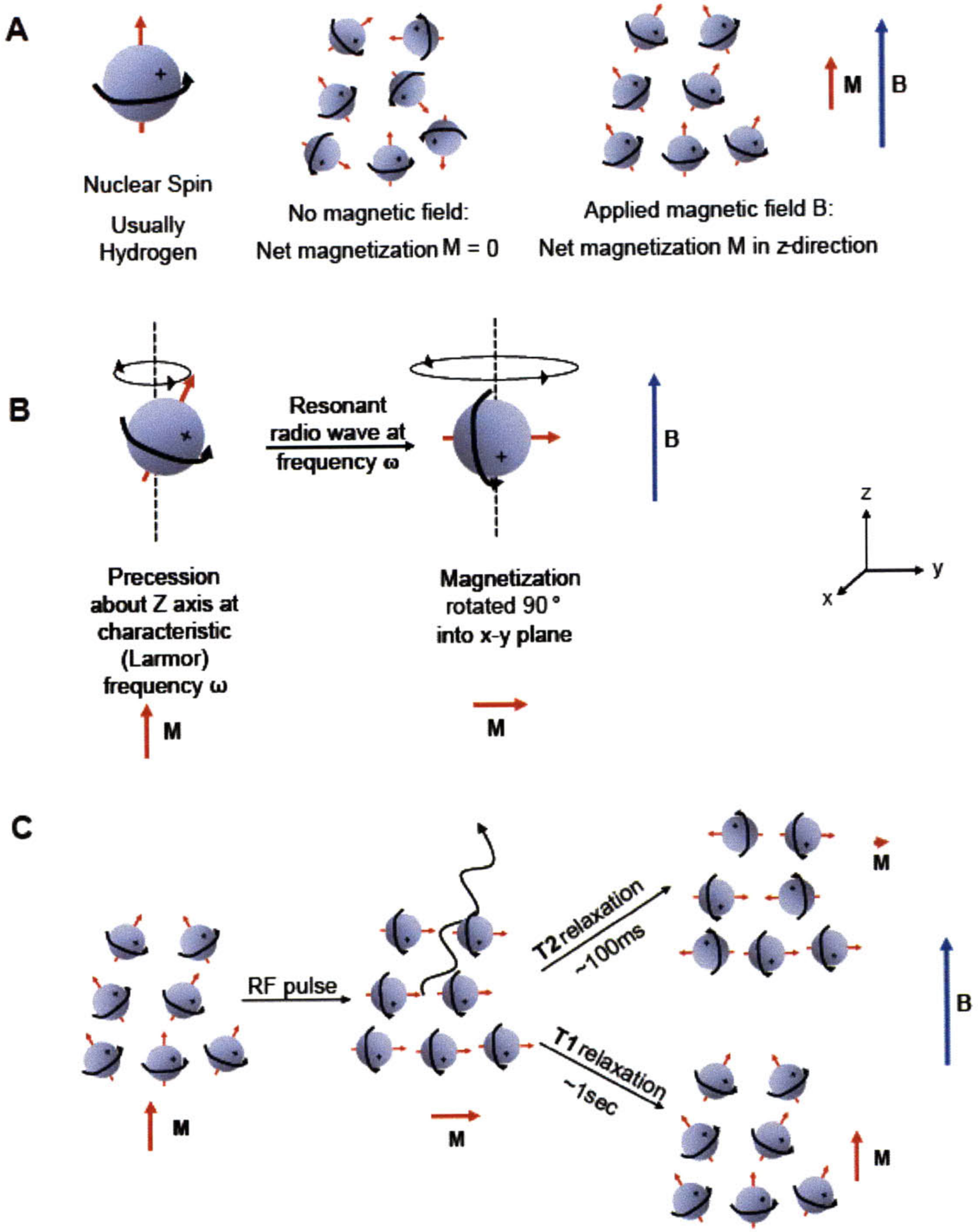
A
Nuclear Spin
Usually Hydrogen
No magnetic field:
Net magnetization M = 0
Applied magnetic field B:
Net magnetization M in z-direction
M
B
B
Resonant radio wave at frequency ω
Precession about Z axis at characteristic (Larmor) frequency ω
Magnetization rotated 90 ° into x-y plane
M
M
B
z
y
x
C
RF pulse
T2 relaxation ~100ms
T1 relaxation ~1sec
M
M
M
M
B

Figure 2

A T2 contrast agents: create inhomogeneous field

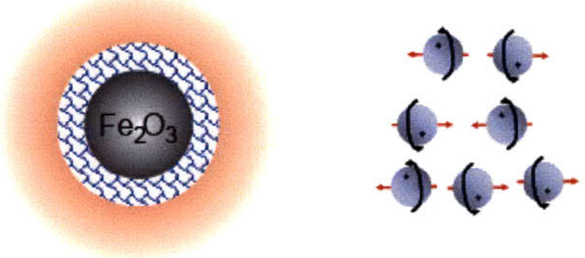

B T1 contrast agents: help protons relax to low energy state

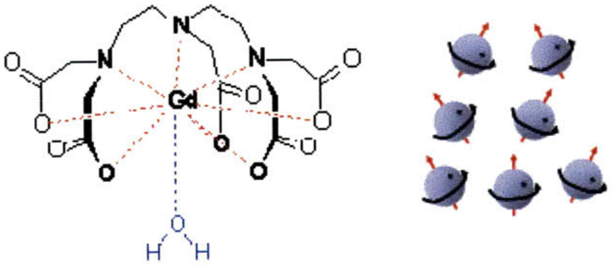

Figure 3

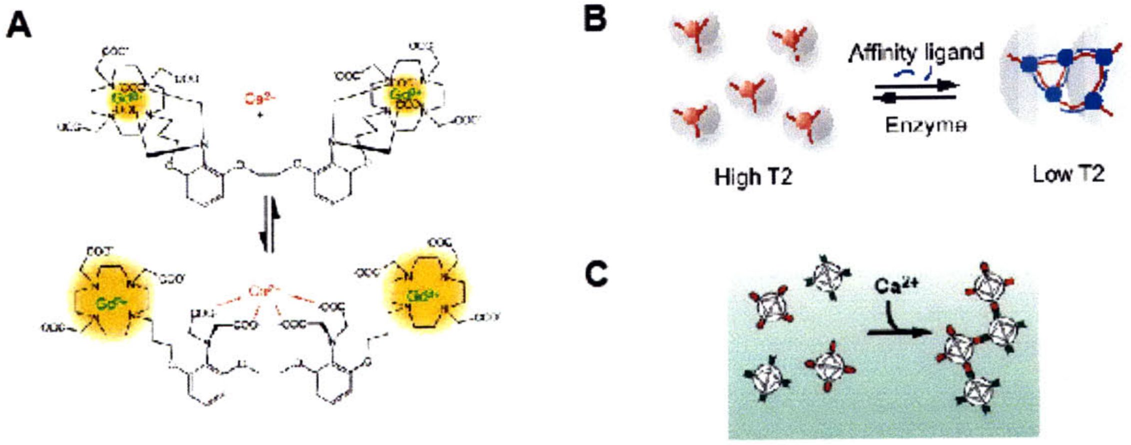

Figure 4

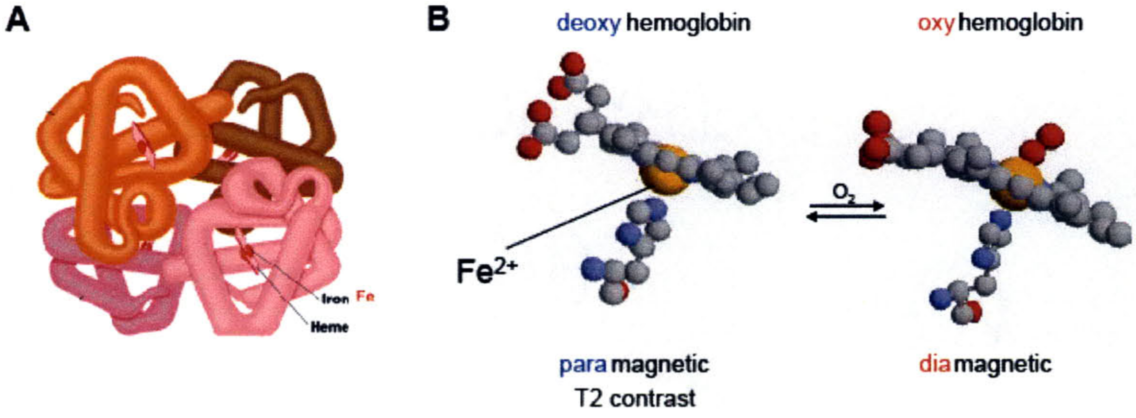
A
Iron Fe
Heme
B
deoxy hemoglobin
oxy hemoglobin
Fe2+
O2
para magnetic
T2 contrast
dia magnetic

2. Dynamic imaging with MRI contrast agents: quantitative considerations

ABSTRACT

Time-resolved MRI has had enormous impact in cognitive science, and may become a significant tool in basic biological research with the application of new molecular imaging agents. In this paper we examine the temporal characteristics of MRI contrast agents that could be used in dynamic studies. We consider "smart" *T1* contrast agents, *T2* agents based on reversible aggregation of superparamagnetic nanoparticles, and sensors that produce changes in saturation transfer effects (CEST). We discuss response properties of several agents with reference to available experimental data, and we develop a new theoretical model that predicts the response rates and relaxivity changes of aggregation-based sensors. We also perform calculations to define the extent to which constraints on temporal resolution are imposed by the imaging methods themselves. Our analysis confirms that some small *T1* agents may be compatible with MRI temporal resolution on the order of 100 ms. Nanoparticle aggregation *T2* sensors are applicable at much lower concentrations, but are likely to respond on a single second or slower time scale. CEST agents work at high concentrations and temporal resolutions of 1-10 s, limited by a requirement for long presaturation periods in the MRI pulse sequence.

keywords: *contrast agent, molecular imaging, sensor, temporal resolution, superparamagnetic nanoparticle*

INTRODUCTION

Many of life's most important processes occur within a fraction of a second. With temporal and spatial resolution orders of magnitude cruder than optical imaging, MRI seems a deeply insufficient tool for investigation of this "short-timescale physiology." But with opaque specimens, noninvasive imaging with MRI may still be a uniquely valuable approach. Echo planar pulse sequences allow images to be collected in tens of milliseconds—fast enough to freeze-frame the beating heart or record rapid fluctuations of blood flow in the brain [53]. In many other contexts, the limitation on MRI has not been its intrinsic acquisition rate, but rather the absence of contrast mechanisms that can translate biological events of interest into MRI-detectable signal changes.

Newly developed contrast agents, products of the growing field of molecular imaging, are beginning to change this situation [54, 55]. Several groups have introduced agents useful for mapping static or slowly varying patterns of gene expression and epitope distribution [15, 56-58]. Contrast agents have also been developed for sensing more dynamic variables such as pH [59-61], oxygen tension (pO_2) [62, 63], ion and metabolite concentrations [14, 64, 65], and enzyme-catalyzed reactions [15, 57]. These agents have been referred to as "smart" contrast agents, and function as sensors in MRI, analogous to fluorescent probes used in optical imaging and microscopy. Some MRI sensors could in principle be applied to study fast (generally cellular) physiological events, for example: endocytic pH changes during vesicle recycling on the one second time scale, calcium signaling transients lasting 10-100 ms, pO_2 fluctuations within 2 s of modulations to oxidative metabolism, and changes in protein phosphorylation in seconds to minutes during neuronal synaptic plasticity. In each case, however, the practical time resolution attainable with contrast agent-enhanced MRI may be limited by the agent's molecular properties and by the physical requirements of contrast generation.

Characteristics of contrast agents and methods for their detection vary widely. Historically, the most commonly used are small paramagnetic metal chelates which act by shortening *T1* (longitudinal) relaxation times [66]. MRI sensors (Figure 1) have been constructed from these agents by coupling determinants of their *T1* relaxivity—solvent accessibility, rotational correlation time, or the spin and redox state of the metal [?ref?]—to the presence of specific molecular targets. Sensors based on *T2* (transverse) relaxation rate changes have also been produced, most recently by coupling the aggregation state of superparamagnetic iron oxide nanoparticles (SPIOs) to physiological signals of interest. Aggregation of SPIOs even in concentrations as low as 10 mg/L can change observed *T2*'s quite dramatically [15]. A third family of MRI sensors has been based on chemical exchange saturation transfer effects (CEST) [13]. Labile protons or water molecules bound to a CEST agent can be selectively saturated, and will exchange with bulk solvent protons to decrease the local MRI signal. In CEST-based sensors, the exchange rate or chemical shift of bound protons is modulated by interaction with the sensor's target [67, 68].

To be useful for dynamic imaging studies, an MRI sensor must produce a fast and large enough signal change to be detected on the desired timescale. Although the steady-state detection thresholds for various contrast agents have been discussed extensively in the literature (*e.g.* [69-72]), the interaction between sensitivity and dynamics has been less thoroughly examined. At the same time, a systematic analysis of advantages and disadvantages of available contrast mechanisms is essential to the development of effective strategies for fast-timescale molecular imaging. In this paper, we review the molecular mechanisms of some paradigmatic smart *T1*-, *T2*-, and CEST-based contrast agents, and consider the agents' response rates using a combination of simulations and reference to existing experimental data. Throughout the paper, we estimate the temporal resolution of each molecular imaging strategy as the inverse of the duration of the impulse response that relates an underlying stimulus or change in conditions, via the contrast agent and MRI pulse sequence, to a detectable signal change. Because of the importance of the MRI acquisition method in determining this temporal resolution, we include a discussion of detection methods themselves along with consideration of the different classes of molecular imaging agents.

MATERIALS & METHODS

Bloch equation simulations

Magnetization trajectories were estimated by using Euler integration of the Bloch equations to simulate one or two spin-pool evolution in the presence of relaxation and chemical exchange. Radiofrequency (RF) excitation pulses were modeled as instantaneous rotations, and Larmor precession was omitted from the calculations. Presaturation used in CEST simulations was modeled as a π pulse train delivered at fixed frequency (generally 2 kHz) during a presaturation period *TP*. Parameter settings are noted where appropriate in the text. Time steps used in the calculations were chosen to be a factor of ten below the smallest characteristic time relevant to the simulation.

Macroscopic susceptibility effects (*i.e.* *T2** relaxation components) were omitted. All simulations were performed using custom routines running under Matlab (Mathworks, Natick, MA) on a Linux-based workstation.

SPIO aggregation simulations

SPIO aggregation and disaggregation were simulated using the Euler method, applied to the Smoluchowski equation [see Eq. (16) below], which describes the transition rates among single particles and aggregates of all allowable sizes. The aggregation kernel K_{agg}, adapted from Odriozola *et al.* [73], describes the rate constant for binding of two aggregates of compositions (i, j) and (k, m) as a function of their diffusion-limited collision rate and their probability of sticking upon collision:

$$K_{agg}(i,j,k,m) = k_{dl}(i,j,k,m)\frac{P_{stick}(i,j,k,m)\varepsilon\left[(i+j)(k+m)\right]^{b}}{1+P_{stick}(i,j,k,m)\left\{\varepsilon\left[(i+j)(k+m)\right]^{b}-1\right\}} \quad (1)$$

where $\varepsilon$and b correspond to Odriozola's constants N_{11} and b, respectively, with respective values of 6.1 and 0.35. $k_{\mathrm{dl}}(i, j, k, m)$ is the diffusion-limited collision rate due to Brownian motion, given by:

$$k_{dl}(i,j,k,m) = \frac{2k_B T}{3\eta}\left([i+j]^{1/df}+[k+m]^{1/df}\right)\left([i+j]^{-1/df}+[k+m]^{-1/df}\right) \quad (2)$$

where k_{B} is the Boltzmann constant, T is the absolute temperature, η is the medium viscosity and df is the fractal dimension of the aggregates (assumed to be constant throughout aggregation). $P_{\mathrm{stick}}(i, j, k, m)$ is the sticking probability of the two aggregates, given by:

$$P_{stick}(i,j,k,m) = P_{11}\left[N_i\left(\frac{i}{i+j}\right)N_m\left(\frac{m}{m+k}\right) + N_k\left(\frac{k}{k+m}\right)N_j\left(\frac{j}{i+j}\right)\right] \quad (3)$$

where N_x for $x=i,j,k,m$ represents the fraction of functional groups of the corresponding type available for binding, *e.g.*:

$$N_i = \frac{(f-1)i - j + 1}{fi} \quad (4)$$

where f is the number of functional groups per particle and (i, j) is the aggregate composition. P_{11} is the sticking probability for a collision of two oppositely-functionalized monomers, which we estimated by assuming cubical geometry for the two types of functional groups, with sides of length d_a and d_b and calculating the fraction of the particle surface that is covered by the functional group (for given functionalization ratios f and g and particle radius r). The product of these surface fractions is then multiplied by the bimolecular sticking probability P_{bm} for free functional groups in solution, which may be roughly estimated as the ratio of their known binding on-rate k_{on} and their theoretical diffusion-limited collision rate. We include an additional factor of 6 to account for an assumption that the cubic functional groups are optimally oriented on the particle surface. The resulting expression is:

$$P_{11} = P_{bm}\left(\frac{6fd_a^{\ 2}}{4\pi r^2}\right)\left(\frac{6gd_b^{\ 2}}{4\pi r^2}\right) \tag{5}$$

The fragmentation kernel K_{frag}, adapted from Laurenzi and Diamond [74], describes the rate constant of fragmentation of an aggregate of composition $(i + k, j + m)$ into two aggregates (i, j) and (k, m):

$$K_{frag}(i,j,k,m) = k_{off}\left[A_f(i,j)A_g(k,m) + A_f(k,m)A_g(i,j)\right]\frac{N_{iso}(i,j)N_{iso}(k,m)}{N_{iso}(i+k,j+m)} \tag{6}$$

Here, k_{off} is the bimolecular dissociation rate for the complimentary functional groups. A_f and A_g are the number of free functional groups of the two types in aggregates of a given composition, i.e.:

$$A_f(i,j) = (f-1)i - j + 1; \qquad A_g(i,j) = (g-1)j - i + 1 \tag{7}$$

N_{iso} is a combinatorial factor describing the number of possible arrangements of particles in an aggregate of a given composition:

$$N_{iso}(i,j) = \frac{f^i g^j (fi-i)!(gj-j)!}{\left[A_f(i,j)\right]!\left[A_g(i,j)\right]!i!j!} \tag{8}$$

In order to minimize the computational cost of our simulation, we imposed an upper limit on the allowed aggregate size, $C(z, z)$, with $z = 45$. This limit allowed the kernels to be pre-defined, greatly speeding up the simulations. Under simulation conditions that favor extensive aggregation, this limit causes an underestimation of average particle size and an accumulation, or "bunching", of the aggregate population at sizes near the maximum. However, the parameters used in most of our runs produced aggregates with average sizes well below this upper limit, and resulting size distributions that did not exhibit significant bunching. When noticeable bunching did occur, it produced only a minimal effect on simulation time courses (below 5% for T_{obs}), with "saturating" effects on steady-state size evident only when this size approached $2z$.

Unless otherwise noted in the main text, the parameters used in our aggregation simulations were as follows: $k_{\mathrm{on}} = 10^6\ \mathrm{M}^{-1}\ \mathrm{s}^{-1}$, $k_{\mathrm{off}} = 6 \times 10^{-4}\ \mathrm{s}^{-1}$, $f = 50$, $g = 50$, $r = 15$ nm, $df = 2.2$, T = 300 K, $\eta = 1$ cp, $R2$ (non-aggregated relaxivity) = 20 (mM Fe)$^{-1}$ s^{-1}, Fe atoms per particle = 2064. The same equations and parameters were used to simulate disaggregation, but with a factor of 10^2 decrease in k_{on} and a factor of 10^2 increase in k_{off}.

Additional calculations and data presentation. Additional computations, including calculations of percent signal change for *T1* and CEST imaging, were performed using Matlab. Kaleidagraph (Synergy Software, Reading, PA) and Adobe Illustrator (Adobe Systems, San Jose, CA) were used in the preparation of figures.

RESULTS & DISCUSSION

Dynamic imaging with smart T1 contrast agents

Temporal resolution of* T1*-weighted imaging. Several of the first MRI sensors were *T1* agents synthesized by Meade and colleagues, that respond to their targets with roughly two-fold changes in *T1* relaxivity [14, 57]. Changes in *T1* induced by these agents are usually detected using gradient-recalled echo (GRE), spin echo (SE), or inversion-recovery (IR) imaging pulse sequences [75]. The *T1* observed in the presence of a smart *T1* contrast agent is given by the approximation, generally valid for low agent concentrations ([M]):

$$\frac{1}{T1(t)} = \frac{1}{T1_0} + R1(t)[\mathrm{M}] \tag{9}$$

where $T1_0$ is the background *T1* in the absence of contrast agent and $R1(t)$ is the time-dependent relaxivity of the contrast agent; $R1(t)$ could also be rewritten as $R1_0 + \Delta R1(t)$, where $R1_0$ is the "resting" relaxivity and $\Delta R1(t)$ is the temporally varying component of relaxivity, typically linked to a phenomenon of interest.

The sampling rate of a time varying *T1*-weighted signal is determined by $1/TR$, where TR is the repetition time of the pulse sequence; entire three-dimensional volumes may be acquired with each repetition if echo planar readout (EPI) is used. The contrast-to-noise ratio (CNR) of a GRE or SE imaging method designed to detect changes in *T1* is maximized when TR equals $\langle T1(t) \rangle$, the average value of *T1* over time, and when Ernst angle radiofrequency (RF) excitation is used [in a GRE pulse sequence, this means that the flip angle α would be set equal to $\cos^{-1}(\exp\{-TR/T1\})$]. In contrast, the temporal resolution of a *T1*-weighting scheme is maximized when the RF flip angle is set to $\pi/2$—only under this condition is the signal observed at each time point independent of the *T1* observed in the previous acquisition. For the same reason, GRE or SE imaging with $\pi/2$ excitation achieves better temporal resolution than IR imaging, despite the advantages of IR for measurements of absolute *T1*. Figure 2 demonstrates these effects in simulated *T1*-weighted signals acquired with $\pi/2$ and Ernst angle GRE, and with standard IR pulse sequences. Practical consequences of the sensitivity of dynamic *T1*-weighted imaging to flip angle are that SNR sacrifices may be required to optimize temporal resolution, particularly for short *TR* values, and that spatially-varying RF excitation (*e.g.* produced by a surface coil) is likely to produce inhomogeneous temporal dependence.

With *T1*-weighted GRE or SE acquisition (echo time << *T2*, *TR*) and ideal $\pi/2$ pulse excitation, the relative signal (I_n) at the end of the nth acquisition period is given by:

$$I_n \propto 1 - \exp\left\{ -\int_{t_{n-1}}^{t_{n-1}+TR} \frac{1}{T1(t)} dt \right\} \tag{10}$$

where t_{n-1} and t_n ($= t_{n-1} + TR$) are the RF excitation times preceding the (n-1)th and nth acquisitions, respectively. The recorded *T1*-weighted MRI signal therefore reflects the history of *T1* between each RF excitation and the next, so contributions from instantaneous events cannot be recognized with temporal resolution better than that defined by *TR*. Assuming ideal flip angles are used, the time resolution of a *T1*-weighted molecular imaging experiment will therefore be limited by the smallest *TR* consistent acceptable MRI contrast changes given the amount of *T1* change produced by the contrast agent and the noise level of the scanner.

Response rates of* T1*-based MRI sensors. *T1* contrast agents are typically organic complexes containing a paramagnetic metal ion such as gadolinium (Gd), which strongly promote the relaxation of the water protons due to the influence of unpaired electron spins of the metal ion. Factors that are important in determining the relaxivity of a contrast agent (reviewed in [66, 76]) are contained in the Solomon-Bloembergen-Morgan (SBM) equations; these include timescales for various molecular motions, structural features of the contrast agent, and spin properties of the paramagnetic metal ion. Some of these properties can be manipulated in such a way as to produce a change in relaxivity coupled to specific events. Among them are the coordination number of the water molecules, q, the lifetime of the water molecule in the complex, τ_m, and the rotational correlation time of the whole complex, τ_R. If one of these parameters differs significantly between two "states" or conformations of a contrast agent, the intensity of the signal observed with MRI is also changed. The timescale on which the change occurs is strongly dependent on the type of the contrast agent and which property has been affected.

The best explored class of *T1* contrast agents relies on the change in solvent exposure to the paramagnetic metal ion (Figure 1A) [77]. The resting state of the contrast agent usually has relatively low relaxivity, with limited water access to the metal ion. The contrast agent is switched into a state of higher relaxivity by a biochemical trigger, such as the activity of an enzyme or a spike in concentration of an intracellular messenger. Several agents that work by this type of mechanism have been reported in the literature. Louie *et al.* [57] synthesized a caged contrast agent called EgadMe, which is a substrate for the enzyme *β*-galactosidase. The activity of β-galactosidase uncages the agent by cleaving a galactopyranosyl group, exposing a Gd coordination site to raise the agent's effective q from 0.65 to 1.02; this structural change in turn gives rise to an increase in $T1$ relaxivity from 0.903 to 2.72 mM^{-1} s^{-1} (measured at 11.7 T). Like many enzymes, β-galactosidase obeys so-called Michaelis-Menten kinetics, meaning that the rate of product formation depends on parameters k_{cat} and $K_m$in the following equation:

$$V = \frac{k_{\text{cat}}[\text{E}]_0[\text{S}]}{K_{\text{m}} + [\text{S}]} \tag{11}$$

where $[E]_0$ is the total enzyme concentration, [S] is the substrate (caged contrast agent) concentration, and V is the rate of uncaged product formation in moles per second. The cleavage of EgadMe takes place with a k_{cat} of 2.4 x 10^{-3} nmol U^{-1} s^{-1} and a K_m of 0.0182 mM; this means for example that a 100 μM concentration of the agent would require on the order of several minutes to be cleaved by 100 U/mL (~ 1 μM) of β-galactosidase. Enzymes most likely to be useful for activating contrast agents are those that cleave carbon-carbon, carbon-nitrogen, or carbon-oxygen bonds; these typically have a k_{cat} significantly smaller than 1 s^{-1}, and are therefore likely to process their substrates over time scales much longer than the TR of a typical $T1$-weighted imaging sequence. In these cases, the temporal resolution of the method would be limited by the enzyme activity level, although with large enough enzyme and substrate concentrations the onset of enzyme activity might be recognized with TR-limited precision.

Faster relaxivity changes are likely to be produced by ion-sensing MRI contrast agents. Sensors for calcium and for zinc have been produced [14, 64]; as with EgadMe, they respond to their targets with conformational changes that expose a bound gadolinium atom to water. $T1$ relaxivity changes from 3.26 to 5.76 mM^{-1} s^{-1} (11.7 T), and from 4 to 6 mM^{-1} s^{-1} (7 T), for the calcium and zinc sensors, respectively. No kinetic data is available for either of these contrast agents, but because their mechanisms are somewhat similar to small fluorescent ion sensors, the response rates of these sensors may be relevant. In particular, the calcium sensitive agent synthesized by Li *et al.* has similar affinity and calcium-liganding groups to Fura-2 and related BAPTA-based "fast" calcium sensors. These dyes have measured k_{on} for calcium on the order of 10^9 M^{-1} s^{-1} [78]. Assuming an MRI calcium sensor had an equivalent k_{on} and a K_d of 1 μM, and if it was used at a concentration of 100 μM to detect (buffered) calcium concentration fluctuations between 0.1 and 2 μM, its overall response rate would be limited by dissociation, and would likely be close to a millisecond. This rate is two orders of magnitude below practical *TR* values. Time resolution in imaging experiments using MRI ion sensors would therefore be determined by the repetition rate of the imaging procedure.

Another method shown to enhance the relaxivity of a *T1* contrast agent is to increase its rotational correlation time, τ_R. For small molecules, τ_R dominates the total correlation time (τ_C), a parameter that enters into the SBM equations and strongly influences the magnetic field dependence of *T1* relaxivity. Since

$$\tau_R = 4\pi a^3\eta/3k_BT \qquad (12)$$

where k_B is the Boltzman constant, changes in τ_R could be effected either by manipulating the viscosity (η) or temperature (T) of the system, or by changing the effective radius (a) of the contrast agent. MRI contrast changes due to changes in the τ_R of a *T1* agent are sometimes dramatic, and sensors involving changes in τ_R (Figure 1B) may be particularly valuable for dynamic imaging at today's most common clinical scanner field strengths ($\leq$3 T).

Sherry and colleagues followed these principles and designed a paramagnetic peptide (Gd^{3+}-G80BP) that senses its protein target (Gal80) by binding to it [79]; a related, but enzyme-dependent approach was taken in a study by Aime *et al.* [62]. In the Gal80/Gd^{3+}-G80BP case, association produces a roughly 25-fold increase in τ_R, corresponding to the ratio of Gal80-complexed to free peptide molecular sizes (here assuming equal density). At 0.5 T, the binding reaction produced a *T1* relaxivity change from 8.3 mM^{-1} s^{-1} to 44.8 mM^{-1} s^{-1}. Protein-protein association rates tend to be on the order of 10^6 M^{-1} s^{-1} [80, 81], meaning that a high-affinity binding reaction initiated by 10 μM concentrations of dissociated species might approach its equilibrium with a characteristic time on the order of 0.1-1 s. Dissociation rates for this type of interaction vary widely, but will be slower for complexes with $K_d << 10^{-5}$. Because these time scales are on the order of typical *T1*-weighted MRI TR values, sensors based on protein binding-induced changes in τ_R may often, but not always, respond with rates that are limiting for the temporal resolution of a dynamic MRI experiment.

Dynamic imaging with SPIO aggregation-based *T2* agents

Temporal resolution of* T2*-weighted imaging. An endogenous *T2* contrast agent (deoxyhemoglobin) and an exogenous blood-pool contrast agent (mononuclear SPIO, or MION) have been heavily used in dynamic functional brain imaging experiments (fMRI), where contrast and temporal resolution are governed by hemodynamic effects [82, 83]. Smart iron oxide agents have also been introduced and applied in cell labeling, cell tracking, and molecular sensing [15, 84]. Although they are physically large (10-100 nm), an advantage of SPIO agents is that they have high relaxivities (10-100 mM^{-1} Fe s^{-1}), and are detectable at very low particle concentrations—several orders of magnitude below concentrations required for most *T1* agents [85, 86]. SPIO agents also produce magnetic susceptibility variations that may be visualized even at fairly low spatial resolution by *T2**-weighted imaging.

T2-weighted imaging is usually performed using SE pulse sequences, sometimes in conjunction with Carr-Purcell-Meiboom-Gill (CPMG) readout [75]. GRE sequences can be used to produce related *T2**-weighted images. Contrast is established during the echo time (*TE*) of these sequences, or across multiple echo times with CPMG. Assuming *T1* and *TR* are static or that *TR* >> *T1*, the relative *T2*-weighted signal in a single-echo (GRE) sequence is given by:

$$I_n \propto \exp\left\{-\int_{t_n}^{t_n+TE} \frac{1}{T2(t)}\,dt\right\} \tag{13}$$

where *T2* is affected by the *T2* contrast agent's relaxivity (*R2*) according to:

$$\frac{1}{T2(t)} = \frac{1}{T2_0} + [R2_0 + \Delta R2(t)][\mathrm{M}] \tag{14}$$

where $T2_0$ is the background *T2*, $R2_0$ and $\Delta R2(t)$ are the static and time-dependent components of *T2* relaxivity, respectively. Because echo times are usually short (10-100 ms), and necessarily less than *TR*, the temporal "precision" of *T2*-weighted imaging can be considered to be higher than that of *T1*-weighted imaging. On the other hand, unless CPMG or phase-locking strategies are used, the image sampling rate is still limited by *TR*, and very short *T2* changes may be missed entirely with probability (1 - *TE*/*TR*), even if they would be likely to produce a signal change when sampled optimally. A clear advantage of scan series data obtained with *T2*-weighted imaging sequences, however, is that their time dependence does not depend on the RF flip angle.

SPIO aggregation sensors. Several types of *T2* relaxation-promoting smart contrast agents have been produced. Of these, agents based on the aggregation of biocompatible SPIO nanoparticles demonstrate the largest relaxivity changes, and appear to be easily tailored to a variety of applications [15]. Superparamagnetic sensors are formed by functionalizing the surfaces of SPIOs with molecules (usually biomolecules, *i.e.* proteins or nucleic acids) that associate with complementary groups on other SPIOs, either when activated in some way, or when bridged by a particular target molecule of interest. Because the particles are multivalent, this binding or bridging induces formation of aggregates, somewhat similar to the process of immunoprecipitation. Aggregation can dramatically amplify the transverse relaxivity of SPIOs, significantly reducing the *T2* relaxivity even of very dilute SPIO suspensions (< 10 mg/L Fe). Ralph Weissleder and colleagues pioneered this approach and have applied it to make MRI sensors for specific oligonucleotides, protease and nuclease activity, and protein-protein binding, including antibody/epitope recognition [15, 87]. Our group has adapted the approach to construct an SPIO bioconjugate sensor for calcium [88].

The strong *T2* effects produced by SPIO sensors make these contrast agents potentially attractive tools for dynamic MRI studies *in vivo*. Little is currently known, however, about the response dynamics of aggregation-based sensors. Most of the existing SPIO sensors appear to respond to their targets on a several-minute time scale, though some enzyme-dependent variants are slower. It is currently unknown to what extent design characteristics of the sensors affect rates of aggregation and concomitant relaxivity changes. Given the relative absence of experimental data related to biofunctionalized nanoparticle aggregation kinetics, we here explore theoretical determinants of SPIO aggregation dynamics in some detail through computational modeling, with the goal of identifying key parameters affecting the time courses and extents of aggregate formation. In addition, we apply a rudimentary approach to approximating changes in *T2* relaxivity produced by SPIO aggregates; this allows us to convert calculated aggregation times into estimated MRI signal changes.

Model of SPIO aggregation behavior. To model physiologically-induced SPIO aggregation dynamics, we considered the following reaction scheme:

$$\mathrm{A} + \mathrm{B} \xrightleftharpoons{\text{activation}} \mathrm{A}^* + \mathrm{B}^* \xrightleftharpoons{\text{aggreg.}} \frac{\sum_{i,j} C(i,j)\mathrm{A}_i^*\,\mathrm{B}_j^*}{\sum_{i,j} C(i,j)} \tag{15}$$

where A and B denote two types of bioconjugated SPIO nanoparticles with different functional groups. Under resting or baseline conditions, the groups on A and B particles have minimal binding affinity for one another. When one or both of the two types of functional groups are activated (converting A to A* and B to B*), their binding affinity increases, initiating the process of particle aggregation. The end-product of the aggregation is a distribution of clusters [denoted by the summation ratio on the right hand side of Eq. (15)] with compositions $\mathrm{A}_i^*\mathrm{B}_j^*$ and concentrations $C(i, j)$, where i is the number of A-type particles and *j* is the number of B-type particles in a given aggregate of total size $i + j$. Disaggregation can be induced by deactivating the functional groups, causing dissociation at the molecular level; here we assume that dissociation need not precede deactivation. For simplicity, we also assume that the activation and deactivation steps happen much faster than aggregation and disaggregation. In many cases, this is a reasonable approximation, given the relatively slow timescales for aggregate (dis)assembly (1-1000 seconds) compared to the time scales of potential (de)activation events (*e.g.* milliseconds for Ca^{2+}-induced protein conformational changes). Some triggering events, like enzymatic proteolysis, might be much slower however, in which case the fast-activation condition would be violated and the model we develop would have to be modified.

Aggregation phenomena are commonly formulated using the Smoluchowski equation [89], a general differential equation describing the formation and fragmentation of various size aggregates. The Smoluchowski model assumes that every transition in the system involves either the break-up of an aggregate into two smaller species, or the agglomeration of two aggregates into a larger cluster:

$$\begin{aligned}\frac{dC(u,v)}{dt} &= \frac{1}{2}\sum_{i=0}^{u}\sum_{j=0}^{v}K_{agg}(i,j,u-i,v-j)C(i,j)C(u-i,v-j) \\ &-\frac{1}{2}\sum_{i=0}^{u}\sum_{j=0}^{v}K_{frag}(i,j,u-i,v-j)C(u,v) \\ &-\sum_{i=0}^{z-u}\sum_{j=0}^{z-v}K_{agg}(i,j,u,v)C(i,j)C(u,v) \\ &+\sum_{i=0}^{z-u}\sum_{j=0}^{z-v}K_{frag}(i,j,u,v)C(u+i,v+j)\end{aligned} \qquad (16)$$

Here, $C(u, v)$ is the concentration of aggregates that contain u particles of type A and v particles of type B. The coefficients K_{agg} and K_{frag} are "kernels" for aggregation and fragmentation—they function like rate constants, and reflect the probability that aggregates of size (u, v) will be formed by or broken into clusters of all other allowed sizes. The first term of equation (16) is the instantaneous rate at which aggregates of composition (u, v) are formed through the binding of all possible pairs of smaller aggregates. Similarly, the second term accounts for the breakup of (u, v) clusters into all possible smaller fragment pairs. The third term is the rate at which aggregates of composition (u,v) bind to other clusters. The final term is the rate at which (u, v) clusters break off from larger aggregates of size $(u + i, v + j)$. K_{agg} and K_{frag} were adapted from the literature [73, 74] in order to reflect the scenario in Eq. (15). As is common in other models, our approach assumed that the aggregates are fractal (irregular at all length scales) and non-circular (any two particles are connected through only one chain). These assumptions are valid for rigid particles with small (protein-sized) functional groups tightly anchored to the particle surface. See the Methods for further details.

In order to simulate the aggregation of SPIOs, we used Euler integration to obtain mass-action solutions to Eq. (16). Figure 3A shows representative aggregation and disaggregation time courses produced by our simulations. We depict both the mass-averaged mean particle radius $\langle r \rangle$ (relative to an individual particle), and the mass-averaged mean aggregate size $\langle n \rangle$ as functions of time. The corresponding steady-state distribution (limit at infinite time) of aggregate sizes and compositions is shown in Figure 3B. These time courses and distributions are consistent with results from previous Monte

Carlo simulations and experiments involving general reversible aggregation phenomena [74, 90]. To facilitate the comparison of time courses for varying sets of parameters, we defined an "apparent" aggregation time constant T_{obs} as the value for which $[\langle n\rangle(T_{\mathrm{obs}}) - \langle n\rangle(0)]$ equals $(1-1/e)[\langle n\rangle(\infty) - \langle n\rangle(0)]$, where $\langle n\rangle(\infty)$ is the steady state value of $\langle n\rangle$ (as t goes to infinity), for an aggregation process initiated at $t = 0$.

Our simulations investigated the dependence of T_{obs} and $\langle n\rangle(\infty)$, on the total nanoparticle concentration, the number of functional groups per particle and the concentration ratio of complementary particles. The results, shown in Figure 3C, demonstrate a generally non-linear dependence of T_{obs} and $\langle n\rangle(\infty)$ on these parameters. As concentration increases, both the rate of approach to equilibrium and the steady state size rise in a supralinear fashion (panel C*i*), as would be expected for a multi-body process. For increasing number of functional groups per particle, T_{obs} approximates an inverse exponential dependence, while $\langle n\rangle(\infty)$ increases roughly linearly (panel C*ii*). As shown in panel C*iii*, the maximal aggregation rate and size are found when the concentrations of complementary particles are equal. Overall, these results suggest that the kinetics of aggregation are highly sensitive to the particulars of their design and deployment, with aggregation times varying over three orders of magnitude within a feasible concentration and functionalization range. At the higher end of this range, theoretically achievable aggregation times are as short as several seconds.

As shown in the sample time courses of Figure 3A (gray regions), disaggregation upon the removal of the activating physiological stimulus can occur on time scales considerably faster than those seen for aggregation. However, the rate of disaggregation can vary widely depending on the specific deactivation mechanism. For example, given an allosteric mechanism where activation and deactivation of particle functional group(s) can occur in both bound and unbound states, deactivation can be expected to increase dramatically the bimolecular dissociation rate k_{off} (in addition to reducing k_{on}), leading to fast disaggregation. By contrast, if the functional group(s) can only be deactivated in the unbound state, k_{off} remains unchanged for bound particles, resulting in a much slower disaggregation process. In general, at low nanoparticle concentrations, we expect disaggregation to occur faster than aggregation, making aggregation the limiting factor in the reversible response rate of an aggregation-based sensor.

It should also be noted that the rates of aggregation and disaggregation in biological tissues (*e.g.* cell cytoplasms) may be significantly slower than the rate observed in solution [91]. Experiments have shown that molecular crowding in the cellular milieu reduces the effective diffusivity of solutes in a size-dependent manner, decreasing it by roughly a factor of four for most biological molecules, and by a factor of 40 or more for particles with diameters above a 50-80 nm threshold. Single SPIOs in the 30 nm size range should fall below this threshold, but aggregates larger than a certain size will be above it. Since under many conditions monomers are the single most common species in the aggregation reaction, it may be possible to roughly approximate the slowing of aggregation in the cellular environment by dividing the Brownian diffusivity constant by around a factor of four (here we assumed that diffusion of each aggregate was determined by the Stokes-Einstein equation only).

SPIO aggregation-induced changes in relaxivity. The model developed above makes predictions about the dependence of SPIO aggregation rate on various parameters of MRI sensors; aggregation time constants are likely to vary from several seconds to many minutes, depending on concentration, functionalization, monomer ratio, and, in biological environments, size. But how is the aggregation rate of these particles likely to translate into MRI-observable signal changes? Although strong changes in *T2* relaxivity upon aggregation of SPIOs have been reported, little work has been done to explain the mechanism of aggregation-induced contrast change. Previous theoretical analyses, Monte Carlo simulations, and experimental work have shown that the *T2* relaxivity of iron oxide nanoparticles is well-described by the motional averaging approximation when mean Larmor frequency shift at the particle surface ($\Delta\omega$) and the time constant for water diffusion around the particle (τ_d) satisfy the condition $\tau_d\Delta\omega < 1$ [31, 92]. This condition is fulfilled for uncoated iron oxide crystals smaller than approximately 30 nm. For coated SPIOs such as MION-46 [93], which contains a crystalline core of around 5 nm diameter surrounded by an organic shell of roughly 10 nm thickness, this maximum size for motional averaging is relaxed to around 350 nm, due to a lower field strength at the particles' water-accessible outer surfaces.

In the motional averaging regime, outer sphere theory predicts the component of *T2* relaxation due to a suspension of field-perturbing SPIO particles to be given by:

$$1/T2_{\mathrm{SPIO}} = (4/9)V(\Delta\omega)^2\tau_d \tag{17}$$

where V is the volume fraction of solution occupied by the particles, τ_d is defined as $\tau_d = r^2/D$, where r is the particle radius and D is the self-diffusion coefficient of water, and $\Delta\omega$ is given by $\Delta\omega = (1/3)\mu_0\gamma M$, where M is the particle magnetization, μ_0 is the free space magnetic permeability, and γ is the proton gyromagnetic ratio.

For aggregate sizes below the motional averaging cutoff, Eq. (17) and the definition of τ_d predict an increase in relaxivity proportional to the square of aggregate radius. For fractal aggregates, the relationship between the number of particles in the aggregate (n) and its radius of gyration (r) is:

$$r \propto n^{1/df} \tag{18}$$

where df is the aggregate's fractal dimension. Typically, df is between 1.75 and 2.3 in fractal aggregates [94, 95], with reaction-limited aggregation (see above) resulting in larger df.

In addition, Eq. (17) and the definition of $\Delta\omega$ predict a quadratic dependence of relaxivity on particle magnetization, M. At field strengths above 1 T, SPIO magnetic moments are known to be saturated [93]. Under these conditions, M is field-independent and roughly proportional to ρ, the density (number of particles within the volume defined by r) of a given aggregate:

$$M \propto \rho \propto \frac{n}{r^3} \propto r^{df-3} \propto n^{1-\frac{3}{df}} \tag{19}$$

Because V and D are independent of aggregation state, we can combine Eqs. (17-19) to obtain a set of proportionalities:

$$1/T2_{\mathrm{SPIO}} \propto \rho^2 r^2 \propto r^{2df-4} \propto n^{2-\frac{4}{df}} \tag{20}$$

Since at (typical) low SPIO volume fractions $1/T2_{\mathrm{SPIO}}$ is approximately equal to $R2$ times the particle concentration [*cf.* Eq. (14)], Eq. (20) predicts an increase in $T2$ relaxivity with increasing aggregate size when the fractal dimension is greater than 2. In the limiting case where aggregates are composed of fully-packed spherical particles ($df = 3$) the proportionality reduces to an r^2 dependence.

We simulated fractal aggregates with $df = 2.2$, which is on the high end of the reaction-limited aggregation regime. This choice of df is somewhat arbitrary, and one would expect the fractal dimension to vary considerably depending on the details of particle geometry and functionalization. Although variation of df within the typical range would have a large effect on predicted relaxivity, our simulations demonstrated that it had a negligible effect on kinetics (data not shown). For aggregates with $df = 2.2$, relation (20) predicts a relaxivity proportional to $n^{2/11}$. In order to characterize the relaxivity of a given population of aggregates, we therefore calculated the mass average of $n^{2/11}$ and scaled it by the known single-particle relaxivity.

Figure 4A shows the temporal evolution of relative relaxivity (normalized by the unaggregated particle relaxivity) and corresponding percent change in MRI signal intensity during the SPIO aggregation and disaggregation time courses shown in Figure 3A. Signal intensity was calculated by assuming a baseline $T2$ for the medium of 100 ms and setting the TE to the $T2$ observed in the presence of non-aggregated SPIOs. Figure 4B shows the predicted apparent time constant (T_{obs}, defined as above) of the change in MRI signal intensity, along with the maximal steady-state signal change, as a function of particle concentration. These results suggest that single-second temporal resolution may be possible for aggregation sensors with particle concentrations in the 20-100 nM range, but that lower SPIO concentrations will lead to considerably slower response rates. From a practical standpoint, it is also useful to know how long it takes the aggregation-induced signal change to reach a minimal detection threshold. We defined $T_{5\%}$ to be the time it takes to obtain a 5% change in signal, during aggregation of initially fully disaggregated particles. Figure 4B shows that at high concentrations, $T_{5\%}$ is predicted to be of order 0.1 s, but that at lower concentrations, where 5% is close to the maximal signal change, $T_{5\%}$ is close to 100 s, and actually longer than T_{obs}.

Time-resolved imaging with CEST agents

Temporal resolution of CEST-based imaging. The chemical exchange saturation transfer (CEST) effect [13] has recently been explored as a basis for MRI contrast agents because of its potential independence of paramagnetic metal complexes and possible advantages in sensitivity compared with some *T1* contrast agents. CEST contrast enhancement is achieved by selectively saturating the proton magnetization of a small pool of labile protons associated with a CEST agent; these protons exchange with bulk solvent, producing a decrease in the bulk magnetization that gives rise to the detected MRI signal. CEST techniques have been applied to produce contrast changes *in vitro*, using a variety of agents including paramagnetic lanthanide complexes (PARACEST agents) [96]. CEST contrast changes have also been created *in vivo* using saturation of amide protons of endogenous proteins or exogenous species [17, 18]. With CEST-based sensors, the efficiency of saturation transfer from the agent depends on select features of the agent's chemical environment, giving rise to modulations in detected MRI intensity that could in principle be followed in a dynamic imaging experiment.

In CEST MRI, saturation transfer to longitudinal bulk magnetization takes place during a presaturation period *TP*, after which RF excitation is delivered and any CEST-related changes in bulk magnetization are measured with a standard readout module (GRE, SE, EPI, *etc.*). Usually *TP* is set to be almost as long as *TR*, in order to maximize CEST contrast for the given repetition rate. Observed CEST-dependent magnetization is influenced by the inherent spin-lattice relaxation rate of bulk water protons ($1/T1_w$), by the time constant (τ_m) for chemical exchange between CEST and bulk proton pools during the presaturation time, and by the efficiency and dynamics of the saturation itself. With a smart CEST contrast agent, τ_m and the saturation efficiency could depend on the configuration of the agent and would become time-dependent variables.

Analytical expressions for CEST-dependent MRI signal changes can be obtained under various simplifying assumptions [68, 71]. A reasonable assumption is that the magnetization of the CEST pool reaches a steady state very rapidly during saturation (*i.e.* much faster than *TP*). A further approximation is that RF irradiation of the CEST pool does not directly saturate the bulk proton pool—this is true when the RF offset ($\Delta\omega$) between the bulk water frequency (ω_1) and CEST pool frequency satisfies: $\Delta\omega/\omega_1 >> 1$. If these two conditions are met, and the steady-state partially-saturated magnetization of the CEST proton pool is given by $(1 - \alpha)M_{0s}$ (with M_{0s} being the equilibrium magnetization of the saturated CEST pool and α the fractional saturation of this pool), the following differential equation describes the evolution of bulk proton magnetization during *TP*:

$$\frac{dM_{zw}(t)}{dt} = \frac{(M_{0w} - M_{zw})}{T1_w} - \alpha \frac{M_{zw}}{\tau_w} \tag{21}$$

□□□□□ $\tau_w = 111\tau_m/c$, where c is the concentration of exchange sites on the CEST agent, and given a bulk proton concentration of 111 M. Assuming perfect RF flip angles (see $T1$ discussion above) and ideal CEST-weighting ($TE \ll T2 < TR \sim TP$), a formula for relative signal observed in a serial imaging experiment can be obtained by integrating Eq. (21) over TP, with the initial condition that bulk magnetization is transverse ($M_{zw} = 0$) before saturation begins:

$$I \propto \frac{\tau_w}{\tau_w + \alpha T1_w} - \frac{\tau_w}{\tau_w + \alpha T1_w} \exp\left\{ -\frac{\tau_w + \alpha T1_w}{\tau_w T1_w} TP \right\} \tag{22}$$

If a CEST-based MRI sensor was being used, terms in Eq. (22) would be replaced with integrals over TP, similar to Eqs. (10) and (13) (omitted here for notational simplicity). Because CEST contrast develops during the entire saturation period, the temporal resolution of a CEST experiment cannot exceed $1/TP$. In analogy to the role of TR in $T1$-weighted molecular imaging, the requirement that TP be long enough to obtain sufficient CNR therefore sets a practical limit on the repetition time for MRI time series using CEST-based sensors.

Figure 5 shows a contour plot of ideal CEST signal changes as a function of TP and τ_m, assuming a CEST agent is “turned on and off” with each image acquisition. The plot was calculated using Eq. (22), and overestimates signal change for cases where the RF offset ($\Delta\omega$) between the bulk water frequency (ω_l) and the saturated pool fails to satisfy $\Delta\omega/\omega_1 >> 1$, when $\Delta\omega$ and the proton exchange time fail to obey $\tau_m\Delta\omega >> 1$, or when $\alpha < 1$ (as often expected under practical saturation powers). For any given noise level, the signal changes reported in the figure suggest realistic limitations on scan rate. The well-known dependence of the CEST effect on τ_m translates into faster possible time resolution for agents where saturation transfer changes occur around smaller τ_m values. The plot extends to τ_m's less than 10 μs, which have been reported for exchanging sites on some lanthanide complexes; at field strengths below 10 T, however, application of these complexes is likely to be compromised by the requirements on $\tau_m\Delta\omega$. As with *T1*-weighted imaging, the use of nonideal flip angles could degrade the temporal resolution below the CNR-dependent limit, by compromising the independence of each MRI acquisition. Temporal resolution could also be degraded if the CEST pool magnetization were not maintained near its steady-state value at all times, but we found no evidence of this in magnetization evolution simulations covering a broad range of conditions.

Response rates of CEST-based sensors. CEST agents have been used as MRI sensors for pH, lactate, and glucose [18, 60, 61, 65, 67]. In all cases, the response rates of the sensors are likely to be extremely fast compared with the demands of the imaging method itself. CEST-based pH sensing is simplest to appreciate, given the well-known dependence of proton exchange rates on pH. Amide protons of endogenous proteins, and of two synthetic lanthanide complexes, have been used for pH-sensitive CEST [17, 18, 60]. Amide τ_m ranges from roughly 10^{-3} s^{-1} at pH 3 to 10^{3} s^{-1} above pH 9 [97], creating a change in saturation transfer efficiency. The response rates to pH are likely to be extremely fast, though they have not been measured directly on the contrast agents. Rate constants for proton association reactions in general are thought to be on the order of 10^{10} to 10^{11} M^{-1} sec^{-1} [98]. Base-catalyzed exchange is most common in the physiological pH range (pH 5-8) [17]; under base catalysis, the association and dissociation rate constants for glycine amide proton exchange (similar to the CEST pH sensor DOTAM-Gly) are roughly 1.4×10^{11} and 8.44×10^{5}, respectively [98]. Given these rates, it is likely that the response of CEST agents to pH changes takes place within a few microseconds. This time scale is negligible compared with the duration of presaturation pulses used to measure pH changes from agent concentrations even over 10 mM.

A related mechanism underlies low affinity glucose detection by a complex synthesized by Zhang *et al.* [67]. The unliganded form of the sensor functions efficiently as a CEST agent, due to exchange of water molecules at a free europium coordination site. In the presence of glucose (K_d = 2.6 mM), the exchange site is partially blocked (*cf.* Figure 1A), leading to a noticeable reduction in CEST efficiency when saturation is delivered at a –30 ppm RF offset. A somewhat different mechanism allows CEST-based lactate sensing by an agent called MBDO3AM [65]. In its free state, this lanthanide adduct contains six amide protons, all of which overlap to give rise to a high field-shifted proton resonance peak at –28.5 ppm. When lactate is added at relatively high concentrations (the dissociation constant is over 100 μM), the degenerate resonance is resolved into discrete peaks in a lower field frequency range, -14 to –20 ppm. If saturation is selectively directed either at the free MBDO3AM amide peaks, or at the complexed-form amides, a change in CEST saturation efficiency results from binding of the lactate to the contrast agent. With neither the glucose nor the lactate sensor are kinetic parameters describing the metabolite/sensor binding interaction known, but by analogy with other bimolecular binding pairs, the association rates are likely to be well over 10^5 M^{-1} s^{-1}, implying that the dissociation rates are at least 10 s^{-1}. Even given these conservative estimates, the kinetics of intermolecular interactions that underlie CEST-based lactate and glucose sensing are still significantly faster than the time scale used to build up CEST contrast, which was on the order of several seconds in these studies.

Comparison of dynamic molecular MRI methods

Figure 6 presents a comparison of temporal resolutions for dynamic imaging approaches using smart *T1* contrast agents, SPIO aggregation-based *T2* sensors, and CEST agents. For each of the three groups of molecular imaging agents we considered, a colored area denotes approximate conditions under which acceptable signal changes may be achieved, assuming realistic MRI acquisition conditions. This representation is a guideline only; it is by necessity highly reductionist, because the full range of relaxivities and interconnected trade-offs between CNR, repetition rate, spatial resolution, partial volume effects, and signal averaging are impossible to address simultaneously in graphical form. Roughly speaking, we assume that a 5% signal change is sufficient for detection of an agent's response in a time-resolved experiment. This requirement is lower than the standard generally required in contrast agent-enhanced anatomical (static) imaging, but reflects the important possibility, specific to dynamic imaging, of performing statistically-rigorous within-subject comparisons to recognize small image intensity fluctuations. In human fMRI, the dominant form of time-resolved MRI today, signal changes lower than 1% are often robustly detected at the single voxel level.

The "fast" *T1* agent area in Figure 6 (saturated red) was estimated assuming GRE imaging with $\pi/2$ excitation pulses, and a sensor with relaxivity changes on the millisecond or faster time scale, from 5 to 10 mM^{-1} s^{-1}. The region is bounded at the right by concentration levels at which toxicity and *T2* effects may interfere with applications; at low concentrations, signal changes are likely to be below the detection limit. In principle *TR*'s close to 10 ms could be used to obtain even higher temporal resolution than shown, but this would result in severe attenuation of the overall signal, and under typical imaging conditions would be impractical. Very short *TR*'s would also be incompatible with EPI volume acquisition. The "slow" T1 area in light red refers to *T1* agents like the Gal80-binding agent and the β-galactosidase substrate discussed above, for which the molecular rate of response is the limiting factor on potential temporal resolution. The relaxivity changes produced by these sensors are on the same order of magnitude as the "fast" agents, but signal averaging becomes a possibility when time resolution is no longer limiting, so it is likely that somewhat lower concentrations could be used.

The aggregation-based SPIO agents are represented by the green shaded area. For these agents, the temporal resolution in *T2*-weighted imaging is also limited by the sensors' rates of response, rather than by the imaging itself. The region plotted in Figure 6 is estimated based on the theoretical analysis we have performed here; our modeling was consistent with data from the literature, but covered a wider variety of conditions than has yet been experimentally explored. The response times of aggregation-based sensors are predicted to vary approximately linearly from about 100 s at 1 nM SPIO concentration to 1 s at 0.1 μM, for particles with ~50 attached proteins; if the functionalization level is lowered, the rates would be decreased. At SPIO concentrations into the micromolar range, the aggregation effect would be yet faster, but concentrations significantly above 0.1 μM (10 mg/L Fe, assuming 2000 iron atoms per particle) would begin to attenuate the MRI signal too severely, and would be inconsistent with physical echo times.

The blue area in Figure 6 denotes conditions under which dynamic MRI with smart CEST agents could be performed. As our earlier discussion emphasized, the temporal resolutions and concentrations compatible with use of existing CEST-based sensors are completely constrained by the physical requirements of performing imaging with acceptable signal changes. To estimate the region in Figure 6, we performed pulse sequence and magnetization simulations for a 300 μs τ_m CEST agent, under a range of repetition rates and concentrations, with $TP \sim TR$. Signal changes between exchanging ("on") and nonexchanging ("off") conditions were greater than 5% for concentrations above 1 mM and for 1-10 s saturation times. If agents with lower τ_m were used at very high field, it is likely that lower saturation times or concentrations could be used.

A conclusion from this comparison is that the fastest MRI molecular imaging temporal resolution (~100 ms) is likely to be obtained with *T1* agents, while the lowest concentrations (and greatest signal changes) may be reached with SPIO aggregation sensors. Several caveats apply: First, most of our arguments have relied on simulations or calculations performed under idealizing assumptions; some of the findings (especially the aggregation simulations) await empirical validation and may incompletely account for realistic experimental conditions. Second, the discussion has focused on time dependence largely to the exclusion of other factors related to the contrast agents. In an actual dynamic MRI experiment, some agents with inferior "theoretical" time resolution may in fact be preferable for unrelated reasons. Third and last, we have not attempted a comprehensive discussion of all existing or putative smart contrast agents and mechanisms—the specific agents we have addressed were chosen because they are representative or of particular interest.

The guide we present in Figure 6, and the more detailed analyses of the previous sections, give an overview of considerations important to dynamic molecular imaging experiments. Although few such experiments have been reported to date, time-resolved molecular imaging of biologically significant targets (particularly in neuroscience and developmental biology) is clearly an urgent direction in MRI methods development. Quantitative description of contrast agent properties will help direct both the selection of viable experimental strategies, and the design of new smart contrast agents with improved characteristics. Our discussion suggests that high CNR is the most important requirement for optimizing temporal resolution with *T1* agents, where the sensitivity of the MRI methods currently limits acquisition rates. The development of *T2* SPIO agents with enhanced kinetic properties is also clearly recommended, given the low concentrations at which these agents can be used; improved SPIO-based sensors could be produced by maximizing nanoparticle functionalization levels, or by loosely tethering particles to one another in order to speed aggregation.

ACKNOWLEDGEMENTS

The authors gratefully acknowledge comments from G. Odriozola and P. Gillis about the proposed models for nanoparticle aggregation and SPIO relaxivity changes, respectively. David Cory is thanked for helpful remarks on the manuscript. MGS was supported by a Hertz Fellowship and a Soros Fellowship, HF was supported by award DAMD17-03-1-0413 from the Department of the Army, and GGW and AJ were supported by a grant from the Raymond and Beverley Sackler Foundation.

FIGURE LEGENDS

Figure 1. Smart contrast agent mechanisms. Contrast agents have been constructed to respond to physiological targets by a variety of mechanisms. In (A), binding of a target molecule (red) to a paramagnetic chelate (green and gray) increases exposure of the agent's coordinated metal ion (green, usually Gd) to surrounding tissue water (blue), allowing water molecules to participate in inner sphere interactions with the metal, and increasing the agent's *T1* relaxivity. Enzyme and ion-sensitive contrast agents that work this way have been synthesized. (B) Association of a lanthanide chelate (green and gray) with a much larger binding partner (red) results in an increase in rotational correlation time (τ_R) and *T1* relaxivity. (C) The presence of a target molecule (red) induces aggregation of functionalized superparamagnetic nanoparticles (green). Aggregation can induce dramatic changes in *T2*.

Figure 2. Effect of excitation flip angle on *T1* image series. Magnetization trajectories during *T1*-weighted MRI time series were simulated using the Bloch equations. To model the effect of a smart *T1* agent, the *T1* of the system was set to a baseline of 1.0 s, but reduced by a factor of two during a 10 s "stimulus" period (gray boxes). The top two panels show results from a mock gradient echo (GRE) imaging sequence with 0.5 s *TR*, 10 ms *TE*, and 100 ms *T2*, beginning with longitudinal magnetization at equilibrium (= 1.0). The top panel shows the echo peak signal series obtained when perfect $\pi/2$ pulses are used for excitation: a transition in signal level takes place sharply after the change in *T1*. The middle panel shows the effect of Ernst angle excitation. Although the overall

signal level is higher, the increase in signal after *T1* decreases is slower. In the bottom panel, an inversion-recovery sequence is simulated with a 0.5 s recovery time and 1.0 s *TR*. As with Ernst angle GRE imaging, the signal at each acquisition is dependent on the previous acquisition, and the new equilibrium signal is reached only two or more acquisitions after a change in *T1*.

Figure 3. Predicted characteristics of nanoparticle aggregation and disaggregation. (A) The temporal evolution of mass-weighted average aggregate size $<n>(t)$ (top) and radius of gyration relative to monomer (bottom) during aggregation and disaggregation. (B) The steady state aggregate size distribution corresponding to $t = 250$ s in (A). The insert shows the composition distribution of the aggregates, with the number of type A and type B particles on the horizontal and vertical axes, respectively. (C) Apparent aggregation time constant T_{obs} (circles) and steady-state mass-weighted average aggregate size $<n>(\infty)$ (squares) for a range of initial monomer concentrations (*i*), functionalization densities (functional groups per particle) (*ii*), and concentration ratios between the complementary particle types (*iii*). Simulation parameters are listed in the Methods section.

Figure 4. Relaxivity changes during SPIO aggregation and disaggregation. (A) The temporal evolution of percent MRI signal change (top) and ratio of net *T2* relaxivity, relative to unaggregated monomer solution (bottom), corresponding to the aggregation time course shown in Figure 3A. (B) Apparent signal change time constant T_{obs} (filled circles), time to reach a 5% signal change $T_{5\%}$ (filled squares), and the steady-state

percent signal decrease (hollow diamonds), as a function of initial monomer concentration.

Figure 5. Computed signal changes in dynamic MRI with CEST agents. Signal changes were calculated using Eq. (22) in the text, by considering the difference between signal in the absence and presence of chemical exchange, assuming complete saturation of the CEST pool ($\alpha = 1$) over a variable saturation period *TP*. Black contours show 5, 10, and 25% signal change levels estimated for 100 μM CEST agent. Signal change contours for 1 mM agent are approximately parallel to these (contour for 5% change shown in gray), with < 5% signal change observed at all *TP* values for low τ_m. A $T1_w$ of 1.0 s was assumed.

Figure 6. Schematic comparison of temporal resolutions for three classes of molecular imaging agent. Colored regions approximate combinations of temporal resolution and contrast agent concentration that would lead to acceptable signal changes (> 5%) with *T1*-weighted (red), *T2*-weighted (green), and CEST (blue) imaging. *T1* agents are subdivided into "fast" agents (saturated red), for which imaging requirements limit the attainable temporal resolution, and "slow" agents (light red), for which properties of the agents themselves are limiting. See text for further discussion.

Figure 1

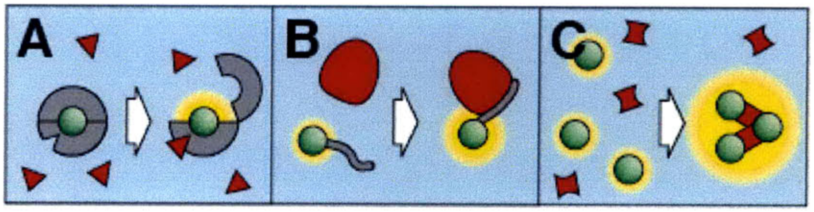

Figure 2

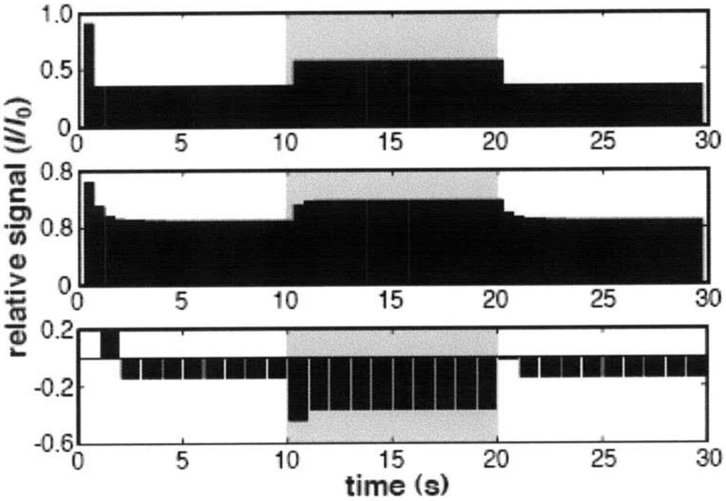
1.0
0.5
0
0
5
10
15
20
25
30
0.8
0.8
0
0
5
10
15
20
25
30
0.2
-0.2
-0.6
0
5
10
15
20
25
30
relative signal (I/I_0)
time (s)

Figure 3

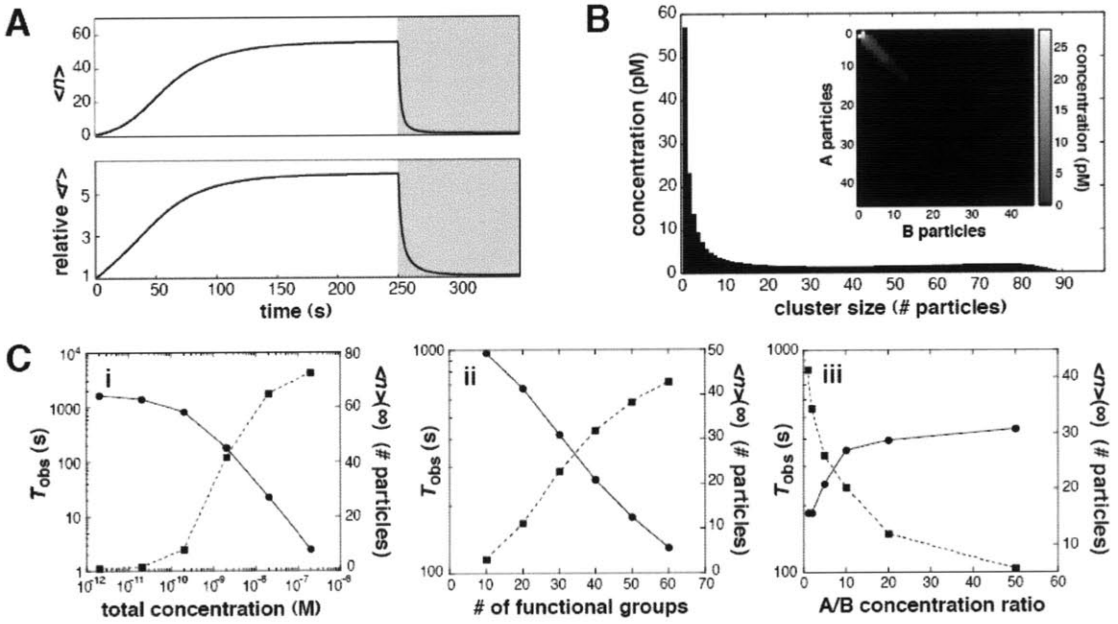
A
<n>
0
20
40
60
relative <r>
1
3
5
time (s)
0
50
100
150
200
250
300
B
concentration (pM)
0
10
20
30
40
50
60
cluster size (# particles)
0
10
20
30
40
50
60
70
80
90
A particles
B particles
concentration (pM)
0
5
10
15
20
25
C
i
T_{obs} (s)
<n>(∞) (# particles)
total concentration (M)
10^{-12}
10^{-11}
10^{-10}
10^{-9}
10^{-8}
10^{-7}
10^{-6}
1
10
100
1000
10^4
0
20
40
60
80
ii
T_{obs} (s)
<n>(∞) (# particles)
# of functional groups
100
1000
0
10
20
30
40
50
60
70
iii
T_{obs} (s)
<n>(∞) (# particles)
A/B concentration ratio
100
1000
10
20
30
40
0
10
20
30
40
50
60

Figure 4

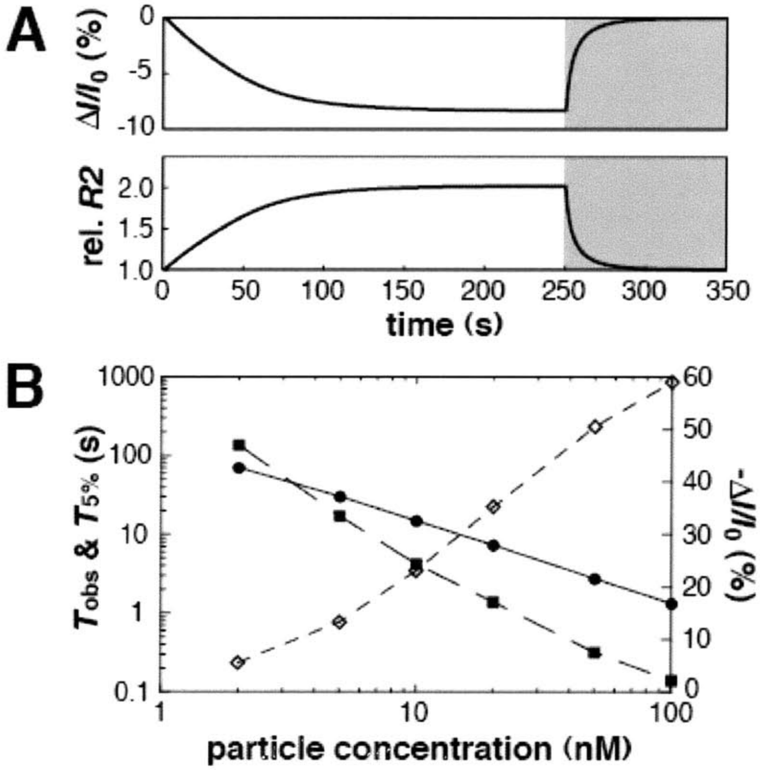
A
ΔI/I0 (%)
0
-5
-10
rel. R2
2.0
1.5
1.0
0
50
100
150
200
250
300
350
time (s)
B
Tobs & T5% (s)
1000
100
10
1
0.1
1
10
100
particle concentration (nM)
-ΔI/I0 (%)
60
50
40
30
20
10
0

Figure 5

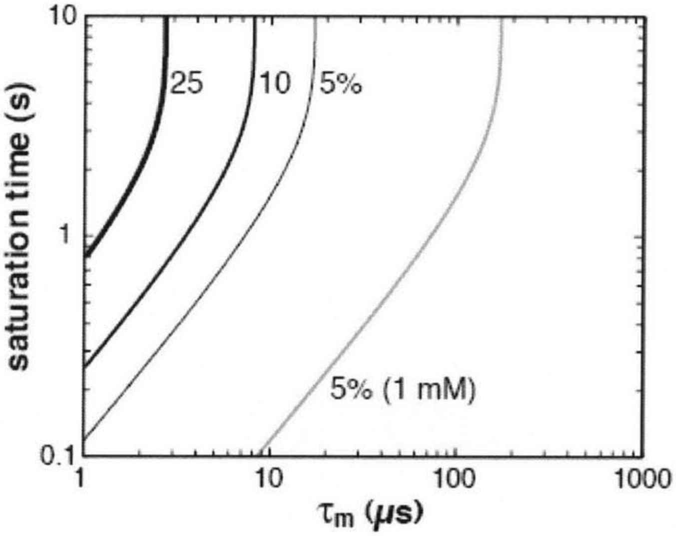

Figure 6

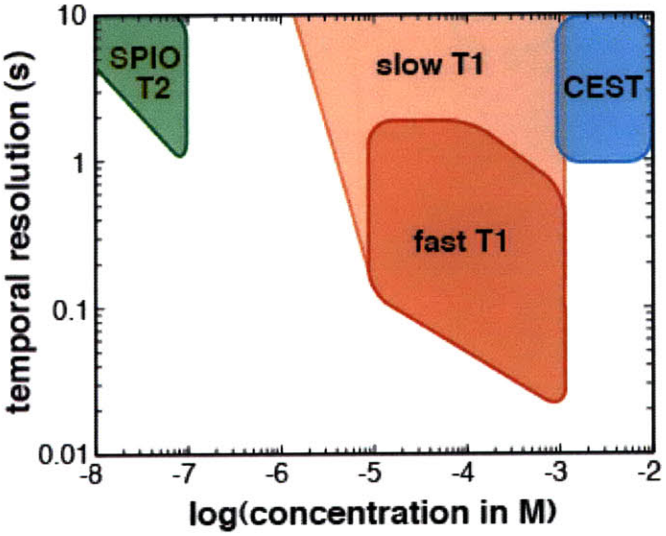
SPIO
T2
slow T1
CEST
fast T1
temporal resolution (s)
10
1
0.1
0.01
-8
-7
-6
-5
-4
-3
-2
log(concentration in M)

3. Protein-based MRI contrast agents engineered to sense neurotransmitter dynamics *in vivo*

ABSTRACT

Progress in biology and medicine could be accelerated using methods for non-invasive molecular imaging of living tissues, but the development and application of imaging agents that could serve this purpose remains a major challenge. Here we applied powerful protein engineering techniques to create a new type of magnetic resonance imaging (MRI) contrast agent sensitive to a critical signaling molecule in the brain, the neurotransmitter dopamine. Multiple rounds of directed evolution were used to identify dopamine-binding variants of the heme domain of the bacterial cytochrome P450-BM3 (BM3h). Engineered BM3h mutants brightened MRI signal in the absence but not the presence of dopamine; little or no interference was observed from other neural signaling molecules. Quantitative measurements of biological dopamine release were obtained and validated *in vitro* using cultured PC12 cells. Intracranial injection of BM3h-based sensors into anesthetized rats produced dopamine-dependent MRI contrast changes and revealed real-time dynamics of neurotransmitter transport with submillimeter spatial resolution. Our approach can be generalized to monitor a wide variety of physiological processes in living organisms.

INTRODUCTION

Discoveries in neuroscience often follow the development of new ways to peer into the active brain. Magnetic resonance imaging (MRI) has become a particularly valuable tool for studying the brain because MRI scans are noninvasive and can provide information at relatively high spatial resolution (< 100 μm) and temporal resolution (~1 s) from living specimens[7]. Powerful MRI-based techniques for studying neuroanatomy and brain function have been established, but the range of neuronal phenomena accessible to measurement by MRI remains limited by the small variety of endogenous signals. One approach to this problem is to develop MRI sensors that respond dynamically to aspects of structure or function in neural tissue; these sensors might act in analogy to fluorescent dyes used for optical imaging studies[99, 100]. Earlier efforts to create MRI sensors have focused on incorporating traditional MRI contrast moieties, such as gadolinium chelates or iron oxide nanoparticles, into complex organic structures or supramolecular assemblies [100], resulting in sensors that are difficult to engineer, synthesize and apply *in vivo*.

Neurotransmitters are prime targets for sensing by new MRI imaging agents. Dopamine (DA) is a neurotransmitter of particular interest because of its role in learning, reward and motor coordination[37]. Dysfunction of dopaminergic systems is implicated in addiction[38] and neurodegenerative diseases[39]. Most measurements of DA release in basic research rely on invasive techniques like microdialysis[40] and voltammetry[41], which report variations of DA concentration at a single site in the brain. Positron emission tomography (PET) is used to monitor DA receptor occupancy and related variables[42].

PET methods are sensitive, but have relatively low spatial resolution (> 1 mm); and because most PET measurements are based on kinetic modeling, they are best suited to studies of chronic conditions or temporal changes that occur on the time scale of many minutes or longer. To build an understanding of how DA functions in brain processing, there is therefore a need to develop measurement techniques that could be applied at a whole-brain level, and that have significantly better spatial and temporal resolution than PET. MRI, in combination with a suitable contrast agent sensor, would help satisfy this need.

No MRI contrast agent for sensing DA (or any other neurotransmitter) has been reported to date, and the specifications for such an agent are strict. DA fluctuations in the basal ganglia of the brain, for instance, take place on the order of seconds, and involve peak DA concentrations $< 100\ \mu M$[43, 44]. A DA sensor must therefore respond quickly, reversibly, and specifically to DA fluctuations in the micromolar range. To be comparable with established functional brain imaging techniques (fMRI), the probe must also be capable of producing image signal changes in tissue on the order of 1% or more[45].

Metalloproteins represent a promising platform for engineering MRI sensors of DA and other small molecules. Many metalloproteins are natural MRI contrast agents because they contain paramagnetic ions that interact with water molecules to accelerate nuclear magnetic T_1 or T_2 relaxation rates, in turn brightening or darkening (respectively) MRI image intensities. Proteins typically offer ample surface area for achieving specificity in ligand binding, are straightforward to produce and deliver exogenously, and may also be delivered indirectly as genes. A variety of rational and evolution-based methods have been developed to engineer protein function. The paramagnetic flavocytochrome protein P450-BM3 from *Bacillus megaterium* (BM3) has become a platform for efforts to tune catalytic activity using so-called "directed evolution" techniques, involving multiple rounds of mutagenesis and high throughput screening. Because of the ease with which its substrate range can be altered, BM3 is an especially promising starting point for engineering of new MRI sensors. We show here that by applying a novel directed evolution approach to BM3, we have been able to isolate MRI contrast agents suitable for DA sensing *in vivo*.

RESULTS

Natural and unnatural ligand binding to the BM3 heme domain changes MRI contrast and optical absorption in a concentration-dependent manner

The wild-type BM3 enzyme is a soluble fatty acid hydroxylase comprising a 53 kDa heme domain fused to a 65 kDa reductase domain[21]. The heme domain (BM3h) contains a single paramagnetic iron(III) atom (mixed spin 1/2 and 5/2[22]), bound to a hemin prosthetic and axially coordinated by residue C399 on the protein. In the absence of substrate, the remaining iron coordination site is filled by a water molecule[23]. Interaction between exchanging water molecules at the axial site and the heme iron atom promotes T_1 relaxation in aqueous solutions[24]. To determine the extent of this effect, we used a spin echo MRI pulse sequence to measure the proton relaxation rate as a function of protein concentration in phosphate buffered saline solution (PBS); the slope of this relationship (T_1 relaxivity, or r_1) provides a standard measure of the strength of a contrast agent. For BM3h in the absence of ligands, an r_1 value of 1.23 ± 0.07 $mM^{-1}s^{-1}$ was obtained. Addition of a saturating quantity of natural BM3 substrate, arachidonic acid (AA, 400 uM concentration), resulted in an r_1 of 0.42 ± 0.05 $mM^{-1}s^{-1}$ (Fig. 1a). This ligand-dependent change in relaxivity enabled quantitative sensing of AA using MRI (Fig. 1b), and suggests that BM3h could serve as a platform for molecular sensor engineering.

We next tested whether DA or related compounds could serve as unnatural ligands to BM3h, when applied at high enough concentrations. As measured by MRI, addition of 1 mM DA to BM3h in fact induced a drop in r_1, to 0.76 ± 0.03 $mM^{-1}s^{-1}$. (Fig 1a). Binding of AA is known to induce a change (blue shift) in BM3h's optical absorbance spectrum, because of perturbation of the electronic environment of the heme chromophore[101]. To determine whether low affinity binding by DA also influences optical absorption by BM3h we measured spectra in the presence and absence of 1 mM DA. The interaction produced a significant red shift of λ_{max}, from 419 to 422 nm (Fig. 1c). Red shifting of iron porphyrin absorption spectra has been taken to indicate direct coordination to the heme iron[101], and suggested in this case that 1 mM DA directly replaces water as an axial metal ligand in BM3h; this model is consistent with the established propensity of catechols to bind to iron and other transition metals. These considerations strongly suggested that MRI and optical readouts of ligand binding to BM3h both report interactions with the heme site, and that binding measurements obtained with either modality are comparable indicators of these interactions. We monitored the difference between absorption at two wavelengths, as a function of ligand concentration, to determine binding isotherms for AA and DA (Fig 1 d,e). For BM3h, the apparent K_d for AA was 6.8 ± 0.5 µM; for DA the K_d was 990 ± 110 µM. Goals for the production of BM3h-based MRI sensors thus included decreasing the affinity for AA, increasing the DA affinity by at least two orders of magnitude, and maintaining or enhancing the relaxivity changes observed upon ligand binding.

Screen-based isolation of BM3h mutants with enhanced DA affinity

To create an MRI sensor for DA using directed evolution, we needed to develop a customized screening methodology (Fig. 2a). Results presented above suggested that either MRI-based or optical assays could be used conveniently to distinguish BM3h mutants with differing ligand affinities. We chose to use an absorbance assay for our screen, primarily because low protein concentrations (~1 µM) could be used for affinity measurements. Input to each round of screening consisted of a library of BM3h mutants generated by error-prone PCR from the wild-type gene or a previously selected mutant. DNA libraries of ~10^{15} variants each were transformed into *E. coli* and plated. Approximately 900 randomly selected clones were grown and induced in microtiter plate format, then prepared into cleared lysates for optical assaying in a plate reader. Aliquots of DA and AA were then added to lysates while optical spectra were recorded. High-throughput fluid handling was achieved using an automated pipetting station. The optical data was analyzed to determine K_d values for DA and AA. An average of 79% of assayed mutants exhibited sufficient protein levels (absorbance signal > 30% of parent) and had clean enough titration curves ($r^2 > 0.8$) for K_d estimation. Mutant affinities appeared to be distributed randomly about the dissociation constant measured for the corresponding parent protein; however individual clones with significant desired affinity changes could be identified in each round (Fig. 2b). From each screen, 8-10 mutants were chosen based on their estimated K_d's, purified in bulk, re-titrated to obtain more accurate estimates of DA and AA affinities, and examined by MRI to ensure that robust ligand-induced changes in r_1 could be detected. Based on these assays, the mutant showing the best combination of improved DA affinity, decreased affinity for AA, and relaxivity changes was chosen to be a parent for the next round of directed evolution.

By carrying out the screening strategy over multiple rounds, we found a steady trend in the distribution of K_d values towards greater affinity for DA and lower affinity for AA (Fig. 2b-d). Little change in binding cooperativity was observed, and changes in partial saturation generally occurred over a factor of 100 in DA concentration. Five rounds of evolution yielded a BM3h variant with eight mutations (Fig. 2e), four near the ligand-binding pocket and four at distal surfaces of the protein. One residue (I263) was first mutated to threonine (third round), then to alanine (fourth round). The clones selected from rounds one, three and five had two new mutations each. We did not perform site-directed mutagenesis to determine the relative contribution of each mutation to the observed changes in affinity. The mutation I366V was introduced by site-directed mutagenesis after the fourth round to enhance thermostability[102, 103] (see supplementary materials).

Selected sensor proteins show strong, preferential MRI response to DA

The mutant proteins selected after the fourth and fifth round of evolution, denoted BM3h-8C8 and BM3h-B7, had dissociation constants of 8.9 ± 0.7 μM and 3.3 ± 0.1 μM, respectively, for DA, and 750 ± 140 μM and 660 ± 80 μM for AA. The T_1 relaxivity of

BM3h-8C8 was 1.1 ± 0.1 $mM^{-1}s^{-1}$ in the absence of ligand, and 0.17 ± 0.03 $mM^{-1}s^{-1}$ in the presence of 400 μM DA (Fig. 3a). For BM3h-B7, the corresponding r_1 values were 0.96 ± 0.13 $mM^{-1}s^{-1}$ and 0.14 ± 0.04 $mM^{-1}s^{-1}$. Both sensor variants exhibited a DA concentration-dependent decrease in T_1-weighted MRI signal (up to 13% with 28.5 μM protein) that could be fitted by binding isotherms with estimated K_d values of 4.9 ± 2.7 μM for BM3h-8C8 and 2.7 ± 2.9 μM for BM3h-B7 (Fig. 3b,c).

The reporting specificities of BM3h-8C8 and BM3h-B7 for DA were investigated by measuring MRI signal changes that resulted from incubating 28.5 μM of each protein with 30 μM of DA or one of eight other neuroactive molecules: norephinephrine (NE), 3,4-dihydroxy-L-phenylalanine (DOPA), serotonin (5HT), glutamic acid (Glu), glycine (Gly), γ-aminobutyric acid (GABA), acetylcholine (ACh), and AA (Fig. 3d). Of these potential ligands, only DA, NE and 5HT elicited significant changes in the T_1 relaxation rate ($1/T_1$). For BM3h-8C8, the $1/T_1$ reductions produced by NE and 5HT were 0.0076 ± 0.0023 s^{-1} and 0.0041 ± 0.0020 s^{-1}, respectively, compared to 0.0182 ± 0.0006 s^{-1} for DA; for BM3h-B7, NE and 5HT induced $1/T_1$ decreases of 0.0112 ± 0.0024 s^{-1} and 0.0171 ± 0.0005 s^{-1}, respectively, compared to 0.0208 ± 0.0002 s^{-1} for DA. The affinities of BM3h-based DA sensors for these competitors were measured spectroscopically (Fig. 3d, inset). For BM3h-8C8, measured K_d's were 44 ± 3 μM and 80 ± 8 μM for NE and 5HT, respectively, and for BM3h-B7 the K_d values were 18.6 ± 0.4 μM and 11.8 ± 0.1 μM, respectively. While both BM3h-8C8 and BM3h-B7 show significantly higher affinity for DA over NE (5-fold and 6-fold, respectively) and over 5HT (9-fold and 4-fold, respectively), the BM3h-8C8 variant is more specific for sensing DA at concentrations above 10 μM. In settings where DA is known to be the dominant neurotransmitter, BM3h-B7 may provide greater overall sensitivity

The stability and reversibility of DA sensing by BM3h variants were examined. DA-induced changes in the BM3h-B7 and BM3h-8C8 absorbance spectra were steady over a period of more than 2 hours, in the presence of DA concentrations up to 800 μM (Supplementary Fig. 1). Reversibility of DA binding to the sensors was confirmed by showing that their absorbance spectra reverted to their ligand-free state after DA was removed by size-cutoff filtration (Supplementary Fig. 2). Stored in PBS at 4° C, the proteins appeared stable over a period of several days.

BM3h-based sensors report DA release from PC12 cells *in vitro*

We next asked whether BM3h mutants identified by directed evolution could sense DA release from living cells. The pheochromocytoma cell line PC12 provides a popular model of DA metabolism, transport, and signaling[104]; PC12 cells have been shown to release vesicular DA when depolarized by extracellular potassium ions[105]. We therefore adapted an established experimental paradigm to test the ability of our sensors to detect stimulus-evoked DA discharge from PC12 cells (Fig. 4a). Cells were loaded with DA by preincubation over a one hour period. After pelleting and washing, cells were resuspended in a physiological buffer containing 32 μM BM3h-B7 and either 5.6 or 59.6 mM K^+ (the low K^+ condition was osmotically balanced with Na^+). T_1-weighted MRI images (spin echo TE/TR = 10/477 ms) obtained with BM3h-B7 showed a 4.0 ± 0.5% reduction in signal intensity in the supernatant of K^+-stimulated cells, compared with cells for which isotonic Na^+ was used as a nondepolarizing control stimulus (Fig. 4b).

This corresponded to a 54 ± 4% decrease in sensor r_1 (Fig. 4c). Given the DA dissociation constant of BM3h-B7 and its relaxivities under ligand-free and DA-saturated conditions, and assuming negligible dilution of the sensor after mixing with cells, we estimated supernatant DA concentrations of 50.7-63.7 μM for stimulated cells and 21.0-23.2 μM for controls. These estimates are in reasonable agreement with an independent quantification of DA release made using an enzyme-linked immunosorbent assay (ELISA), which yielded concentrations of 54 ± 9 μM and 13 ± 2 μM for stimulated and control cells, respectively (Fig 4d). BM3h-8C8 could also be used to image DA release from PC12 cells. Under experimental conditions similar to above, BM3h-8C8 exhibited a 37 ± 2% reduction in r_1 in the supernatant of K^+-stimulated cells relative to Na^+ controls (Supplementary Fig 3). These results demonstrated that BM3h-based sensors are capable of reporting release of DA in a biological context using MRI.

BM3h-8C8 enables dynamical MRI imaging of DA transport *in vivo*

To demonstrate sensing *in vivo*, we used BM3h-8C8 to image the transport of injected DA in the striatum of anesthetized Lewis rats. We first confirmed that the interaction between DA and BM3h-8C8 produces the expected MRI contrast change in the *in vivo* environment. The sensor, alone or mixed with DA, was infused stereotactically into rat striatum over 20 minutes (Fig. 5a). Images were obtained before, during and after infusion using a T1-weighted FSE pulse sequence with a spatial resolution of 0.3 mm x 0.3 mm x 1 mm and a temporal resolution of 8s. The 15 voxels with the greatest change in signal at the end of the infusion period were selected for further analysis. As expected, infusing BM3h-8C8 produced a gradual increase in T1-

weighted signal (to ~ 25% at the end of the infusion period), the magnitude of which was reduced to ~10 % by co-infusing DA (Fig 5b, c). Infusing wild-type BM3h also produced a signal change, but this change was unaffected by the presence of DA (Fig 5d).

Since the striatum is heavily innervated by dopaminergic axons, some amount of reuptake would be expected for DA infused into this brain region. We hypothesized that reuptake of DA could contribute to higher T1-weighted signal by removing some DA that would otherwise be bound to BM3h-8C8. In preliminary experiments to test this hypothesis, we endeavored to block DA reuptake using cocaine. When cocaine was co-infused into the striatum together with BM3h-8C8 and DA, both the maximal signal change and the rate of signal increase during infusion were significantly reduced (Fig 5e), suggesting that more DA remains in the selected voxels, although additional experiments are needed to confirm that this is the case. These results demonstrate that BM3h-8C8 retains its DA-dependent contrast properties *in vivo* and could potentially serve as an effective sensor of DA transport in the living brain.

DISCUSSION

Our results demonstrate for the first time that a powerful protein engineering method can be applied successfully to the construction of a dynamic MRI sensor capable of imaging an important signaling molecule *in vivo*. Instrumental to the success of our approach was the choice of a protein, cytochrome P450 BM3h, which produced ligand-induced MRI contrast changes in its wild-type form and had tunable ligand selectivity, making it a suitable platform for sensor development. To apply directed evolution to the creation of a DA sensor, we designed an optical screen for mutant proteins with enhanced DA sensitivity. Although an MRI-based screen might have been more direct, the optical titration curves we in fact examined could be measured more conveniently, and appeared to be directly correlated with relaxivity-determining structural changes near the protein's heme site. This methodology can be employed to develop sensors for a variety of small molecules, with a wide structural range implied by our ability to tune sensing between the structurally dissimilar molecules AA and DA.

In vitro experiments confirmed that the high-affinity DA sensors we produced, BM3h-B7 and BM3h-8C8, are able to detect and quantify depolarization-triggered DA release from cultured cells. Given the $1/T_1$ changes we observed in this context (~0.01 s^{-1}), it is reasonable to expect signal changes of ~1-2% to be observed if the sensors are applied at similar concentrations in the extracellular space of the intact brain, and if DA concentrations varied in the range from 0-40 μM DA (as in brain stimulation reward paradigms, *e.g.* [43, 44]).

I*n vivo*, we demonstrated that BM3h-8C8 could be used to observe signal changes resulting from co-infusion of DA in the rat striatum and potentially from modulation of its reuptake with cocaine. These observations was aided by the high spatial (300 μm) and temporal (8 sec) resolution of MRI, highlighting one of the major advantages of sensors designed for this imaging modality.

Detection by MRI would be easier if the sensors had higher r_1. At field strengths comparable to the 4.7 T we used, relaxivity changes of roughly 1.8 to 2.5 $mM^{-1}s^{-1}$ have been reported for Gd^{3+}-based synthetic sensors[14, 106], which have higher electron spin (S = 7/2) than BM3h (mixed S = 1/2, 5/2). In principle, improved BM3h sensors for DA or other ligands could be engineered to produce greater relaxivity changes, most likely by increasing the percentage of high spin iron in the heme site.

In future studies, BM3h-based sensors for DA may be applied by direct intracranial infusion as was done here, or intravenously in conjunction with blood-brain barrier permeabilization techniques [107]. Subsequent monitoring of DA release and transport will be valuable in studies of reward, addiction, Parkinson's disease, and a variety of brain phenomena involving dopaminergic signaling; related sensors could be applied in similar ways to study additional neurotransmitter systems or physiological phenomena. Because BM3h-based MRI sensors are proteins, they may also be targeted genetically to specific brain regions or cell types[108], where they would report local analyte concentrations, provided that high enough sensor expression levels (> 10 μM) could be attained. A longer-term motivation behind the development of novel MRI sensors is the potential for human diagnostic use, either as exogenous agents or components of genetically-engineered transplants such as stem cells. The relative ease of production and versatility of metalloprotein MRI sensors, like the DA probes introduced here, suggests that this new class of reagents may find utility in a broad range of biological and medical applications.

METHODS

Library construction

BM3h mutant libraries were constructed in accordance with a previously published protocol[25]. The starting parent for evolution was the wild type heme domain of BM3 with a C-terminal hexahistidine tag, housed in the pCWori vector[109]. Mutant libraries were constructed through error-prone PCR using the primers GAAACAGGATCCATCGATGCTTAGGAGGTCAT (forward) and GCTCATGTTTGACAGCTTATCATCG (reverse) and Taq polymerase (AmpliTaq, Applied Biosystems, Foster City, CA) with 25 μM $MnCl_2$, producing approximately 1-2 mutations per gene. Between the fourth and fifth rounds of evolution, the mutation I366V was introduced into 8C8 via overlap extension PCR to improve protein thermostability[103] (see Supplementary Info).

Protein expression and high-throughput screening

Mutant colonies were picked into deep-well 96-well plates containing 0.4 mL Luria Broth (LB) medium and grown overnight. On each plate, the parent clone and up to three previous parents were included in triplicate. 0.1 mL of each culture was transferred to new plates containing 1.2 mL fresh Terrific Broth (TB) medium per well, supplemented with 100 μg/mL Ampicillin, 0.2 mM IPTG and 0.5 mM δ-aminolevulinic acid (ALA). Remaining LB cultures were stored with glycerol at -80 °C. Following 20-30 hours of protein expression at 30 °C, cultures were pelleted and lysed in 0.65 mL PBS containing 0.75 mg/ml hen egg lysozyme (Sigma Aldrich, St. Louis, MO) and 5 μg/mL DNase I (Sigma Aldrich). Absorbance spectra of 200 μL of cleared lysate from each well were recorded in a multiwell plate reader (Spectramax Plus, Molecular Devices, Sunnyvale, CA) before and after addition of successively more concentrated DA or AA. The resulting absorbance spectra were analyzed in Matlab (Mathworks, Natick, MA), using a custom routine that calculated the absorbance difference spectra for each acquisition relative to ligand-free lysate, computed the difference between maximum and minimum of each difference spectrum, plotted each value as a function of ligand concentration, and for each well fitted a non-ligand depleting bimolecular association function to estimate the corresponding K_d. Mutant K_d values were compared to those of the parents within each plate, and 8-10 mutants showing the greatest decrease in K_d for DA and/or the greatest increase in K_d for AA were chosen for bulk expression and analysis.

Bulk expression and titrations

Frozen LB cultures of selected mutants were inoculated into 30 mL TB medium containing 100 μg/mL Ampicillin, induced at log phase with 0.6 mM IPTG, supplemented with 0.5 mM ALA and 50 μg/ml thiamine, and shaken for an additional 20-25 hours to express protein. Pelleted cells were lysed with BugBuster and Lysonase (EMD Chemicals, San Diego, CA) and BM3h mutants purified over Ni-NTA agarose (Qiagen, Valencia, CA). Buffer was exchanged to PBS over PD-10 desalting columns (GE Healthcare, Piscataway, NJ). Protein concentration was measured by CO assay[110]. Titrations with DA, AA, 5HT, NE, DOPA, Ach, Glu, Gly, and GABA (Sigma Aldrich) were performed on samples of purified protein and analyzed using Matlab as described above.

MRI

Samples (60-100 μL) were arrayed into microtiter plates and placed in a 40-cm-bore Bruker (Billerica, MA) Avance 4.7 T MRI scanner, equipped with a 10 cm inner diameter birdcage resonator radiofrequency coil and 26 G/cm triple axis gradients. Unused wells of the microtiter plates were filled with phosphate buffered saline, and imaging was performed on a 2-mm slice through the sample. A T_1-weighted spin echo pulse sequence was used; echo time (*TE*) was 10 ms, and repetition times (*TR*) ranged from 77 ms to 5 s. Data matrices of 512 × 128 points were acquired and zero-filled to 1024 x 512 points, where the second dimension corresponds to the phase encoding direction. Images were reconstructed and analyzed using custom routines running in Matlab. Relaxation rates and relaxivities reported here were calculated by exponential fitting to the image data. Contrast was adjusted to produce MRI images presented in the figures.

DA release from PC12 cells

PC12 cells were grown in suspension in F-12K medium supplemented with 15% horse serum and 2.5% fetal bovine serum (ATCC, Manassas, VA). In preparation for DA release experiments, 50 mL cell cultures were incubated for one hour in medium supplemented with 1 mM DA and 1 mM ascorbic acid, pelleted and washed twice with Locke's buffer (154 mM NaCl, 5.6 mM KCl, 3.6 mM $NaHCO_3$, 2.3 mM $CaCl_2$, 5.6 mM D-glucose, and 5 mM HEPES, pH 7.4). To Locke's buffer missing 54 mM NaCl and containing or not containing the sensor, a 1:50 dilution of 2.7 M KCl (stimulus) or NaCl (control) was added. Washed PC12 cell pellets were resuspended in 200 μL of either K^+- or Na^+-supplemented buffer, with or without sensor. After 30-60 minutes incubation at room temperature, cells were pelleted and the supernatant was imaged in an MRI scanner as described above. DA release was estimated by calculating sensor saturation level from observed r_1, then solving the quadratic equation describing bimolecular equilibrium binding with a known K_d, and assuming 32μM of sensor, for ligand concentration. Independent measurements of DA release were made using the Dopamine EIA Kit (LDN, Nordhorn, Germany).

MRI imaging of DA transport *in vivo*

Lewis rats (350-500 g) were anesthetized with 1.5% - 2% isoflurane, placed on a heat blanket and monitored with pulse oxymetry throughout the subsequent surgery.

Plastic guide cannulae (6 mm length, PlasticsOne) were stereotactically inserted bilaterally into the striatum using stereotactic coordinates (0.7 mm rostral and 3 mm lateral to bregma, 5 mm below dura) and secured in place with dental cement. A T-shaped headpost (Ultem 1000) was subsequently cemented on to the skull rostrally to the guide cannulae. Plastic tubing filled with silicon oil was connected to an MRI-compatible dual channel syringe pump (PhD 2000, Harvard Apparatus). The Silicon oil was retracted to generate a small air cushion of about 1 μl at the tips before connecting the internal cannulae (6.1 mm length, PlasticsOne) to the tubing. Subsequently, a volume of 20 μl of PBS solution containing the MRI sensor (500 μM 8C8 variant (or wt) of BM3h +/- 500 μM of Dopamine (Sigma)) was aspirated through the internal cannulae. The solution for the cocaine reuptake inhibition experiments contained 500 μM 8C8 variant, 500 μM and +/-

1 μmole cocaine (Sigma). The pump was then slowly run in infusion mode for a short time to ensure that the MRI sensor solution would reach the tip of the cannulae without

any dead space. Internal cannulae were subsequently inserted into the guide cannulae and secured with dental cement. A MRI surface coil (Insight Neuroimaging), modified to have an appropriate cutout to accommodate the cannulae and the headpost, was placed over the rat's head. The head was then moved into a plastic headgear, the rat's teeth positioned over a bite bar and the headpost screwed into the headgear with plastic screws. Subsequently, the rat was moved into a body holder, which was wrapped in a heat blanket before being inserted into a birdcage body coil (Insight Neuroimaging). The dual coil imaging setup was then moved in to the bore of a Bruker 4.7 Tesla magnet (40 cm horizontal bore) interfaced to an AVANCE console (Bruker Instruments) and equipped with a 12 cm ID triple axis gradient set (26 G/cm maximum). The scanner was controlled using Paravision software running on a Linux workstation. A continuous series of MRI scans were obtained using a T1-weighted FSE pulse sequence (0.3 mm x 0.3 mm x 1 mm resolution, 8 s per image) before, during and after an injection period of 20 minutes (0.0005 mL/min). The rat was monitored by pulse oxymetry throughout the imaging experiment. Analysis of imaging data was performed with Matlab v.7 (Mathworks) running in-house processing routines.

ACKNOWLEDGEMENTS

The authors wish to thank Neel Shah for assistance with animal experiments. MGS wishes to acknowledge the Fannie and John Hertz Foundation and the Paul and Daisy Soros Fellowship for generous support. This work was funded in part by a Dana Foundation Brain and Immuno-Imaging grant to AJ, NIH grant number R01-GM068664–01 to FHA, and NIH grant number R01-DE013023-08 to RL.

FIGURE LEGENDS

Figure 1. Ligand binding to the BM3 heme domain changes MRI contrast and optical absorption in a concentration-dependent manner. **(a)** T_1 relaxivity (r_1) of BM3h in PBS solution, and in the presence of 400 μM AA or 1 mM DA; inset shows T_1-weighted spin echo MRI image intensity (*TE*/*TR* = 10/477 ms) of microtiter plate wells containing 240 μM BM3h in PBS alone (left), or in the presence of 400 μM AA (middle) or 1 mM DA (right). **(b)** T_1 relaxation rates ($1/T_1$) measured from solutions of 28.5 μM BM3h incubated with 0-250 μM AA. **(c)** Optical absorbance spectra of 1 μM BM3h measured alone (blue), and following addition of 400 μM AA (gray) or 1 mM DA (orange). **(d)** Difference spectra showing the change in BM3h absorbance as a function of wavelength upon addition of 400 μM AA (gray) or 1 mM DA (orange). **(e)** Normalized titration curves showing binding of BM3h to AA (gray) or DA (orange). The optical signals used for titration analysis were formed by subtracting the minimum from the maximum of difference spectra [arrowheads in (d)] under each set of conditions. Error bars were smaller than the symbols.

Figure 2. Screen-based isolation of BM3h mutants with enhanced DA affinity. **(a)** Schematic of the directed evolution approach, including (left to right) mutant DNA library generation, transformation into *E. coli* and growth in multiwell plate format, spectroscopic analysis of each mutant's ligand binding affinities, and detailed MRI and optical characterization of selected mutant proteins. **(b)** Histograms of mutant DA

dissociation constants determined during each round of directed evolution, by relating each mutant protein's relative DA affinity (measured in plate format) to the K_d of the parent protein (measured in bulk). K_d distributions for screening rounds one (blue), two (green), three (red), four (cyan), and five (purple) are labeled by numbers in circles. Color-coded arrowheads indicate the measured K_d's of parent proteins used to create the library of mutants at each round; the yellow arrowhead indicates the K_d of the mutant protein selected after round five of screening. **(c)** Dissociation constants for DA (orange) and AA (gray) measured from wild type BM3h and mutant BM3h variants isolated by each round of screening; progressive improvements in DA affinity and attenuation of AA affinity are evident. Colored arrowheads indicate the correspondence with data in panel (a). **(d)** Titration analysis of DA binding to WT BM3h and proteins selected after each round of directed evolution [color coding as in (b)]. Mutant proteins identified by rounds four (8C8) and five (B7) were considered to be end products of the screening procedure. **(e)** X-ray crystal structure[111] of WT BM3h (gray; heme group shown in orange) bound to palmitoleic acid (black), indicating the location of amino acid substitutions accumulated during directed evolution of enhanced DA binding affinity. Each mutation's location is identified by a blue sphere and a label color-coded by the parent protein in which the substitution was first identified [see caption to (b)]. The previously characterized I366V mutation (asterisk) was incorporated between screening rounds four and five, to improve the thermostability of the engineered proteins.

Figure 3. Selected sensor proteins produce strong and specific MRI signal changes in response to DA. **(a)** Relaxivity values measured from BM3h-B7 (yellow bars) and

BM3h-8C8 (purple bars) in PBS alone, or in the presence of 400 μM DA. The inset shows T_1-weighted MRI signal (*TE/TR* = 10/477 ms) obtained from 195 μM BM3h-B7 or BM3h-8C8, each incubated in microtiter plate wells with or without 400 μM DA (wells ordered left to right as in the bar graph). **(b)** A normalized MRI image showing signal amplitudes measured from wells containing 28.5 μM WT BM3h, BM3h-8C8, and BM3h-B7, each incubated with increasing DA concentrations (0-63 μM, left to right). The image was formed by dividing signal from a T_1-weighted scan (I_{T_1}; *TE/TR* = 10/477 ms) by signal from a proton-weighted image ($I_{^1\mathrm{H}}$; *TE/TR* = 10/5000 ms), to correct for intensity variation due to radiofrequency heterogeneity in the scanner. **(c)** Relaxation rates ($1/T_1$ values) measured from solutions of 28.5 μM WT (blue), BM3h-B7 (yellow), and BM3h-8C8 (purple), as a function of total DA concentration. Curves were fitted using a ligand-depleting bimolecular association model. **(d)** Changes in $1/T_1$ relative to ligand-free protein for 28.5 μM BM3h-B7 (yellow) and BM3h-8C8 (purple) incubated with 30 μM DA, 5HT, NE, DOPA, AA, ACh, GABA, Glu, or Gly; inset: spectroscopically determined affinities ($K_a = 1/K_d$) of BM3h-B7 and BM3h-8C8 for DA, 5HT, and NE.

Figure 4. BM3h-based sensors report DA release from PC12 cells. **(a)** In our experimental paradigm, PC12 cells depolarized by addition of 54 mM K^+, but not 54 mM Na^+, were stimulated to release DA into supernatants containing a BM3h-based sensor. **(b)** T_1-weighted spin echo MRI signal amplitudes (*TE/TR* = 10/477 ms) measured from the supernatants of PC12 cells incubated with 32 μM BM3h-B7 in the presence of K^+ (stimulus) or Na^+ (control); inset: MRI image of microtiter wells under corresponding

conditions. **(c)** Relaxation rates measured from the samples in (b), minus the relaxation rate of buffer not containing BM3h-based sensors. Given the approximate concentration of BM3h variants in these samples, the $\Delta(1/T_1)$ values correspond to apparent relaxivities of 0.23 and 0.50 $mM^{-1}s^{-1}$ in K^+ and Na^+ incubation conditions, respectively. **(d)** Data from panel (c) were used to estimate the concentrations of DA present in samples treated with K^+ and Na^+ (gray bars). Independent measurement of [DA] under equivalent conditions was performed using an ELISA assay (white bars).

Figure 5. BM3h-8C8 enables dynamical MRI imaging of DA transport *in vivo.* **(a)** Diagram of setup for *in vivo* infusions. Bilateral injections into the striatum were made via surgically implanted cannulae. For ± DA experiments, BM3h-8C8 or wild type BM3h was injected on both sides, with DA co-injected on one side. For ± cocaine experiments, BM3h-8C8 and DA were co-injected on both sides, and cocaine was co-injected on one side. **(b)** T1-weighted MRI image of three adjacent coronal slices at the end of a BM3h-8C8 ± DA injection. Cannulae tracts are visible in the middle slice. A brightening of the image is observed immediately below the tip of the right cannula, where sensor was injected alone, but not below the tip of the left cannula, where DA was co-injected with sensor. **(c)** Timecourse of T1-weighted signal change during and after injection of BM3h-8C8 without (blue) and with (orange) DA. Gray shading indicates when the injection occurred. **(d)** Same as (c), but with wild type BM3h instead of BM3h-8C8. **(e)** Timecourse of signal during injection as in (c), but both with both sides receiving BM3h-8C8 and DA, without (orange) or with (green) the addition of 1 μmol cocaine.

Figure 1

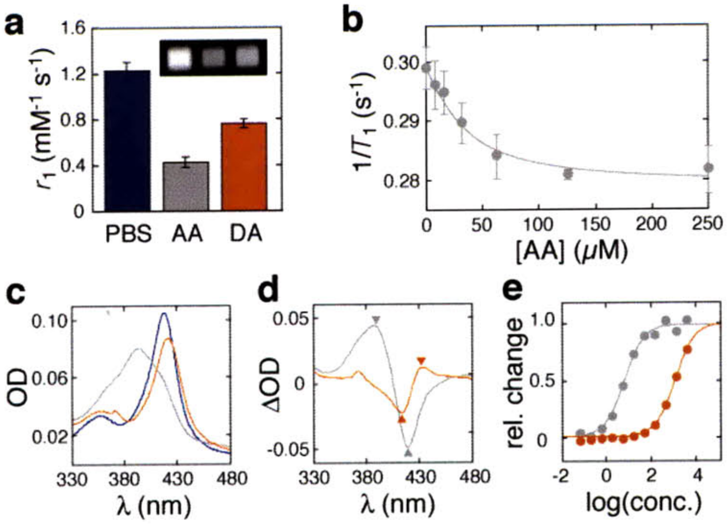
a
1.6
1.2
0.8
0.4
0
r_1 (mM^{-1} s^{-1})
PBS
AA
DA
b
0.30
0.29
0.28
1/T_1 (s^{-1})
0
50
100
150
200
250
[AA] (μM)
c
0.10
0.06
0.02
OD
330
380
430
480
λ (nm)
d
0.05
0
-0.05
ΔOD
330
380
430
480
λ (nm)
e
1.0
0.5
0
rel. change
-2
0
2
4
log(conc.)

Figure 2

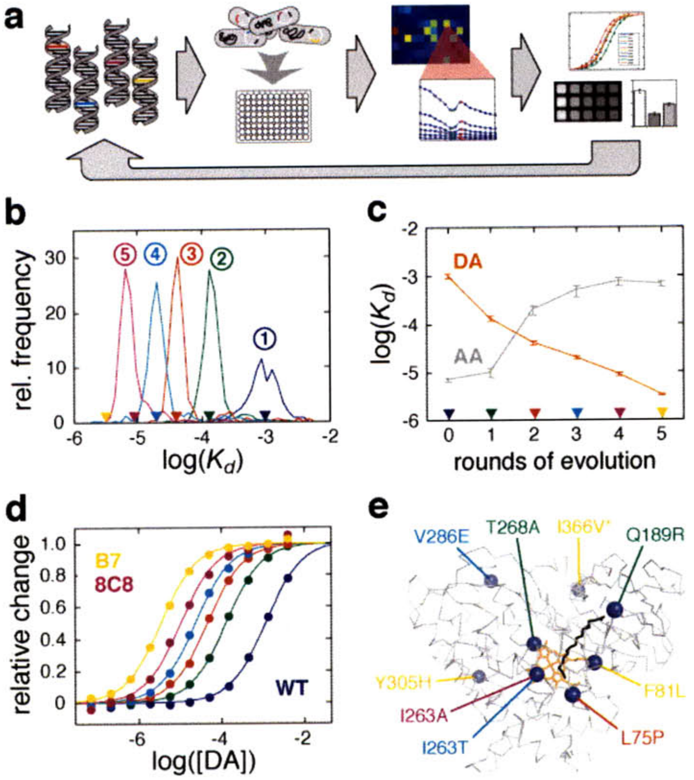
a
b
⑤ ④ ③ ② ①
rel. frequency
30
20
10
0
-6
-5
-4
-3
-2
log(Kd)
c
-2
-3
-4
-5
-6
DA
AA
log(Kd)
0
1
2
3
4
5
rounds of evolution
d
relative change
1.0
0.8
0.6
0.4
0.2
0
B7
8C8
WT
-6
-4
-2
log([DA])
e
V286E
T268A
I366V*
Q189R
Y305H
F81L
I263A
I263T
L75P

Figure 3

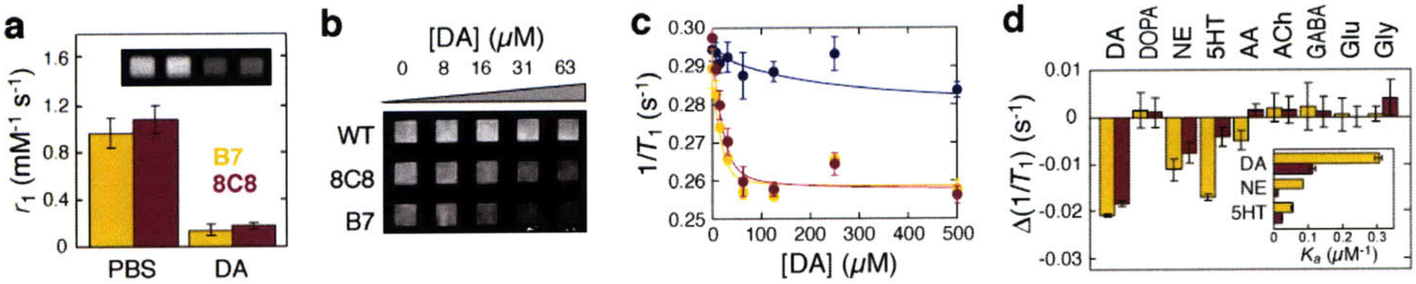
a
1.6
1.2
0.8
0.4
0
r_1 (mM^{-1} s^{-1})
B7
8C8
PBS
DA
b
[DA] (μM)
0
8
16
31
63
WT
8C8
B7
c
0.30
0.29
0.28
0.27
0.26
0.25
$1/T_1$ (s^{-1})
0
100
200
300
400
500
[DA] (μM)
d
DA
DOPA
NE
5HT
AA
ACh
GABA
Glu
Gly
0.01
0
-0.01
-0.02
-0.03
$\Delta(1/T_1)$ (s^{-1})
DA
NE
5HT
0
0.1
0.2
0.3
K_a (μM^{-1})

Figure 4

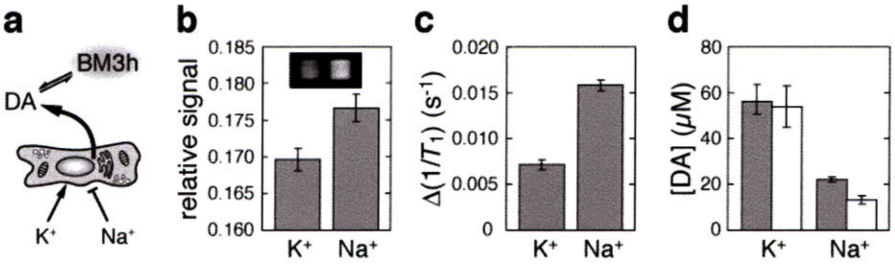
a
BM3h
DA
K⁺
Na⁺
b
relative signal
0.185
0.180
0.175
0.170
0.165
0.160
K⁺
Na⁺
c
Δ(1/T₁) (s⁻¹)
0.020
0.015
0.010
0.005
0
K⁺
Na⁺
d
[DA] (μM)
80
60
40
20
0
K⁺
Na⁺

Figure 5

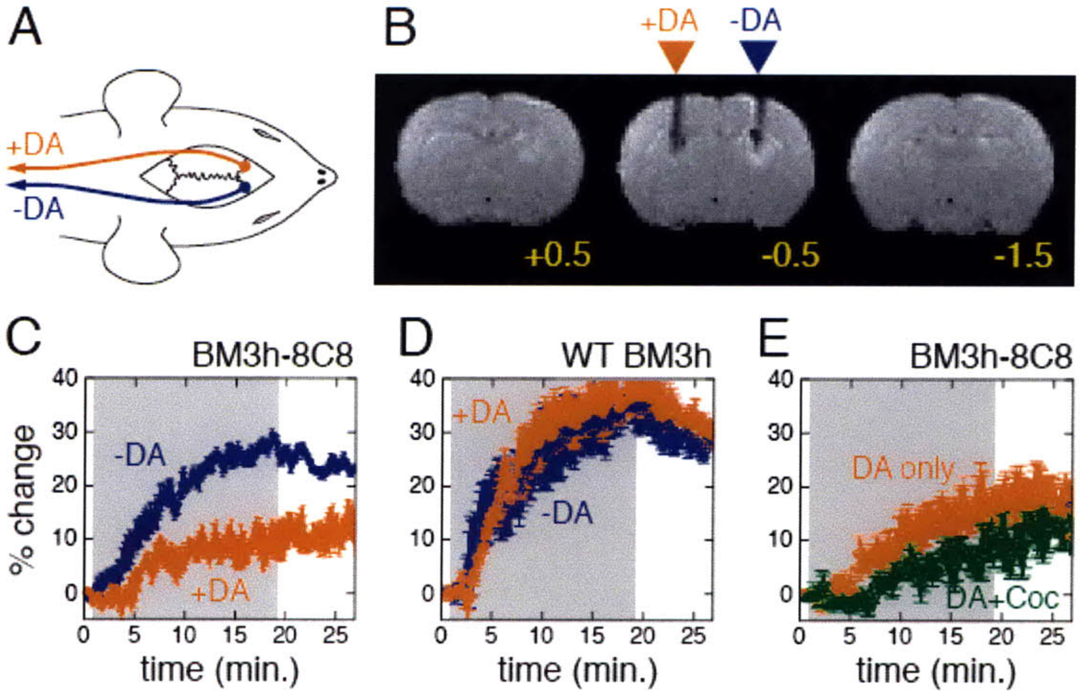
A
+DA
-DA
B
+DA
-DA
+0.5
-0.5
-1.5
C
BM3h-8C8
% change
-DA
+DA
time (min.)
D
WT BM3h
+DA
-DA
time (min.)
E
BM3h-8C8
DA only
DA+Coc
time (min.)
0
10
20
30
40
0
5
10
15
20
25

SUPPLEMENTARY MATERIAL

DA binding to BM3h-B7 and BM3h-8C8 is stable and reversible

The stability of DA binding to BM3h-B7 and BM3h-8C8 was tested by incubating each protein with various amounts of DA at room temperature and measuring the absorbance difference at 430 nm and 410 nm over two hours (Supplementary Fig. 1). During this time, a decline of less than 5% was observed when 1 μM sensor was incubated in the presence of excess DA (800 μM). Optical changes were greater when sensor was incubated with subsaturating concentrations of DA (up to 22% signal change for 1.3 μM DA incubated with BM3h-B7), consistent with the predicted effects of DA oxidation (known to take place under ambient conditions) on the partial saturation of the sensor. To test the reversibility of DA binding to BM3h-B7 and BM3h-8C8, we acquired absorbance spectra of the proteins alone and with 400 μM DA before and after filtering the solutions through a 30 kDa cutoff centrifugal filter. Successive steps of filtering and resuspension restored the original, ligand-free spectrum (Supplementary Fig. 2a,b).

Thermostabilization of BM3h-8C8

Mutations in the amino acid sequence of BM3h have been shown to reduce the protein's thermostability. This was observed during directed evolution of BM3h: the melting temperature (T_{m}, the midpoint temperature for thermal denaturation after 10 min) of WT BM3h was approximately 58 °C, while the T_m for BM3h-8C8 was approximately 48 °C. While this change did not significantly affect the protein's stability in physiologic buffer at room temperature, it did apparently reduce the yield of our bulk purification procedure. To improve thermostability of BM3h-8C8 before performing the fifth round of evolution, we introduced the mutation I366V, which has been shown previously to improve stability[102]. For BM3h-8C8 this improvement corresponded to a T_m increase by approximately 4 °C.

SUPPLEMENTARY FIGURE CAPTIONS

Supplementary Figure 1. Optical signatures of DA binding to BM3h-B7 **(a)** and BM3h-8C8 **(b)** are stable over two hours. Absorbance at 430 nm minus 410 nm collected over 2 hrs. for 1 μM sensor incubated in the presence of 0-800 μM DA (labels in color).

Supplementary Figure 2. DA binding to BM3h-B7 and BM3h-8C8 is reversible. **(a)** Absorbance spectra of 1 μM BM3h-B7 alone (blue) or incubated with 400 μM DA (green) before filtering (top), and after filtering twice (middle) or three times (bottom) through a 30 kDa cutoff filter. **(b)** Ratios of absorbance at 430 nm to 410 nm corresponding to the DA-free (white bars) and DA-incubated (gray bars) spectra in (a). Panels **(c)** and **(d)** display equivalent data for sensor variant BM3h-8C8.

Supplementary Figure 3. BM3h-8C8 reports DA release from PC12 cells. Plot and experimental conditions are analogous to Fig. 4c in the main text.

Supplementary Figure 1

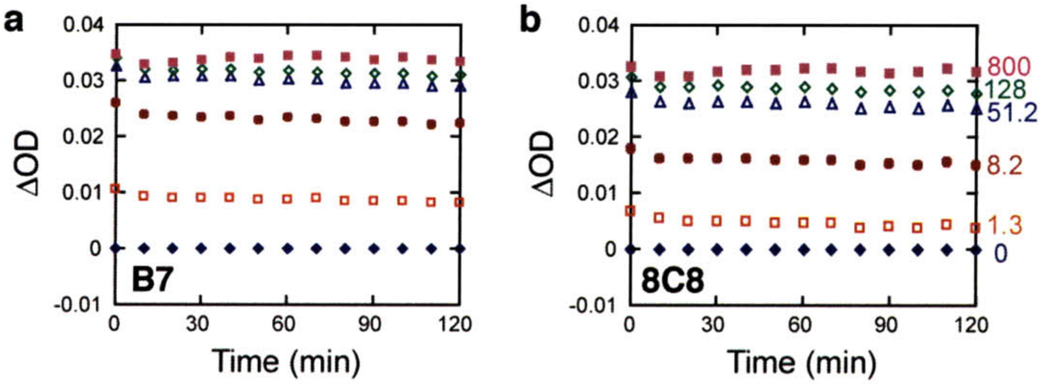

Supplementary Figure 2

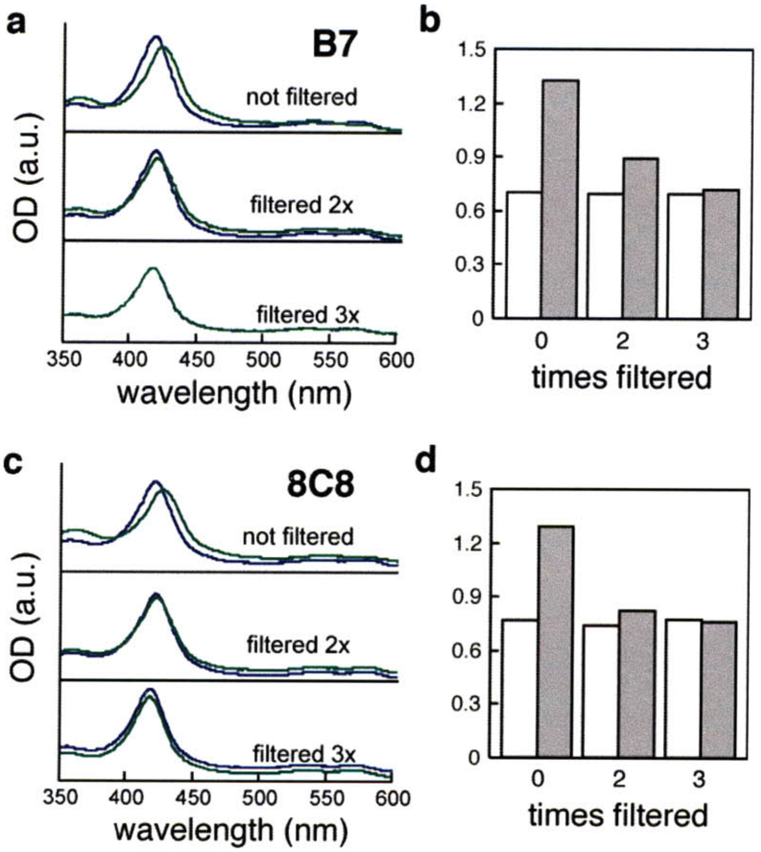

Supplementary Figure 3

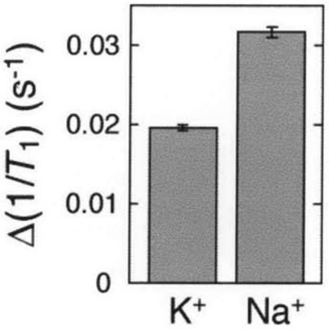

4. Protein nanoparticles engineered to sense protein kinase activity in MRI

ABSTRACT

Discoveries in neuroscience would be aided by the creation of tools for non-invasive molecular imaging of the brain, but the development and application of imaging agents that could serve this purpose remains a major challenge. Nanoscale superparamagnetic materials have been used to create molecular sensors for magnetic resonance imaging (MRI), but their synthetic nature makes them challenging to produce and limits their potential for future use *in vivo*. Here we describe for the first time a completely protein-based molecular sensor made of self-assembling multifunctional nanoparticles incorporating the iron storage protein ferritin. We created a sensor for cAMP-dependent protein kinase A (PKA), a key signaling molecule involved in memory processes, by generating fusions of ferritin with domains of CREB and CBP, and co-expressing them in mammalian cells with wild type and epitope-tagged ferritin subunits. Intact self-assembled nanoparticles were easily purified and loaded with iron. Incubation with PKA induced aggregation of the sensor nanoparticles, leading to real-time T2 contrast enhancement in MRI. Our approach enables future work towards genetically engineered molecular sensors for a variety of signaling processes, with potential applications in basic research and clinical diagnostics.

INTRODUCTION

Magnetic resonance imaging (MRI) has been a powerful tool in biological research, offering non-invasive access to anatomy and activity at high spatial and temporal resolution[7]. However, the range of biological phenomena accessible to measurement by MRI is limited due to a lack of molecular sensors that can respond dynamically to specific molecular signaling events. Earlier efforts to create MRI sensors have incorporated traditional MRI contrast moieties, such as gadolinium chelates or iron oxide nanoparticles, into complex organic structures or supramolecular assemblies [99, 100], resulting in sensors that are difficult to engineer, synthesize and apply *in vivo*.

MRI sensors based on proteins could resolve some of these difficulties. They could be developed using well-established protein engineering methods. They could be synthesized easily in cultured cells. And they could be applied in vivo by direct delivery or in-situ synthesis in cells targeted with corresponding genetic constructs.

The iron storage protein ferritin (Ft) represents a potential platform for developing protein-based MRI sensors. Ft comprises a 12nm protein shell and an 8nm antiferromagnetic iron oxide core containing up to 4,000 iron atoms[27]. Ft induces T2 relaxation in MRI and has been studied as an endogenous source of anatomical contrast and an exogenous marker of gene expression[28-30]. Aggregation of Ft after proteolysis[31] or chemical cross-linking[32] has been shown to enhance its T2 contrast, suggesting that Ft-based sensors could be made analogously to those previously created using synthetic iron oxide nanoparticles[15, 33, 34]. In these designs, nanoparticle surfaces were functionalized with moieties whose binding to each other or to other molecules drives the formation of aggregates, altering T2 contrast. Sensor performance depends on nanoparticles' surface properties, including the number of functional groups per particle and propensity for non-specific agglomeration. Ft nanoparticles comprise 24 heavy chain (HF) and light chain (LF) subunits which self-assemble into symmetrical nanoparticles at ratios proportional to their relative expression levels[35]. The N-termini of LF and HF are exposed at the nanoparticle surface, and can thus serve as sites for genetic fusion of surface functional groups[36]. A combination of fusion constructs and wild-type subunits could hypothetically be co-expressed at particular ratios to achieve desired surface properties and sensor performance. Ft's aggregation-dependent MRI contrast, its amenability to surface-functional fusions, and it ability to self-assemble from independent subunits in a stoichiometrically-controlled fashion make it a potential platform for protein-based sensor development.

Cyclic AMP-dependent protein kinase A (PKA) plays a critical role in memory formation and is an active target of pharmaceutical development[46]. It is thus an important target for molecular imaging. A key substrate of PKA is the transcription factor CREB[47]. When the residue Ser133 of the kinase inducible domain (KID) of CREB is phosphorylated by PKA, CREB binds to the KIX domain of the activator protein CBP[48, 49], turning on transcription of CREB-dependent genes[50]. Phosphorylation-dependent binding of KID and KIX has been studied extensively, and fluorescent sensors of PKA activity have been made by fusing these domains to variants of green fluorescent protein[51] or β-lactamase[52]. No MRI or other non-invasive sensor of PKA activity has been reported.

RESULTS AND DISCUSSION

We made a protein-based MRI sensor of PKA activity by producing Ft nanoparticles that incorporated KID or KIX functional groups on their surface (Fig 1a). Fusions of KID, KIX and the affinity tag 3xFLAG were made at the N-terminus of LF (KID-LF, KIX-LF and FLAG-LF, respectively). 3xFLAG was selected because of its high negative charge at neutral pH, the presence of which we thought would help reduce non-specific aggregation between Ft nanoparticles. The linker sequence GTSSEFM, inserted between each functional group and the N-terminus of LF, was found to produce well-expressing fusion constructs. Plasmids encoding FLAG-LF, wild-type LF, HF, and either KID-LF or KIX-LF were co-transfected into HEK-293 cells at pre-determined ratios. After four days of expression, cells were lysed and Ft nanoparticles were purified over an anti-FLAG resin. The nanoparticles were iron-loaded by incubation of lysates with an excess of ferrous ammonium sulfate. Self-assembly of different co-transfected subunits was confirmed by the presence of corresponding bands on coomassie-stained gels after FLAG purification (Fig. 1b). The relative functional group composition of the nanoparticles could be controlled by varying the transfection ratios of recombinant Ft genes.

KID-expressing Ft nanoparticles (KID-NPs) could be phosphorylated by PKA and de-phosphorylated by lambda protein phosphatase (λPPase). Incubation of pre-phosphorylated KID-NPs (pKID-NPs) with KIX-expressing Ft nanoparticles (KIX-NPs) at a 3:2 ratio induced the formation of aggregates, as observed by dynamic light scattering (DLS). These aggregates showed 4.5-fold larger radii than that observed when

KIX-NPs were mixed with unphosphorylated KID-NPs (Fig 1c). Adding PKA to a mixture of KID-NPs and KIX-NPs resulted in a similar level of aggregation. PKA-induced aggregation could be prevented by adding a PKA inhibitor. Adding λPPase to a mixture of pKID-NPs and KIX-NPs also resulted in smaller aggregate sizes (Fig 1c). Changes in KID-LF phosphorylation under these conditions were confirmed with subsequent SDS-PAGE and phosphoprotein staining (Fig 1d).

Non-invasive sensing of PKA activity was performed in a 4.7T MRI magnet using a spin-echo acquisition sequence. Incubation of the sensor (3:2 ratio of KID-NPs with KIX-NPs) with PKA for 2 hours produced an increase of ~ 84% in the transverse relaxivity (r_2, calculated by subtracting the T2 relaxation rate of sensor-free buffer) from $0.53 \pm 0.06\ s^{-1}$ to $0.98 \pm 0.03\ s^{-1}$ (Fig 2a). At an echo time (TE) of 210 msec this corresponded to a 10.7 ± 1.3 % change in MRI signal intensity. PKA-dependent r_2 change could be prevented by adding a PKA inhibitor (Fig 2a). Similarly, a pre-phosphorylated sensor mixture had a relaxivity of $0.95 \pm 0.10\ s^{-1}$, which was reduced to $0.49 \pm 0.11\ s^{-1}$ in the presence of λPPase. Dynamical MRI measurements enabled real-time monitoring of PKA activity, with increases in r_2 happening faster with higher concentrations of PKA (Fig 2b).

Effective performance of the sensor depended on the quantity of functional groups displayed on the nanoparticle surface and the ratio of KID-NPs to KIX-NPs in the sensor mixture. When the quantity of transfected KID-LF or KIX-LF plasmid relative to wild-type and FLAG-LF plasmids was changed from 60% to 40%, 20% or 0% (decreases from 60% were compensated by an equal increase in LF), phosphorylation-dependent effects on r_2 were eliminated (Fig 3a). For particles of a fixed transfection composition, the ratio of pKID-NPs to KIX-NPs in the sensor mixture (D:X) influenced the level and dynamics of aggregation (Fig 3b). Although low D:X ratios ($\leq$1:1) produce the greatest maximal signal in the phosphorylated condition, they lose relaxivity after short periods, ostensibly due to over-aggregation, and show a significant change in r_2 in the unphosphorylated state. A high D:X ratio ($\geq$3:1) resulted in little phosphorylation-dependent contrast. A medium D:X ratio -- 3:2 -- showed the greatest phosphorylation-dependent contrast change on the 1-2 hour timescale; we therefore used this ratio throughout the rest of this article.

Our results represent the first *in vitro* proof of concept for a completely protein-based MRI sensor incorporating Ft, and suggest a general approach to creating future sensors for non-invasive molecular imaging through genetically directed self-assembly of multifunctional protein nanoparticles. To create a novel MRI sensor of PKA activity, we fused KID, KIX and 3xFLAG functionalities to the Ft light chain and co-expressed the resulting constructs in mammalian cells at desired ratios, yielding multifunctional Ft nanoparticles. We demonstrated that the fused functional groups conferred their properties onto the particles (FLAG purification, KID phosphorylation, de-phosphorylation), and that PKA caused a mixture of KID- and KIX- functionalized nanoparticles to aggregate. PKA-induced aggregation produced an 84% change in transverse relaxivity in MRI, allowing these nanoparticles to act as a dynamic non-invasive sensor of PKA activity. Comparisons of Ft sensors with different levels of nanoparticle functionalization and D:X ratios revealed valuable engineering principles that will aid in optimizing the performance of this sensor and of future sensors of this type.

Our ability to apply the traditional protein engineering method of fusion construction to the design of our PKA sensor and our ability to easily synthesize intact self-assembled sensor particles through expression in mammalian cells highlight two advantages of a protein-based approach to MRI sensor development. Future i*n vivo* applications of this or similar sensors may demonstrate a third potential advantage: ability to deliver sensors to cells or tissues as either purified molecules or as gene constructs to be expressed by the target cells.

METHODS

Fusion gene construction

Light-chain Ft fusion constructs were generated using standard molecular cloning techniques. Original genes encoding human Ft were kindly supplied by Paulo Arosio; genes encoding rat CREB and mouse CBP were obtained from Michael Greenberg. KID-LF encodes amino acids 88-160 of CREB, followed by the spacer GTSSEFM, and LF. KIX-LF encodes amino acids 574-686 of CBP, followed by the same spacer and LF. FLAG-LF encodes the amino acid sequence MDYKDHDGDYKDHDIDYKDDDDK in place of KID or KIX. All three constructs and LF and HF were cloned into the pCMV-Sport vector (Invitrogen, Carlsbad, CA) for expression in mammalian cells under the CMV promoter.

Ft nanoparticle expression and purification

Ft nanoparticles were expressed in suspension-cultured HEK-293 cells using the Freestyle293 system (Invitrogen) in accordance with manufacturer instructions. Plasmids encoding HF, LF, FLAG-LF and either KID-LF or KIX-LF were mixed and transfected into cells at pre-determined ratios (by DNA mass). For a 60% functional group composition, the plasmid mixture contained 60% KID-LF or KIX-LF, 20% FLAG-LF, 10% HF and 10% LF. After four days, cells were harvested and lysed in lysis buffer (50mM Tris-HCl, 150mM NaCl, 1mM EDTA, 1% Triton X-100, pH 7.4, 6ml per pellet generated from a 50mL culture) supplemented with a protease inhibitor cocktail (Halt, Pierce, Rockford, IL). Cleared lysates were supplemented overnight with 2mM Ferrous Ammonium Sulfate (Sigma) at 4°C. Anti-FLAG agarose (Ez-view, Sigma) was added for an additional 2 hours. After washing with wash buffer (50mM Tris-HCl, 150mM NaCl, pH 7.4), the nanoparticles were eluted with 0.1 M glycine at pH 3.5, then quenched with 10X wash buffer. Prior to subsequent handling, nanoparticles were concentrated using centrifugal filter units and buffer was exchanged to the assay buffer (10mM HEPES, 150mM NaCl, pH 7.4) using size-exclusion chromatography. Particle concentration was estimated by absorbance at 280nm, as calibrated by ELISA (Leinco, St. Louis, MO). Concentrations are given on a per-nanoparticle basis.

Phosphorylation and dephosphorylation

Phosphorylation was carried out by the addition of the recombinant catalytic subunit of protein kinase A (PKA, Promega, Madison, WI) and 1mM ATP (EMD Chemicals, San Diego, CA). For pre-phosphorylation, ~50 units of PKA were used per pmol of Ft. In DLS and MRI experiments, PKA was added directly from its original stock solution. To inhibit PKA activity, we used a peptide PKA inhibitor (Promega). Dephosphorylation was accomplished using lambda protein phosphatase (λPPase, New England Biolabs, Ipswich, MA), which was diluted in assay buffer and concentrated ~10-fold relative to its stock solution. Protein phosphorylation states were assayed by electrophoresis on 15% SDS-PAGE gels (BioRad, Hercules, CA) and staining using the Pro-Q Diamond phosphoprotein staining kit (Invitrogen). In gel images shown here, lanes have been re-arranged digitally to align them in the order of data presented in accompanying figures.

DLS

DLS measurements were performed using a DynaPro DLS system (Wyatt Technology, Santa Barbara, CA) at 25°C. For each sample (20μL), a single intensity-weighted value was used to characterize the average size of all particles in the specimen. This value was an average of 60 measurements acquired over one minute.

MRI

Samples (60-100 μL) were arrayed into microtiter plates and placed in a 40-cm-bore Bruker (Billerica, MA) Avance 4.7 T MRI scanner, equipped with a 10 cm inner diameter birdcage resonator radiofrequency coil and 26 G/cm triple axis gradients. Unused wells of the microtiter plates were filled with phosphate buffered saline, and imaging was performed on a 1.63mm slice through the sample. A *T2*-weighted spin echo pulse sequence with multiecho acquisition was used; repetition time (*TR*) was 4 s, and *TE* ranged from 30 to 900 ms, in 30-ms increments. Each acquisition took 8.5 min. Data matrices of 512 x 128 points were acquired and zero-filled to 1024 x 512 points, where the second dimension corresponds to the phase encoding direction. Images were reconstructed and analyzed using custom routines running in Matlab. Relaxation rates reported here were calculated by exponential fitting to the image data. Contrast was adjusted to produce MRI images presented in the figures.

ACKNOWLEDGEMENTS

The authors wish to thank Niyatee Samudra for assistance with DNA cloning. MGS wishes to acknowledge the Fannie and John Hertz Foundation and the Paul and Daisy Soros Fellowship for generous support. This work was funded in part by a New Innovator Award NIH DP2-OD2441to AJ, and NIH grant number R01-DE013023-08 to RL.

FIGURE LEGENDS

Figure 1. Ft nanoparticle sensors self-assemble and aggregate in response to PKA activity. (a) Diagram of the PKA sensor. Ft nanoparticles express either KID or KIX on their surfaces. When KID is phosphorylated by PKA, the pKID and KIX moieties bind, causing the nanoparticles to aggregate. Particles also express 3xFLAG groups for purification and electrostatic stabilization. (b) Coomassie-stained SDS-PAGE gels showing the composition of FLAG-purified nanoparticles self-assembled from subunits of HF, LF, FLAG-LF (expected m.w. 23.5 kDA) and either KID-LF (expected m.w. 29 kDA) or KIX-LF (expected m.w. 33.6 kDA). HF and LF appear as a combined band near 20kDa. (c) DLS measurements of relative radius for 3:2 mixtures of KID-NPs and KIX-NPs incubated for 3.5 hours under the indicated conditions. (1) KIX-NPs and unphosphorylated KID-NPs; (2) KIX-NPs and pre-phosphorylated KID-NPs; (3) unphosphorylated sensor with 12.7 units PKA per pmol Ft and 1mM ATP; (4) unphosphorylated sensor with just ATP; (5) unphosphorylated sensor with PKA, ATP and 100uM PKA inhibitor; (6) pre-phosphorylated sensor with 1026 units λPPase per pmol Ft. N=3 for each sample. Insert: mass-weighted size distribution for clusters under conditions (1) and (2). (d) SDS-PAGE gel stained for phosphoproteins (top) then coomassie stained (bottom). Lanes correspond to conditions (1)-(6) in (c). In the top gel, bands shown correspond to the known location of KID-LF; in the bottom gel, KIX-LF and KID-LF bands are both visible, with the KIX-LF appearing above KID-LF.

Figure 2. Sensors enhance T2 relaxation in MRI in response to PKA activity. (a)

measurements of the transverse relaxivity (r_2) after 2 hours of sensor incubation under the conditions listed in Fig. 1 (c). For each condition, r_2 was calculated by subtracting from 1/T2 the relaxation rate of sensor-free assay buffer containing an identical quantity of non-Ft species. Insert: T2-weigted MRI image (TE = 210 ms, TR= 4 sec) of wells containing samples corresponding to conditions (1)-(6). (b) Time course of MRI relaxation enhancement for sensor incubated with 460 (filled circles), 230 (filled squares), 115 (open circles) or 0 (open squares) units of PKA, 1mM ATP. Time indicated is from when PKA was added. N=3 for all data points.

Figure 3. Sensor performance depends on level of functionalization and ratio of partner particles. (a) Relaxivities (top) and relative radii (bottom) of 3:2 mixtures of KID-NPs and KIX-NPs expressed with various levels of functional group DNA, as described in the text. Unphosphorylated sensors (white) and pre-phosphorylated sensors (gray) were tested at each level of functionalization. (b) Timecourses of transverse relaxation rates when 60% functionalized KID-NPs and KIX-NPs are mixed at different KID-NP : KIX-NP ratios, with KID-NPs pre-phosphorylated (top) or unphosphorylated (middle). The bottom plot shows the difference between the phosphorylated and unphosphorylated conditions at each ratio. The D:X ratios shown are 2:3 (filled squares), 1:1 (filled circles), 3:2 (open squares) and 3:1 (open circles). N=2 for all data points.

Figure 1

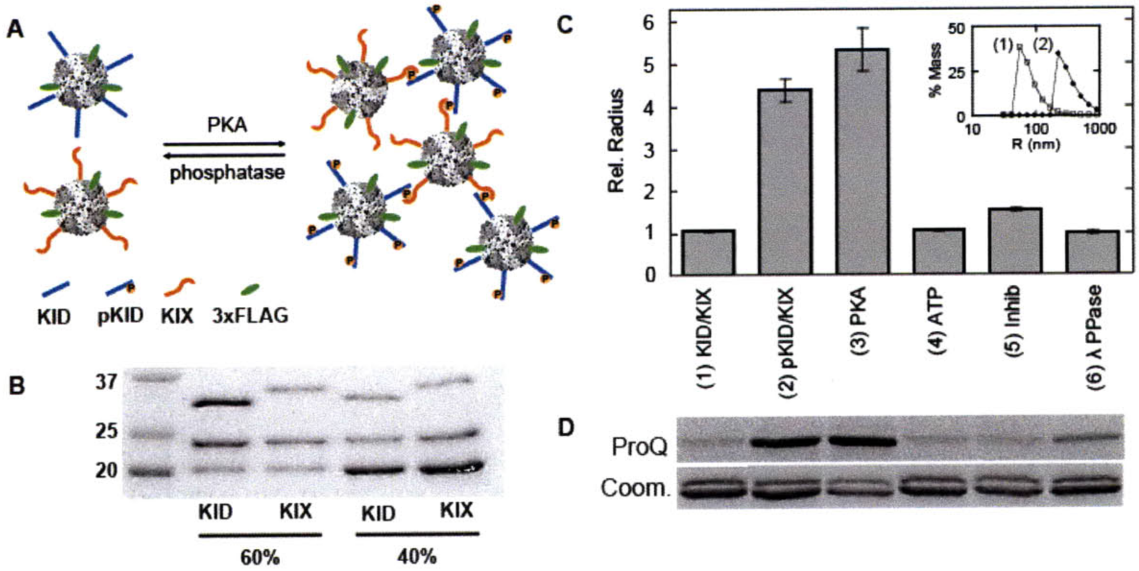
A
PKA
phosphatase
P
KID
pKID
KIX
3xFLAG
B
37
25
20
KID
KIX
KID
KIX
60%
40%
C
Rel. Radius
0
1
2
3
4
5
6
(1) KID/KIX
(2) pKID/KIX
(3) PKA
(4) ATP
(5) Inhib
(6) λ PPase
% Mass
50
25
0
(1)
(2)
10
100
1000
R (nm)
D
ProQ
Coom.

Figure 2

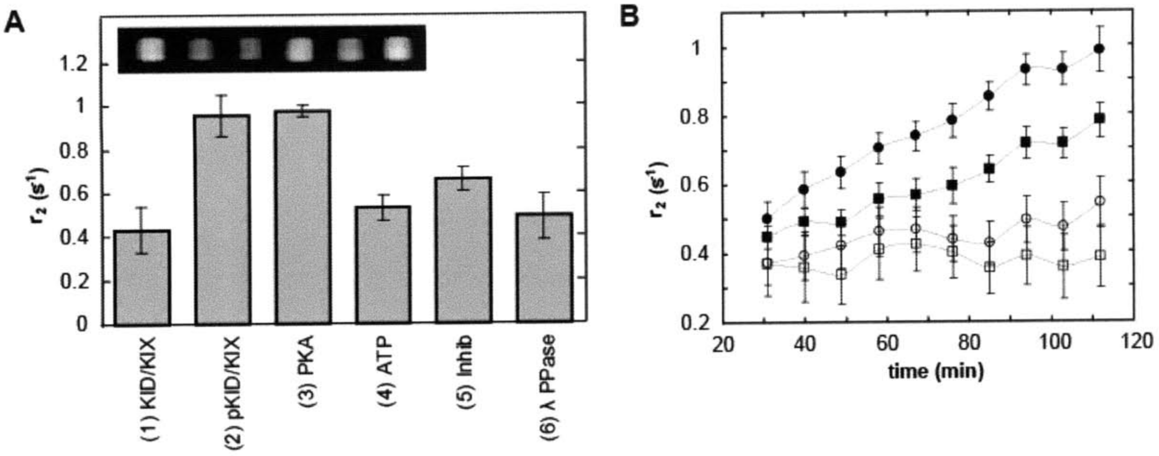
A
1.2
1
0.8
0.6
0.4
0.2
0
r_2 (s^{-1})
(1) KID/KIX
(2) pKID/KIX
(3) PKA
(4) ATP
(5) Inhib
(6) λ PPase
B
1
0.8
0.6
0.4
0.2
r_2 (s^{-1})
20
40
60
80
100
120
time (min)

Figure 3

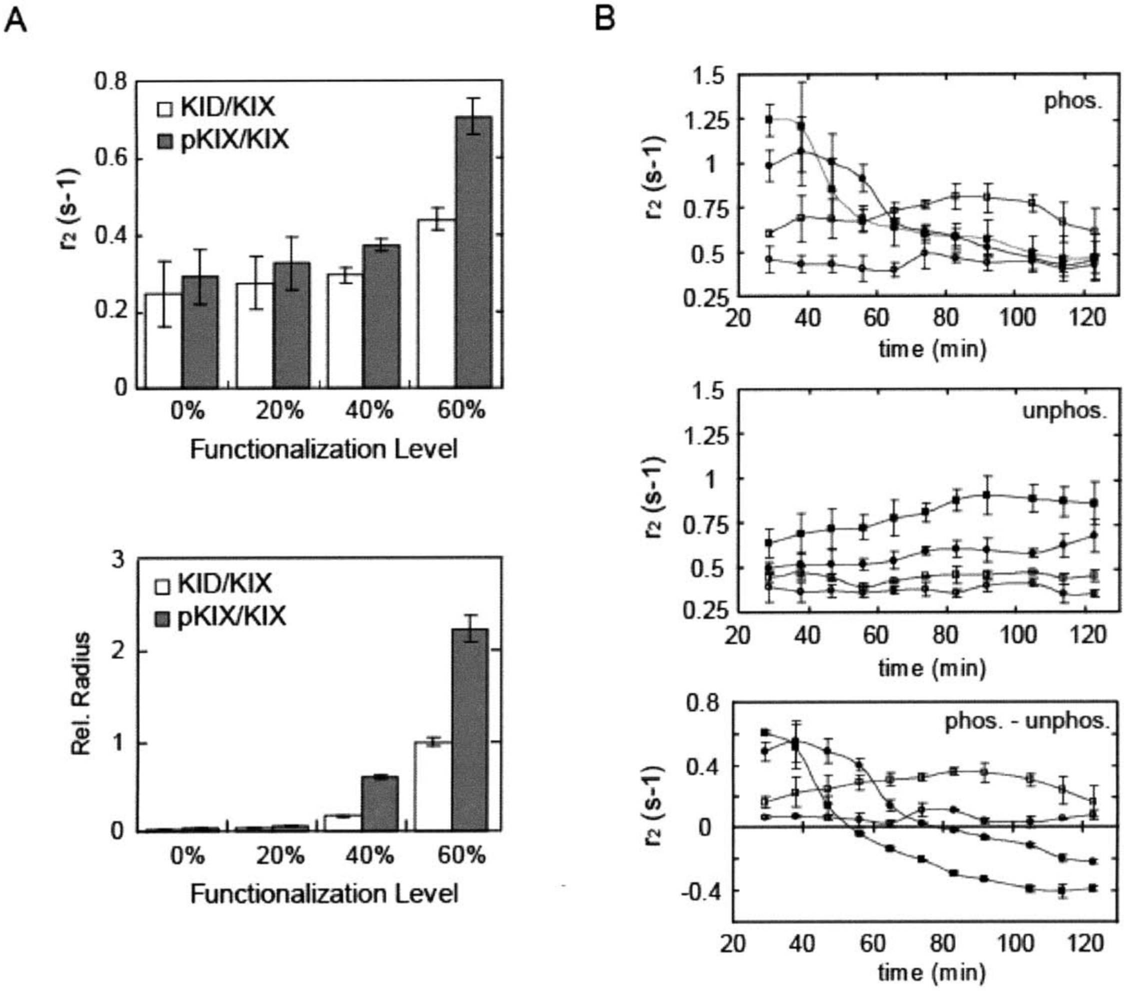
A
B
0.8
0.6
0.4
0.2
0
□ KID/KIX
■ pKIX/KIX
r2 (s-1)
0%
20%
40%
60%
Functionalization Level
3
2
1
0
Rel. Radius
□ KID/KIX
■ pKIX/KIX
0%
20%
40%
60%
Functionalization Level
1.5
1.25
1
0.75
0.5
0.25
r2 (s-1)
phos.
20
40
60
80
100
120
time (min)
1.5
1.25
1
0.75
0.5
0.25
r2 (s-1)
unphos.
20
40
60
80
100
120
time (min)
0.8
0.4
0
-0.4
r2 (s-1)
phos. - unphos.
20
40
60
80
100
120
time (min)

SUPPLEMENTARY MATERIAL

Amino acid sequences of Ft fusion constructs

Functional domains are highlighted in **bold**, linkers are highlighted in *italic*, and LF is in relular font.

KID-LF:

MGSSCKDLKRLFSGTQISTIAESEDSQESVDSVTDSQKRREILSRRPSYR 50

KILNDLSSDAPGVPRIEEEKSEEET*GTSSEFM*SSQIRQNYSTDVEAAVNS 100

LVNLYLQASYTYLSLGFYFDRDDVALEGVSHFFRELAEEKREGYERLLKM 150

QNQRGGRALFQDIKKPAEDEWGKTPDAMKAAMALEKKLNQALLDLHALGS 200

ARTDPHLCDFLETHFLDEEVKLIKKMGDHLTNLHRLGGPEAGLGEYLFER 250

LTLKHD

KIX-LF:

MSTIPTAAPPSSTGVRKGWHEHVTQDLRSHLVHKLVQAIFPTPDPAALKD 50

RRMENLVAYAKKVEGDMYESANSRDEYYHLLAEKIYKIQKELEEKRRSRL 100

HKQGILGNQPALPA*GTSSEFM*SSQIRQNYSTDVEAAVNSLVNLYLQASYT 150

YLSLGFYFDRDDVALEGVSHFFRELAEEKREGYERLLKMQNQRGGRALFQ 200

DIKKPAEDEWGKTPDAMKAAMALEKKLNQALLDLHALGSARTDPHLCDFL 250

ETHFLDEEVKLIKKMGDHLTNLHRLGGPEAGLGEYLFERLTLKHD

FLAG-LF:

MDYKDHDGDYKDHDIDYKDDDDK*GTSSEFM*SSQIRQNYSTDVEAAVNSLV 50

NLYLQASYTYLSLGFYFDRDDVALEGVSHFFRELAEEKREGYERLLKMQN 100

QRGGRALFQDIKKPAEDEWGKTPDAMKAAMALEKKLNQALLDLHALGSAR 150

TDPHLCDFLETHFLDEEVKLIKKMGDHLTNLHRLGGPEAGLGEYLFERLT 200

LKHD

5. Conclusions and Future Directions

This thesis has described two new protein platforms for the development of genetically engineered molecular sensors for MRI, and provided a theoretical framework for a quantitative understanding of the performance characteristics of these and other sensors. This work represents an important initial step in the development of a new class of technologies that may some day find widespread use in science and medicine. However, substantial improvements over our initial prototypes will be needed to reach this ambitious goal.

BM3h platform: future improvements

Of the two platforms we introduced, the greatest amount of progress has been demonstrated with BM3h. We showed that our novel methods for directed evolution of sensor specificity allowed us to create sensors for DA in a relatively straightforward process. We showed that the resulting sensors could be used to quantify DA release from cultured cells and image the dynamics of DA transport in the brains of rats exposed to cocaine. That a protein whose native activity was to catalyze chemical modifications of fatty acids could, with 9 mutations, be turned into a non-invasive sensor of neurotransmitter dynamics is remarkable. However, at least two significant challenges must be addressed to broaden the utility of BM3h-based sensors.

First, the overall (ligand-free) T1 relaxivity of BM3h, at ~1.2 $mM^{-1}s^{-1}$, is low relative to synthetic contrast agents. Even in dynamical imaging paradigms (which can accept weaker signals because temporal noise is typically lower than spatial noise), BM3h must be used at concentrations >10uM to elicit detectable changes in MRI signal. This means it can only sense those targets, such as DA, that are active at or above this concentration in a given tissue. In the brain, this rules out the use of this sensor to image glutamate, GABA, glycine and other dilute, local neurotransmitters. Only more concentrated molecules like DA, serotonin, norepinephrine and melatonin could be detected.

Several approaches could be tried to improve BM3h's sensitivity as a contrast agent. Its ligand-free relaxivity depends on the number of unpaired electrons in its heme-bound metal ion and the exchange rate of water molecules coordinated to this ion. Since the iron (III) in BM3h normally exists in a mixed 1/2 – 5/2 spin state with spin 1/2 predominating, one may attempt to improve relaxivity by mutating the protein so as to make its high-spin state more favored. Since this depends on the iron atom's immediate electronic environment, mutagenesis should be focused around the heme pocket and in particular on the non-heme ligand C399. Another approach might be to change the metal contained in BM3h. Porphyrins are available with various other metals, including Mn, Ni and Co. Because these metals have different d-orbital electron configurations than iron does, they could possess a higher spin number in BM3h. Transmetallation could be carried out by refolding denatured BM3h in the presence of the desired metal heme. A drawback of this approach is that it involves modifying the sensor after it is expressed, confining its utility to cases where it can be delivered in its intact form rather than as a genetic construct. Another way to potentially improve relaxivity is to increase water exchange rates at the open coordination site on the metal ion. This would likely require mutations in the protein that are difficult to predict, and would therefore need to be done through a high-throughput screen. Unfortunately, if the readout of such a screen is MRI, then the relatively high noise levels of this modality (compared with optical spectroscopy) would make such a screen inefficient.

A second challenge for BM3h is to show it can work for intracellular sensing. Many interesting signaling processes occur inside cells, and indeed even intracellular sensing of DA may find clinical utility in therapies aimed at replacing lost dopaminergic cells. For BM3h to be a useful intracellular sensor, it must be shown that this protein can be expressed at high levels in mammalian cells and find sufficient iron heme to be detectable. It must also be able to sense its target without, through its own interaction with it, significantly altering its function. A first step in this direction has been taken with the creation of a mammalian codon-optimized version of BM3h-8C8 and a demonstration that it can be expressed in mammalian cells to >1% of total cell protein (see appendix A).

BM3h platform: potential applications

BM3h-based sensors could be applied in scientific and clinical imaging in several formats. As we demonstrated in our initial proof of concept, BM3h could be injected directly into a site of interest in the brain, where it could sense the dynamics of a target neurotransmitter. In our proof of concept studies, we co-injected an appropriate quantity the neurotransmitter and imaged its transport. Direct sensor injections could also be used experimentally to monitor the release and reuptake of endogenous neurotransmitters, if such processes can be temporally coupled to imaging (e.g. via electrical stimulation).

Of course, since a key attraction of MRI is its ability to simultaneously image large volumes of tissue, it may be desirable to deliver BM3h more widely in the brain and image target molecule dynamics in a spatially resolved manner. To do this, methods of delivering the sensor to larger volumes will need to be developed, potentially borrowing from the body of work on therapeutic delivery to the brain.

If intracellular sensing with BM3h can be demonstrated, BM3h-based sensors may also find utility as built-in reporters for transplanted cells. For example, much work has been done to develop dopaminergic cell replacement therapies for Parkinson's disease[112]. An unfulfilled need in this field has been a way to assay the viability and performance of transplanted cells. Since the intended activity of such cells is to produce and release DA, a sensor like BM3h-8C8 incorporated into their genome may be useful in reporting how well the transplanted cells are performing this function. Intracellular DA is typically trafficked to vesicles in preparation for release. A way to use a sensor like BM3h-8C8 could be to express it in the cytoplasm and monitor changes in T1-weighted signal after administration of vesicular transporter blockers.

Finally, the gene encoding BM3h could be delivered to endogenous cells using gene delivery technologies, where it could either serve as an intracellular sensor or be targeted for secretion to the extracellular space. As both viral and non-viral gene delivery methods continue to improve, genetically engineered sensors like BM3h-8C8 could find an increasing range of application in their genetic format.

Ferritin platform: future improvements

The data presented in this thesis demonstrates the viability of self-assembling multifunctional Ft nanoparticles to serve as a platform for the development of MRI sensors. Our initial sensor was targeted at protein kinase A, but our general methodology could be applied to the making of a variety of future sensors. As in BM3h, however, a number of challenges must be addressed to broaden the utility of the Ft platform.

Although Ft has already been shown to produce detectable static MRI contrast *in-vivo* despite its antiferromagnetic iron oxide core[28-30] (which has a weaker magnetic moment and per-iron relaxivity than do superparamagnetic cores), its utility in sensor design could be enhanced if relaxivity could be improved by altering its core to a superparamagnetic state. This has been done successfully through in-vitro iron loading in a tightly controlled chemical reaction[113], but since some of the more appealing future applications of Ft sensors are for intracellular sensing (see next section), it would be desirable to alter the protein itself to encourage superparamagnetic core formation under physiological conditions. This might be accomplished by modifying amino acid residues on Ft's inner surface to favor the nucleation of a particular crystalline structure, as has been done with other proteins[114].

To enable Ft-based sensors to be delivered in genetic as well as intact form, it may also be necessary to introduce an orthogonal system for the formation of multifunctional molecules that could serve as an aggregating partner for Ft nanoparticles. With our current constructs, co-transfection of KID-LF and KIX-LF with FLAG-modified and wild-type subunits would result in the formation of particles expressing both KID and KIX on their surface, the proximity of which to each other may cause them to interact within the same nanoparticle rather than with complimentary groups on other particles, thus preventing PKA-induced aggregation. Potential starting points for the development of orthogonal multimeric binding partners include tertameric streptavidin, trimeric p53, and a variety of dimeric coiled-coil motifs.

Ferritin platform: potential applications

Ft-based sensors may be useful in a variety of applications. In their purified protein form, sensors such as the one we described could be used to sense intracellular molecular signaling events after being introduced into cells via methods currently under development for synthetic nanoparticles (e.g. in combination with cell transfection reagents or via attachment of membrane-permeating moieties). In the future, genetic delivery of Ft-based sensors could enable long-term monitoring of intracellular signaling processes in endogenous tissues or transplanted cells. Unfunctionalized Ft has already been shown to express and provide static contrast *in vivo* after viral delivery or genomic incorporation in transgenic animals[28-30]. This suggests that a sensor such as the one we described, pending improvements discussed in the previous section, could likewise be targeted to endogenous tissues and provide functional sensing.

In each aforementioned application, Ft and could BM3h provide complimentary capabilities, since the former is better suited for imaging macromolecular activities that occur on longer timescales, while BM3h lends itself best to sensing small molecules. The fact that BM3h and Ft produce T1 and T2 contrast, respectively, suggests that pulse sequences could be used to distinguish between the signals generated by these probes.

References

1. Massoud, T.F. & Gambhir, S.S. Molecular imaging in living subjects: seeing fundamental biological processes in a new light. *Genes Dev* **17**, 545-580 (2003).
2. Johnson, I. Fluorescent probes for living cells. *Histochem J* **30**, 123-140 (1998).
3. Griesbeck, O. Fluorescent proteins as sensors for cellular functions. *Curr Opin Neurobiol* **14**, 636-641 (2004).
4. Miyawaki, A. Innovations in the imaging of brain functions using fluorescent proteins. *Neuron* **48**, 189-199 (2005).
5. Delbeke, D. & Martin, W.H. Metabolic imaging with FDG: a primer. *Cancer J* **10**, 201-213 (2004).
6. Tai, Y.F. & Piccini, P. Applications of positron emission tomography (PET) in neurology. *J Neurol Neurosurg Psychiatry* **75**, 669-676 (2004).
7. Dickerson, B.C. Advances in functional magnetic resonance imaging: technology and clinical applications. *Neurotherapeutics* **4**, 360-370 (2007).
8. Morris, E.A. Breast cancer imaging with MRI. *Radiol Clin North Am* **40**, 443-466 (2002).
9. Yuh, W.T. et al. Clinical magnetic resonance imaging of brain tumors at ultrahigh field: a state-of-the-art review. *Top Magn Reson Imaging* **17**, 53-61 (2006).
10. Jagust, W.J. et al. Neuropathological basis of magnetic resonance images in aging and dementia. *Ann Neurol* **63**, 72-80 (2008).
11. de Roos, A., Doornbos, J., Baleriaux, D., Bloem, H.L. & Falke, T.H. Clinical applications of gadolinium-DTPA in MRI. *Magn Reson Annu*, 113-145 (1988).

12. Thorek, D.L., Chen, A.K., Czupryna, J. & Tsourkas, A. Superparamagnetic iron oxide nanoparticle probes for molecular imaging. *Ann Biomed Eng* **34**, 23-38 (2006).

13. Ward, K.M., Aletras, A.H. & Balaban, R.S. A new class of contrast agents for MRI based on proton chemical exchange dependent saturation transfer (CEST). *J Magn Reson* **143**, 79-87 (2000).

14. Li, W.H., Fraser, S.E. & Meade, T.J. A calcium-sensitive magnetic resonance imaging contrast agent. *J Am Chem Soc* **121**, 1413-1414 (1999).

15. Perez, J.M., Josephson, L., O'Loughlin, T., Hogemann, D. & Weissleder, R. Magnetic relaxation switches capable of sensing molecular interactions. *Nat Biotechnol* **20**, 816-820 (2002).

16. Atanasijevic, T., Shusteff, M., Fam, P. & Jasanoff, A. Calcium-sensitive MRI contrast agents based on superparamagnetic iron oxide nanoparticles and calmodulin. *Proc Natl Acad Sci U S A* **103**, 14707-14712 (2006).

17. Zhou, J., Payen, J.F., Wilson, D.A., Traystman, R.J. & Van Zijl, P.C. Using the amide proton signals of intracellular proteins and peptides to detect pH effects in MRI. *Nat Med* (2003).

18. Raghunand, N., Zhang, S., Sherry, A.D. & Gillies, R.J. In vivo magnetic resonance imaging of tissue pH using a novel pH-sensitive contrast agent, GdDOTA-4AmP. *Acad Radiol* **9 Suppl 2**, S481-483 (2002).

19. Ho, C., Lindstrom, T.R., Baldassare, J.J. & Breen, J.J. Magnetic resonance studies of human hemoglobins and their implications to the structure-function

relationships in human normal and abnormal hemoglobins. *Ann N Y Acad Sci* **222**, 21-39 (1973).

20. Logothetis, N.K. & Pfeuffer, J. On the nature of the BOLD fMRI contrast mechanism. *Magn Reson Imaging* **22**, 1517-1531 (2004).

21. Munro, A.W. et al. P450 BM3: the very model of a modern flavocytochrome. *Trends Biochem Sci* **27**, 250-257 (2002).

22. Macdonald, I.D., Munro, A.W. & Smith, W.E. Fatty acid-induced alteration of the porphyrin macrocycle of cytochrome P450 BM3. *Biophys J* **74**, 3241-3249 (1998).

23. Ravichandran, K.G., Boddupalli, S.S., Hasermann, C.A., Peterson, J.A. & Deisenhofer, J. Crystal structure of hemoprotein domain of P450BM-3, a prototype for microsomal P450's. *Science* **261**, 731-736 (1993).

24. Modi, S. et al. NMR studies of substrate binding to cytochrome P450 BM3: comparisons to cytochrome P450 cam. *Biochemistry* **34**, 8982-8988 (1995).

25. Glieder, A., Farinas, E.T. & Arnold, F.H. Laboratory evolution of a soluble, self-sufficient, highly active alkane hydroxylase. *Nat Biotechnol* **20**, 1135-1139 (2002).

26. Otey, C.R., Bandara, G., Lalonde, J., Takahashi, K. & Arnold, F.H. Preparation of human metabolites of propranolol using laboratory-evolved bacterial cytochromes P450. *Biotechnol Bioeng* **93**, 494-499 (2006).

27. Harrison, P.M. & Arosio, P. The ferritins: molecular properties, iron storage function and cellular regulation. *Biochim Biophys Acta* **1275**, 161-203 (1996).

28. Genove, G., DeMarco, U., Xu, H., Goins, W.F. & Ahrens, E.T. A new transgene reporter for in vivo magnetic resonance imaging. *Nat Med* **11**, 450-454 (2005).

29. Cohen, B., Dafni, H., Meir, G., Harmelin, A. & Neeman, M. Ferritin as an endogenous MRI reporter for noninvasive imaging of gene expression in C6 glioma tumors. *Neoplasia* **7**, 109-117 (2005).

30. Cohen, B. et al. MRI detection of transcriptional regulation of gene expression in transgenic mice. *Nat Med* **13**, 498-503 (2007).

31. Gossuin, Y., Gillis, P., Muller, R.N. & Hocq, A. Relaxation by clustered ferritin: a model for ferritin-induced relaxation in vivo. *NMR Biomed* **20**, 749-756 (2007).

32. Bennett, K.M., Shapiro, E.M., Sotak, C.H. & Koretsky, A.P. Controlled aggregation of ferritin to modulate MRI relaxivity. *Biophys J* **95**, 342-351 (2008).

33. Atanasijevic, T. & Jasanoff, A. Preparation of iron oxide-based calcium sensors for MRI. *Nat Protoc* **2**, 2582-2589 (2007).

34. Kim, G.Y., Josephson, L., Langer, R. & Cima, M.J. Magnetic relaxation switch detection of human chorionic gonadotrophin. *Bioconjug Chem* **18**, 2024-2028 (2007).

35. Corsi, B. et al. Transient overexpression of human H- and L-ferritin chains in COS cells. *Biochem J* **330 (Pt 1)**, 315-320 (1998).

36. Kim, S.W., Kim, Y.H. & Lee, J. Thermal stability of human ferritin: concentration dependence and enhanced stability of an N-terminal fusion mutant. *Biochem Biophys Res Commun* **289**, 125-129 (2001).

37. Schultz, W. Multiple dopamine functions at different time courses. *Annu Rev Neurosci* **30**, 259-288 (2007).

38. Hyman, S.E., Malenka, R.C. & Nestler, E.J. Neural Mechanisms of Addiction: The Role of Reward-Related Learning and Memory. *Annu Rev Neurosci* (2006).

39. Damier, P., Hirsch, E.C., Agid, Y. & Graybiel, A.M. The substantia nigra of the human brain. II. Patterns of loss of dopamine-containing neurons in Parkinson's disease. *Brain* **122 (Pt 8)**, 1437-1448 (1999).

40. Young, A.M., Joseph, M.H. & Gray, J.A. Increased dopamine release in vivo in nucleus accumbens and caudate nucleus of the rat during drinking: a microdialysis study. *Neuroscience* **48**, 871-876 (1992).

41. Garris, P.A. & Wightman, R.M. Different kinetics govern dopaminergic transmission in the amygdala, prefrontal cortex, and striatum: an in vivo voltammetric study. *J Neurosci* **14**, 442-450 (1994).

42. Lindsey, K.P. & Gatley, S.J. Applications of clinical dopamine imaging. *Neuroimaging Clin N Am* **16**, 553-573, vii-viii (2006).

43. Ewing, A.G., Bigelow, J.C. & Wightman, R.M. Direct in vivo monitoring of dopamine released from two striatal compartments in the rat. *Science* **221**, 169-171 (1983).

44. Michael, A.C., Ikeda, M. & Justice, J.B., Jr. Mechanisms contributing to the recovery of striatal releasable dopamine following MFB stimulation. *Brain Res* **421**, 325-335 (1987).

45. Duong, T.Q., Kim, D.S., Ugurbil, K. & Kim, S.G. Spatiotemporal dynamics of the BOLD fMRI signals: toward mapping submillimeter cortical columns using the early negative response. *Magn Reson Med* **44**, 231-242 (2000).

46. Arnsten, A.F., Ramos, B.P., Birnbaum, S.G. & Taylor, J.R. Protein kinase A as a therapeutic target for memory disorders: rationale and challenges. *Trends Mol Med* **11**, 121-128 (2005).

47. Carlezon, W.A., Jr., Duman, R.S. & Nestler, E.J. The many faces of CREB. *Trends Neurosci* **28**, 436-445 (2005).

48. Parker, D. et al. Phosphorylation of CREB at Ser-133 induces complex formation with CREB-binding protein via a direct mechanism. *Mol Cell Biol* **16**, 694-703 (1996).

49. Chrivia, J.C. et al. Phosphorylated CREB binds specifically to the nuclear protein CBP. *Nature* **365**, 855-859 (1993).

50. Kwok, R.P. et al. Nuclear protein CBP is a coactivator for the transcription factor CREB. *Nature* **370**, 223-226 (1994).

51. Nagai, Y. et al. A fluorescent indicator for visualizing cAMP-induced phosphorylation in vivo. *Nat Biotechnol* **18**, 313-316 (2000).

52. Spotts, J.M., Dolmetsch, R.E. & Greenberg, M.E. Time-lapse imaging of a dynamic phosphorylation-dependent protein-protein interaction in mammalian cells. *Proc Natl Acad Sci U S A* **99**, 15142-15147 (2002).

53. Schmitt, F., Stehling, M.K. & Turner, R. Echo-Planar Imaging: Theory, Technique, and Application. (Springer Verlag, Berlin; 1998).

54. Meade, T.J., Taylor, A.K. & Bull, S.R. New magnetic resonance contrast agents as biochemical reporters. *Curr Opin Neurobiol* **13**, 597-602 (2003).

55. Jasanoff, A. Functional MRI using molecular imaging agents. *Trends Neurosci* **28**, 120-126 (2005).

56. Kayyem, J.F., Kumar, R.M., Fraser, S.E. & Meade, T.J. Receptor-Targeted Co-transport of DNA and Magnetic Resonance Contrast Agents. *Chem. Biol.* **2**, 615-620 (1995).

57. Louie, A.Y. et al. In vivo visualization of gene expression using magnetic resonance imaging [In Process Citation]. *Nat Biotechnol* **18**, 321-325 (2000).

58. Zhao, M., Beauregard, D.A., Loizou, L., Davletov, B. & Brindle, K.M. Non-invasive detection of apoptosis using magnetic resonance imaging and a targeted contrast agent. *Nat Med* **7**, 1241-1244. (2001).

59. Lowe, M.P. et al. pH-dependent modulation of relaxivity and luminescence in macrocyclic gadolinium and europium complexes based on reversible intramolecular sulfonamide ligation. *J Am Chem Soc* **123**, 7601-7609 (2001).

60. Aime, S. et al. Paramagnetic lanthanide(III) complexes as pH-sensitive chemical exchange saturation transfer (CEST) contrast agents for MRI applications. *Magn Reson Med* **47**, 639-648 (2002).

61. Zhou, J., Lal, B., Wilson, D.A., Laterra, J. & van Zijl, P.C. Amide proton transfer (APT) contrast for imaging of brain tumors. *Magn Reson Med* **50**, 1120-1126 (2003).

62. Aime, S., Botta, M., Gianolio, E. & Terreno, E. A p(O2)-Responsive MRI Contrast Agent Based on the Redox Switch of Manganese(II/III)-Porphyrin Complexes. *Angew. Chem. Int. Ed.* **39**, 747-750 (2000).

63. Sun, P.Z., Schoening, Z.B. & Jasanoff, A. In vivo oxygen detection using exogenous hemoglobin as a contrast agent in magnetic resonance microscopy. *Magn Reson Med* **49**, 609-614 (2003).

64. Hanaoka, K. et al. Design and synthesis of a novel magnetic resonance imaging contrast agent for selective sensing of zinc ion. *Chem Biol* **9**, 1027-1032. (2002).

65. Aime, S., Delli Castelli, D., Fedeli, F. & Terreno, E. A paramagnetic MRI-CEST agent responsive to lactate concentration. *J Am Chem Soc* **124**, 9364-9365 (2002).

66. Lauffer, R.B. Paramagnetic metal complexes as water proton relaxation agents for NMR imaging: theory and design. *Chem Rev* **87**, 901-927 (1987).

67. Zhang, S., Trokowski, R. & Sherry, A.D. A paramagnetic CEST agent for imaging glucose by MRI. *J Am Chem Soc* **125**, 15288-15289 (2003).

68. Zhou, J., Wilson, D.A., Sun, P.Z., Klaus, J.A. & Van Zijl, P.C. Quantitative description of proton exchange processes between water and endogenous and exogenous agents for WEX, CEST, and APT experiments. *Magn Reson Med* **51**, 945-952 (2004).

69. Ahrens, E.T., Rothbacher, U., Jacobs, R.E. & Fraser, S.E. A model for MRI contrast enhancement using T1 agents. *Proc Natl Acad Sci U S A* **95**, 8443-8448 (1998).

70. Allen, M.J. & Meade, T.J. Magnetic resonance contrast agents for medical and molecular imaging. *Met Ions Biol Syst* **42**, 1-38 (2004).

71. Woessner, D.E., Zhang, S., Merritt, M.E. & Sherry, A.D. Numerical solution of the Bloch equations provides insights into the optimum design of PARACEST agents for MRI. *Magn Reson Med* **53**, 790-799 (2005).

72. Dahnke, H. & Schaeffter, T. Limits of detection of SPIO at 3.0 T using T2 relaxometry. *Magn Reson Med* **53**, 1202-1206 (2005).

73. Odriozola, G. et al. A probabilistic aggregation kernel for the computer-simulated transition from DLCA to RLCA. *Europhysics Letters* **53**, 797-803 (2001).

74. Laurenzi, I.J. & Diamond, S.L. Kinetics of random aggregation-fragmentation processes with multiple components. *Phys Rev E Stat Nonlin Soft Matter Phys* **67**, 051103 (2003).

75. Callaghan, P.T. Principles of Nuclear Magnetic Resonance Microscopy. (Oxford University Press, Oxford, UK; 1993).

76. Toth, E., Helm, L. & Merbach, A.E. in The Chemistry of Contrast Agents in Medical Magnetic Resonance Imaging. (eds. A.E. Merbach & E. Toth) (John Wiley & Sons, New York; 2001).

77. Li, W.H., Parigi, G., Fragai, M., Luchinat, C. & Meade, T.J. Mechanistic studies of a calcium-dependent MRI contrast agent. *Inorg Chem* **41**, 4018-4024. (2002).

78. McHugh, J.M. & Kenyon, J.L. An Excel-based model of Ca2+ diffusion and fura 2 measurements in a spherical cell. *Am J Physiol Cell Physiol* **286**, C342-348 (2004).

79. De Leon-Rodriguez, L.M. et al. Magnetic resonance imaging detects a specific peptide-protein binding event. *J Am Chem Soc* **124**, 3514-3515 (2002).

80. Fersht, A.R. Enzyme Structure and Mechanism, Edn. 2nd. (W. H. Freement & Co., New York; 1985).

81. Lauffenburger, D.A. & Linderman, J.J. Receptors: Models for Binding, Trafficking, and Signaling. (Oxford University Press, New York; 1993).

82. Ogawa, S. et al. Intrinsic signal changes accompanying sensory stimulation: functional brain mapping with magnetic resonance imaging. *Proc Natl Acad Sci USA* **89**, 5951-5955 (1992).

83. Chen, Y.C. et al. Improved mapping of pharmacologically induced neuronal activation using the IRON technique with superparamagnetic blood pool agents. *J Magn Reson Imaging* **14**, 517-524. (2001).

84. Farinas, E.T., Bulter, T. & Arnold, F.H. Directed enzyme evolution. *Curr Opin Biotechnol* **12**, 545-551 (2001).

85. Bonnemain, B. Superparamagnetic agents in magnetic resonance imaging: physicochemical characteristics and clinical applications. A review. *J Drug Target* **6**, 167-174. (1998).

86. Wang, Y.X., Hussain, S.M. & Krestin, G.P. Superparamagnetic iron oxide contrast agents: physicochemical characteristics and applications in MR imaging. *Eur Radiol* **11**, 2319-2331 (2001).

87. Josephson, L., Perez, J.M. & Weissleder, R. Magnetic Nanosensors for the Detection of Oligonucleotide Sequences. *Angew Chem Int Ed Engl* **40**, 3204-3206 (2001).

88. Atanasijevic, T., Fam, P.S. & Jasanoff, A. Protein-nanoparticle conjugates as dynamic calcium reporters for magnetic resonance imaging. *in preparation* (2005).

89. Smoluchowski, M. Versuch einer mathematischen Theorie der Koagulationskinetik kolloider Losungen. *Z Phys Chem* **92**, 129-168 (1917).

90. Odriozola, G. et al. Constant bond breakup probability model for reversible aggregation processes. *Physical Review E* **65**, - (2002).

91. Verkman, A.S. Solute and macromolecule diffusion in cellular aqueous compartments. *Trends Biochem Sci* **27**, 27-33 (2002).

92. Roch, A., Gossuin, Y., Muller, R.N. & Gillis, P. Superparamagnetic colloid suspensions: Water magnetic relaxation and clustering. *J Magn Magn Mater* **293**, 532-539 (2005).

93. Shen, T., Weissleder, R., Papisov, M., Bogdanov, A., Jr. & Brady, T.J. Monocrystalline iron oxide nanocompounds (MION): physicochemical properties. *Magn Reson Med* **29**, 599-604 (1993).

94. Vicsek, T. Fractal Growth Phenomena, Edn. 2. (World Scientific, Hackensack, NJ; 1992).

95. Zhou, C.L., Zhao, Y., Jao, T.C., Wu, C. & Winnik, M.A. Effect of concentration on the photoinduced aggregation of polymer nanoparticles. *J Phys Chem B* **106**, 9514-9521 (2002).

96. Zhang, S., Merritt, M., Woessner, D.E., Lenkinski, R.E. & Sherry, A.D. PARACEST agents: modulating MRI contrast via water proton exchange. *Acc Chem Res* **36**, 783-790 (2003).

97. Zhang, Y.Z., Paterson, Y. & Roder, H. Rapid amide proton exchange rates in peptides and proteins measured by solvent quenching and two-dimensional NMR. *Protein Sci* **4**, 804-814 (1995).

98. Eigen, M. Proton transfer, acid-base catalysis, and enzymatic hydrolysis: Part I: Elementary Processes. *Angew Chem Int Ed Engl* **3**, 1-19 (1964).

99. Shapiro, M.G., Atanasijevic, T., Faas, H., Westmeyer, G.G. & Jasanoff, A. Dynamic imaging with MRI contrast agents: quantitative considerations. *Magn Reson Imaging* **24**, 449-462 (2006).

100. Jasanoff, A. MRI contrast agents for functional molecular imaging of brain activity. *Curr Opin Neurobiol* **17**, 593-600 (2007).

101. Lewis, D.F.V. Guide to cytochrome P450 structure and function. (Taylor & Francis, London ; New York; 2001).

102. Fasan, R., Chen, M.M., Crook, N.C. & Arnold, F.H. Engineered alkane-hydroxylating cytochrome P450(BM3) exhibiting nativelike catalytic properties. *Angew Chem Int Ed Engl* **46**, 8414-8418 (2007).

103. Bloom, J.D., Labthavikul, S.T., Otey, C.R. & Arnold, F.H. Protein stability promotes evolvability. *Proc Natl Acad Sci U S A* **103**, 5869-5874 (2006).

104. Greene, L.A. & Rein, G. Release, storage and uptake of catecholamines by a clonal cell line of nerve growth factor (NGF) responsive pheo-chromocytoma cells. *Brain Res* **129**, 247-263 (1977).

105. Ohnuma, K., Hayashi, Y., Furue, M., Kaneko, K. & Asashima, M. Serum-free culture conditions for serial subculture of undifferentiated PC12 cells. *J Neurosci Methods* **151**, 250-261 (2006).

106. Louie, A.Y. et al. In vivo visualization of gene expression using magnetic resonance imaging. *Nat Biotechnol* **18**, 321-325 (2000).

107. Chen, Y., Dalwadi, G. & Benson, H.A. Drug delivery across the blood-brain barrier. *Curr Drug Deliv* **1**, 361-376 (2004).

108. Callaway, E.M. A molecular and genetic arsenal for systems neuroscience. *Trends Neurosci* **28**, 196-201 (2005).

109. Barnes, H.J., Arlotto, M.P. & Waterman, M.R. Expression and enzymatic activity of recombinant cytochrome P450 17 alpha-hydroxylase in Escherichia coli. *Proc Natl Acad Sci U S A* **88**, 5597-5601 (1991).

110. Omura, T. & Sato, R. The Carbon Monoxide-Binding Pigment of Liver Microsomes. I. Evidence for Its Hemoprotein Nature. *J Biol Chem* **239**, 2370-2378 (1964).

111. Li, H. & Poulos, T.L. The structure of the cytochrome p450BM-3 haem domain complexed with the fatty acid substrate, palmitoleic acid. *Nat Struct Biol* **4**, 140-146 (1997).

112. Emerich, D.F. & Salzberg, H.C. Update on immunoisolation cell therapy for CNS diseases. *Cell Transplant* **10**, 3-24 (2001).

113. Meldrum, F.C., Heywood, B.R. & Mann, S. Magnetoferritin: in vitro synthesis of a novel magnetic protein. *Science* **257**, 522-523 (1992).

114. Klem, M.T. et al. Bio-inspired synthesis of protein-encapsulated CoPt nanoparticles. *Advanced Functional Materials* **15**, 1489-1494 (2005).

Appendix A – mammalian expression of BM3h

To set the stage for future work on the use of BM3h-based sensors as genetically targeted intracellular reporters in mammalian cells and animals, we created a mammalian codon-optimized version of the BM3h and BM3h-8C8 genes. This was deemed necessary after a comparison of codon usage between the BM3h gene with the codon frequency seen in human cells (Fig. 1a) revealed a high incidence of over-used codons that might serve as translational bottlenecks. A human codon-optimized sequence was generated using Gene Designer software (DNA2.0, Menlo Park, CA) with the BM3h amino acid sequence as an input, and synthesized by Blue Heron (Bothell, WA). The resulting gene sequence (see appendix C) was cloned into a PCMV-Sport vector (same as the one used for Ft expression), and transfected into HEK293 cells using the Freestyle293 expression system (Invitrogen). One day after transfection, cells we supplemented with 0-40uM hemin to ensure adequate supply of heme for expression and folding of BM3h. The hexahistidine tag fused to BM3h was then used to purify the protein from crude cell lysates after four days of expression. It was then run on SDS-PAGE, and its molecular weight compared to bacterially-expressed BM3h (Fig. 1b). The spectrum of mammalian cell-expressed BM3h looked normal (Fig. 1c). BM3h expression was measured by performing a CO assay on clarified lysates, and compared to total protein in the lysate measured by BCA assay (Pierce). Expression levels varied from 0.4% to 1.9% of total cell protein depending on the level of hemin supplementation during growth (Fig. 1d). However, after supplementation with high levels of hemin, a peak at 420nm was seen in the CO assay (Fig 1e), indicating that non-BM3h heme species remain in the cell lysates, possibly due to uptake of heme that does not get incorporated into BM3h. A medium concentration of heme supplement (e.g. 12uM) may offer the highest expression of BM3h without too much extra uptake of heme by the cells. At this level of supplementation, around 1.2% of total protein was BM3h. Assuming a typical net protein density of 150mg/ml in living tissues, this would correspond to a tissue BM3h concentration of ~30uM.

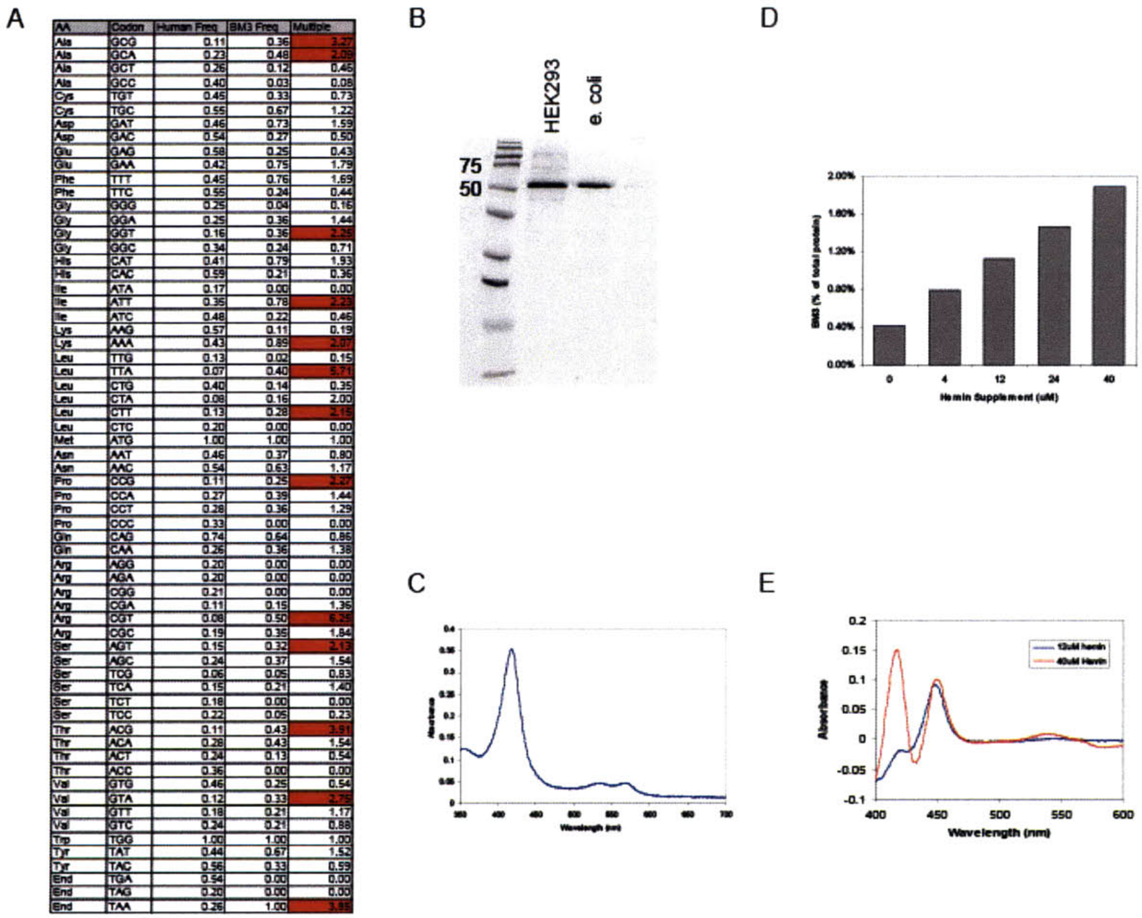

AA	Codon	Human Freq	BM3 Freq	Multiple
Ala	GCG	0.11	0.36	3.27
Ala	GCA	0.23	0.48	2.09
Ala	GCT	0.26	0.12	0.46
Ala	GCC	0.40	0.03	0.08
Cys	TGT	0.45	0.33	0.73
Cys	TGC	0.55	0.67	1.22
Asp	GAT	0.46	0.73	1.59
Asp	GAC	0.54	0.27	0.50
Glu	GAG	0.58	0.25	0.43
Glu	GAA	0.42	0.75	1.79
Phe	TTT	0.45	0.76	1.69
Phe	TTC	0.55	0.24	0.44
Gly	GGG	0.25	0.04	0.16
Gly	GGA	0.25	0.36	1.44
Gly	GGT	0.16	0.36	2.25
Gly	GGC	0.34	0.24	0.71
His	CAT	0.41	0.79	1.93
His	CAC	0.59	0.21	0.36
Ile	ATA	0.17	0.00	0.00
Ile	ATT	0.35	0.78	2.23
Ile	ATC	0.48	0.22	0.46
Lys	AAG	0.57	0.11	0.19
Lys	AAA	0.43	0.89	2.07
Leu	TTG	0.13	0.02	0.15
Leu	TTA	0.07	0.40	5.71
Leu	CTG	0.40	0.14	0.35
Leu	CTA	0.08	0.16	2.00
Leu	CTT	0.13	0.28	2.15
Leu	CTC	0.20	0.00	0.00
Met	ATG	1.00	1.00	1.00
Asn	AAT	0.46	0.37	0.80
Asn	AAC	0.54	0.63	1.17
Pro	CCG	0.11	0.25	2.27
Pro	CCA	0.27	0.39	1.44
Pro	CCT	0.28	0.36	1.29
Pro	CCC	0.33	0.00	0.00
Gln	CAG	0.74	0.64	0.86
Gln	CAA	0.26	0.36	1.38
Arg	AGG	0.20	0.00	0.00
Arg	AGA	0.20	0.00	0.00
Arg	CGG	0.21	0.00	0.00
Arg	CGA	0.11	0.15	1.36
Arg	CGT	0.08	0.50	6.25
Arg	CGC	0.19	0.35	1.84
Ser	AGT	0.15	0.32	2.13
Ser	AGC	0.24	0.37	1.54
Ser	TCG	0.06	0.05	0.83
Ser	TCA	0.15	0.21	1.40
Ser	TCT	0.18	0.00	0.00
Ser	TCC	0.22	0.05	0.23
Thr	ACG	0.11	0.43	3.91
Thr	ACA	0.28	0.43	1.54
Thr	ACT	0.24	0.13	0.54
Thr	ACC	0.36	0.00	0.00
Val	GTG	0.46	0.25	0.54
Val	GTA	0.12	0.33	2.75
Val	GTT	0.18	0.21	1.17
Val	GTC	0.24	0.21	0.88
Trp	TGG	1.00	1.00	1.00
Tyr	TAT	0.44	0.67	1.52
Tyr	TAC	0.56	0.33	0.59
End	TGA	0.54	0.00	0.00
End	TAG	0.20	0.00	0.00
End	TAA	0.26	1.00	3.85

Appendix B – Chemical aggregation of Ferritin

Before embarking on the development of genetically engineered sensors based on Ft, we confirmed that physical aggregation of Ft could produce T2 contrast changes in MRI. We used chemical crosslinking via the biotin-streptavidin interaction[i] to induce controlled aggregation of horse spleen ferritin (HSF) and monitored the resulting effects on T2 relaxivity in MRI. HSF (pre-loaded with ~2,000 iron atoms per particle, Sigma) was biotinylated at primary amino groups using sulpho-NHS-biotin (Pierce) and purified over a G-25 desalting column (GE). Protein concentration was measured by absorbance spectroscopy using a pre-determined titration curve at 400nm. Biotinylated ferritin was then incubated for 1hr with various ratios of streptavidin/ferritin to induce the formation of aggregates. Mean cluster size was then measured using dynamic light scattering (DLS), and samples were imaged in 384-well plates using a T2-weighted MRI pulse sequence. As is apparent from a representative T2-weighted image (Fig 1a), T2 relaxivity increases with greater aggregation, leading to greater signal reduction. The relationship between mean aggregate size and T2 relaxation rate is plotted in Figs 1b and 1c. A more than two-fold increase in relaxivity was observed for aggregates of ~150nm radius. All aggregates within this range of apparent sizes remained in solution during the timecourse of our experiments.

Figure 1`

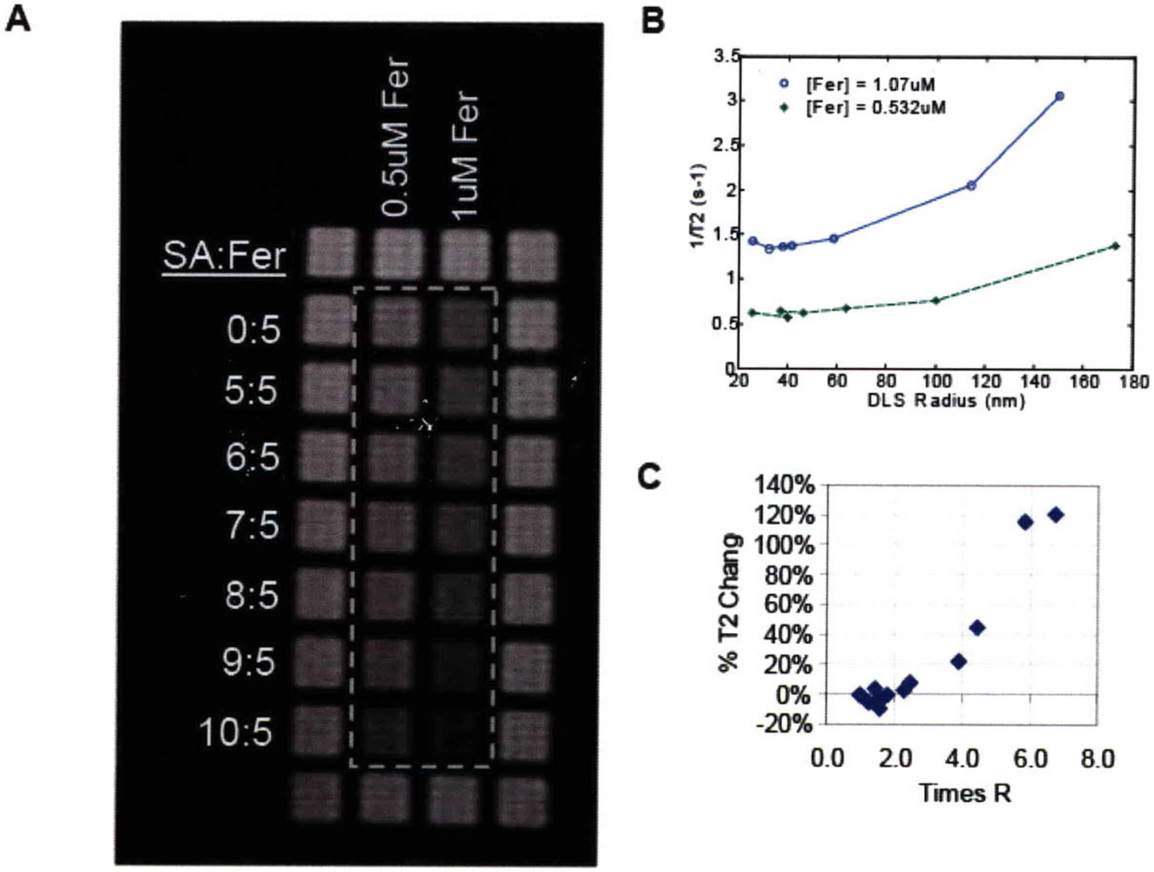

A
0.5uM Fer
1uM Fer
SA:Fer
0:5
5:5
6:5
7:5
8:5
9:5
10:5
B
[Fer] = 1.07uM
[Fer] = 0.532uM
1/T2 (s-1)
0
0.5
1
1.5
2
2.5
3
3.5
20
40
60
80
100
120
140
160
180
DLS Radius (nm)
C
140%
120%
100%
80%
60%
40%
20%
0%
-20%
% T2 Chang
0.0
2.0
4.0
6.0
8.0
Times R

Appendix C – Gene Sequences

This appendix lists the sequences for all of the genes used in Chapters 2 and 3 of this thesis. PCMV-Sport and pCWori, the vectors used for mammalian and bacterial expression, respectively, are also shown. Transcribed genes are in BOLD, with flanking sequences leading to the restriction sites used for vector cloning shown in normal typeface.

BM3h

GGATCCATCGATGCTTAGGAGGTCAT**ATGACAATTAAAGAAATGCCTCAGCCAAAAACGT**
TTGGAGAGCTTAAAAATTTACCGTTATTAAACACAGATAAACCGGTTCAAGCTTTGATGA
AAATTGCGGATGAATTAGGAGAAATCTTTAAATTCGAGGCGCCTGGTCGTGTAACGCGCT
ACTTATCAAGTCAGCGTCTAATTAAAGAAGCATGCGATGAATCACGCTTTGATAAAAACT
TAAGTCAAGCGCTTAAATTTGTACGTGATTTTGCAGGAGACGGGTTATTTACAAGCTGGA
CGCATGAAAAAAATTGGAAAAAAGCGCATAATATCTTACTTCCAAGCTTCAGTCAGCAGG
CAATGAAAGGCTATCATGCGATGATGGTCGATATCGCCGTGCAGCTTGTTCAAAAGTGGG
AGCGTCTAAATGCAGATGAGCATATTGAAGTACCGGAAGACATGACACGTTTAACGCTTG
ATACGATTGGTCTTTGCGGCTTTAACTATCGCTTTAACAGCTTTTACCGAGATCAGCCTC
ATCCATTTATTACAAGTATGGTCCGTGCACTGGATGAAGCAATGAACAAGCTGCAGCGAG
CAAATCCAGACGACCCAGCTTATGATGAAAACAAGCGCCAGTTTCAAGAAGATATCAAGG
TGATGAACGACCTAGTAGATAAAATTATTGCAGATCGCAAAGCAAGCGGTGAACAAAGCG
ATGATTTATTAACGCACATGCTAAACGGAAAAGATCCAGAAACGGGTGAGCCGCTTGATG
ACGAGAACATTCGCTATCAAATTATTACATTCTTAATTGCGGGACACGAAACAACAAGTG
GTCTTTTATCATTTGCGCTGTATTTCTTAGTGAAAAATCCACATGTATTACAAAAAGCAG
CAGAAGAAGCAGCACGAGTTCTAGTAGATCCTGTTCCAAGCTACAAACAAGTCAAACAGC
TTAAATATGTCGGCATGGTCTTAAACGAAGCGCTGCGCTTATGGCCAACTGCTCCTGCGT
TTTCCCTATATGCAAAAGAAGATACGGTGCTTGGAGGAGAATATCCTTTAGAAAAAGGCG
ACGAACTAATGGTTCTGATTCCTCAGCTTCACCGTGATAAAACAATTTGGGGAGACGATG
TGGAAGAGTTCCGTCCAGAGCGTTTTGAAAATCCAAGTGCGATTCCGCAGCATGCGTTTA
AACCGTTTGGAAACGGTCAGCGTGCGTGTATCGGTCAGCAGTTCGCTCTTCATGAAGCAA
CGCTGGTACTTGGTATGATGCTAAAACACTTTGACTTTGAAGATCATACAAACTACGAGC
TGGATATTAAAGAAACTTTAACGTTAAAACCTGAAGGCTTTGTGGTAAAAGCAAAATCGA
AAAAAATTCCGCTTGGCGGTATTCCTTCACCTAGCACTCATCATCATCATCATCATTAAT
GAATTC

BM3h-8C8

GGATCCATCGATGCTTAGGAGGTCAT**ATGACAATTAAAGAAATGCCTCAGCCAAAAACGTTTGGAGA**
GCTTAAAAATTTACCGTTATTAAACACAGATAAACCGGTTCAAGCTTTGATGAAAATTGCGGATGA
ATTAGGAGAAATCTTTAAATTCGAGGCGCCTGGTCGTGTAACGCGCTACTTATCAAGTCAGCGTCT
AATTAAAGAAGCATGCGATGAATCACGCTTTGATAAAAACTTAAGTCAAGCGCCTAAATTTGTACG
TGATTTTGCAGGAGACGGGTTATTTACAAGCTGGACGCATGAAAAAAATTGGAAAAAAGCG
CATAATATCTTACTTCCAAGCTTCAGTCAGCAGGCAATGAAAGGCTATCATGCGATGATG
GTCGATATCGCCGTGCAGCTTGTTCAAAAGTGGGAGCGTCTAAATGCAGACGAGCATATT
GAAGTACCGGAAGACATGACACGTTTAACGCTTGATACGATTGGTCTTTGCGGCTTTAAC

TATCGCTTTAACAGCTTTTACCGAGATCAGCCTCATCCATTTATTACAAGTATGGTCCGT
GCACTGGATGAAGCAATGAACAAGCTGCGGCGAGCAAATCCAGACGACCCAGCTTATGAT
GAAAACAAGCGCCAGTTTCAAGAAGATATCAAGGTGATGAACGACCTAGTAGATAAAATT
ATTGCAGATCGCAAAGCAAGCGGTGAACAAAGCGATGATTTATTAACGCACATGCTAAAC
GGAAAAGATCCAGAAACGGGTGAGCCGCTTGATGACGAGAACATTCGCTATCAAATTATT
ACATTCTTAGCTGCGGGACACGAAGCAACAAGTGGTCTTTTATCATTTGCGCTGTATTTC
TTAGTGAAAAATCCACATGAATTACAAAAAGCAGCAGAAGAAGCAGCACGAGTTCTAGTA
GATCCTGTTCCAAGCTACAAACAAGTCAAACAGCTTAAATATGTCGGCATGGTCTTAAAC
GAAGCGCTGCGCTTATGGCCAACTGCTCCTGCGTTTTCCCTATATGCAAAAGAAGATACG
GTGCTTGGAGGAGAATATCCTTTAGAAAAAGGCGACGAACTAATGGTTCTGATTCCTCAG
CTTCACCGTGATAAAACAATTTGGGGAGACGATGTGGAAGAGTTCCGTCCAGAGCGTTTT
GAAAATCCAAGTGCGATTCCGCAGCATGCGTTTAAACCGTTTGGAAACGGTCAGCGTGCG
TGTATCGGTCAGCAGTTCGCTCTTCATGAAGCAACGCTGGTACTTGGTATGATGCTAAAA
CACTTTGACTTTGAAGATCATACAAACTACGAGCTGGATATTAAAGAAACTTTAACGTTA
AAACCTGAAGGCTTTGTGGTAAAAGCAAAATCGAAAAAAATTCCGCTTGGCGGTATTCCT
TCACCTAGCACTCATCATCATCATCATTATTAATGAATTC

BM3h-B7

GGATCCATCGATGCTTAGGAGGTCAT**ATGACAATTAAAGAAATGCCTCAGCCAAAAACGTTTGGAGA**
GCTTAAAAATTTACCGTTATTAAACACAGATAAACCGGTTCAAGCTTTGATGAAAATTGCGGATGA
ATTAGGAGAAATCTTTAAATTCGAGGCGCCTGGTCGTGTAACGCGCTACTTATCAAGTCAGCGTCT
AATTAAAGAAGCATGCGATGAATCACGCTTTGATAAAAACTTAAGTCAAGCGCCTAAATTTGTACG
TGATCTTGCAGGAGACGGGTTATTTACAAGCTGGACGCATGAAAAAAATTGGAAAAAAGCGCATAA
TATCTTACTTCCAAGCTTCAGTCAGCAGGCAATGAAAGGCTATCATGCGATGATGGTCGATATCGC
CGTGCAGCTTGTTCAAAAGTGGGAGCGTCTAAATGCAGACGAGCATATTGAAGTACCGGAAGACAT
GACACGTTTAACGCTTGATACGATTGGTCTTTGCGGCTTTAACTATCGCTTTAACAGCTTTTACCGA
GATCAGCCTCATCCATTTATTACAAGTATGGTCCGTGCACTGGATGAAGCAATGAACAAGCTGCGG
CGAGCAAATCCAGACGACCCAGCTTATGATGAAAACAAGCGCCAGTTTCAAGAAGATATCAAGGTG
ATGAACGACCTAGTAGATAAAATTATTGCAGATCGCAAAGCAAGCGGTGAACAAAGCGATGATTTA
TTAACGCACATGCTAAACGGAAAAGATCCAGAAACGGGTGAGCCGCTTGATGACGAGAACATTCG
CTATCAAATTATTACATTCTTAGCTGCGGGACACGAAGCAACAAGTGGTCTTTTATCATTTGCGCTG
TATTTCTTAGTGAAAAATCCACATGAATTACAAAAAGCAGCAGAAGAAGCAGCACGAGTTCTAGTA
GATCCTGTTCCAAGCCACAAACAAGTCAAACAGCTTAAATATGTCGGCATGGTCTTAAACGAAGCG
CTGCGCTTATGGCCAACTGCTCCTGCGTTTTCCCTATATGCAAAAGAAGATACGGTGCTTGGAGGA
GAATATCCTTTAGAAAAAGGCGACGAACTAATGGTTCTGATTCCTCAGCTTCACCGTGATAAAACA
GTTTGGGGAGACGATGTGGAAGAGTTCCGTCCAGAGCGTTTTGAAAATCCAAGTGCGATTCCGCA
GCATGCGTTTAAACCGTTTGGAAACGGTCAGCGTGCGTGTATCGGTCAGCAGTTCGCTCTTCATGA
AGCAACGCTGGTACTTGGTATGATGCTAAAACACTTTGACTTTGAAGATCATACAAACTACGAGCT
GGATATTAAAGAAACTTTAACGTTAAAACCTGAAGGCTTTGTGGTAAAAGCAAAATCGAAAAAAAT
TCCGCTTGGCGGTATTCCTTCACCTAGCACTCATCATCATCATCATCATTAATGAATTC

Mammalian codon optimized BM3h

GGTACCACC**ATGACAATCAAGGAGATGCCTCAGCCTAAAACATTCGGCGAACTGAAGAATCTGCC**
GCTTTTGAACACTGACAAACCCGTACAGGCCCTTATGAAGATAGCCGATGAATTGGGTGA
AATTTTTAAGTTTGAGGCGCCCGGGCGCGTAACCAGATATTTGTCCAGTCAGAGGTTGAT
CAAAGAGGCCTGCGATGAGTCTCGCTTTGATAAAAACTTGTCACAGGCACTGAAGTTTGT
CAGAGATTTTGCCGGAGATGGCTTGTTTACGTCCTGGACCCACGAAAAAAACTGGAAGAA
AGCTCATAACATCCTGCTGCCTTCCTTCTCACAACAGGCCATGAAAGGCTACCATGCAAT
GATGGTGGACATCGCGGTCCAGCTGGTGCAGAAATGGGAGAGACTGAATGCCGATGAGCA
CATTGAAGTCCCGGAGGATATGACTCGGCTCACGCTGGATACAATCGGACTGTGTGGCTT
CAATTACCGATTTAACTCATTTTATCGGGATCAGCCTCACCCATTTATCACAAGTATGGT
GAGAGCACTTGACGAGGCAATGAATAAACTGCAGCGCGCTAATCCAGATGATCCGGCATA
TGACGAAAACAAAAGGCAGTTTCAAGAGGACATTAAGGTGATGAACGACTTGGTGGACAA
GATCATCGCAGATCGGAAGGCCTCAGGCGAGCAGTCTGATGATCTCTTGACCCATATGCT
GAATGGGAAAGACCCAGAGACCGGTGAGCCATTGGACGACGAGAATATCAGGTATCAGAT
TATAACTTTTCTGATCGCCGGACACGAGACAACTTCAGGCCTGCTCTCTTTCGCCCTGTA
CTTCCTGGTTAAAAATCCACACGTGCTCCAGAAGGCTGCAGAAGAAGCTGCCAGAGTGCT
TGTAGACCCTGTGCCCTCCTATAAACAAGTGAAGCAGCTTAAGTATGTGGGGATGGTCCT

TAATGAGGCACTGCGACTGTGGCCAACTGCGCCCGCCTTCTCTCTGTACGCCAAGGAGGA
TACCGTTCTGGGCGGGGAATATCCTTTGGAGAAAGGCGATGAGCTCATGGTGCTGATCCC
TCAGCTCCATAGAGACAAGACAATTTGGGGCGACGACGTGGAGGAATTCCGGCCTGAACG
GTTTGAGAACCCCTCTGCAATACCACAACACGCGTTTAAACCCTTCGGCAACGGACAGCG
CGCCTGTATAGGCCAACAGTTCGCCCTGCACGAGGCTACCCTCGTGCTCGGTATGATGCT
GAAGCATTTTGACTTTGAGGACCACACAAATTACGAGCTCGACATCAAAGAGACTCTGAC
ACTGAAGCCGGAAGGCTTTGTGGTAAAAGCTAAAAGCAAGAAGATCCCACTGGGAGGAAT
TCCTAGCCCATCTACTCACCACCATCACCACCATTGATCTAGA

Mammalian codon optimized BM3h-8C8

GGTACCACC**ATGACAATCAAGGAGATGCCTCAGCCTAAAACATTCGGCGAACTGAAGAATCTGCCG**
CTTTTGAACACTGACAAACCCGTACAGGCCCTTATGAAGATAGCCGATGAATTGGGTGAAATT
TTTAAGTTTGAGGCGCCCGGGCGCGTAACCAGATATTTGTCCAGTCAGAGGTTGATCAAA
GAGGCCTGCGATGAGTCTCGCTTTGATAAAAACTTGTCACAGGCACCGAAGTTTGTCAGA
GATTTTGCCGGAGATGGCTTGTTTACGTCCTGGACCCACGAAAAAAACTGGAAGAAAGCT
CATAACATCCTGCTGCCTTCCTTCTCACAACAGGCCATGAAAGGCTACCATGCAATGATG
GTGGACATCGCGGTCCAGCTGGTGCAGAAATGGGAGAGACTGAATGCCGATGAGCACATT
GAAGTCCCGGAGGATATGACTCGGCTCACGCTGGATACAATCGGACTGTGTGGCTTCAAT
TACCGATTTAACTCATTTTATCGGGATCAGCCTCACCCATTTATCACAAGTATGGTGAGA
GCACTTGACGAGGCAATGAATAAACTGCGGCGCGCTAATCCAGATGATCCGGCATATGAC
GAAAACAAAAGGCAGTTTCAAGAGGACATTAAGGTGATGAACGACTTGGTGGACAAGATC
ATCGCAGATCGGAAGGCCTCAGGCGAGCAGTCTGATGATCTCTTGACCCATATGCTGAAT
GGGAAAGACCCAGAGACCGGTGAGCCATTGGACGACGAGAATATCAGGTATCAGATTATA
ACTTTTCTGGCCGCCGGACACGAGGCAACTTCAGGCCTGCTCTCTTTCGCCCTGTACTTC
CTGGTTAAAAATCCACACGAGCTCCAGAAGGCTGCAGAAGAAGCTGCCAGAGTGCTTGTA
GACCCTGTGCCCTCCTATAAACAAGTGAAGCAGCTTAAGTATGTGGGGATGGTCCTTAAT
GAGGCACTGCGACTGTGGCCAACTGCGCCCGCCTTCTCTCTGTACGCCAAGGAGGATACC
GTTCTGGGCGGGGAATATCCTTTGGAGAAAGGCGATGAGCTCATGGTGCTGATCCCTCAG
CTCCATAGAGACAAGACAATTTGGGGCGACGACGTGGAGGAATTCCGGCCTGAACGGTTT
GAGAACCCCTCTGCAATACCACAACACGCGTTTAAACCCTTCGGCAACGGACAGCGCGCC
TGTATAGGCCAACAGTTCGCCCTGCACGAGGCTACCCTCGTGCTCGGTATGATGCTGAAG
CATTTTGACTTTGAGGACCACACAAATTACGAGCTCGACATCAAAGAGACTCTGACACTG
AAGCCGGAAGGCTTTGTGGTAAAAGCTAAAAGCAAGAAGATCCCACTGGGAGGAATTCCT
AGCCCATCTACTCACCACCATCACCACCATTGATCTAGA

HF

GGTACCGAGCTCGGATCCAGTACCCTTCACCATG**GAATTCATGACGACCGCGTCCACCTCGCAGGTGC**
GCCAGAACTACCACCAGGACTCAGAGGCCGCCATCAACCGCCAGATCAACCTGGAGCTCTACGCC
TCCTACGTTTACCTGTCCATGTCTTACTACTTTGACCGCGATGATGTGGCTTTGAAGAACTTTGCCA
AATACTTTCTTCACCAATCTCATGAGGAGAGGGAACATGCTGAGAAACTGATGAAGCTGCAGAACC
AACGAGGTGGCCGAATCTTCCTTCAGGATATCAAGAAACCAGACTGTGATGACTGGGAGAGCGGG
CTGAATGCAATGGAGTGTGCATTACATTTGGAAAAAAATGTGAATCAGTCACTACTGGAACTGCAC
AAACTGGCCACTGACAAAAATGACCCCCATTTGTGTGACTTCATTGAGACACATTACCTGAATGAG
CAGGTGAAAGCCATCAAAGAATTGGGTGACCACGTGACCAACTTGCGCAAGATGGGAGCGCCCGA
ATCTGGCTTGGCGGAATATCTCTTTGACAAGCACACCCTGGGAGACAGTGATAATGAAAGCTAA
AAGGGTCAAGACAATTCTGCAGA TATCCAGCACAGTGGCGGCC GCTCGAGTCTAGA

LF

GGTACCGAGCTCGGATCCAGTACCCTTCACCATG**GAATTCATGAGCTCCCAGATTCGTCAGAATTATT**
CCACCGACGTGGAGGCAGCCGTCAACAGCCTGGTCAATTTGTACCTGCAGGCCTCCTACACCTACC
TCTCTCTGGGCTTCTATTTCGACCGCGATGATGTGGCTCTGGAAGGCGTGAGCCACTTCTTCCGCG
AATTGGCCGAGGAGAAGCGCGAGGGCTACGAGCGTCTCCTGAAGATGCAAAACCAGCGTGGCGGC
CGCGCTCTCTTCCAGGACATCAAGAAGCCAGCTGAAGATGAGTGGGGTAAAACCCCAGACGCCAT

GAAAGCTGCCATGGCCCTGGAGAAAAAGCTGAACCAGGCCCTTTTGGATCTTCATGCCCTGGGTTC
TGCCCGCACGGACCCCCATCTCTGTGACTTCCTGGAGACTCACTTCCTAGATGAGGAAGTGAAG
CTTATCAAGAAGATGGGTGACCACCTGACCAACCTCCACAGGCTGGGTGGCCCGGAGGCT
GGGCTGGGCGAGTATCTCTTCGAAAGGCTCACTCTCAAGCACGACTAA AGGGTCAAGAC
AATTCTGC AGATATCCAGCACAGTGGCGGCC GCTCGAGTCTAGA

FLAG-LF

GGTACCGAGCTCGGATCCACC**ATGGACTACAAAGACCATGACGGTGATTATAAAGATCATGACAT**
CGATTACAAGGATGACGATGACAAGGGAACCAGCAGCGAATTCATGAGCTCCCAGATTCG
TCAGAATTATTCCACCGACGTGGAGGCAGCCGTCAACAGCCTGGTCAATTTGTACCTGCA
GGCCTCCTACACCTACCTCTCTCTGGGCTTCTATTTCGACCGCGATGATGTGGCTCTGGA
AGGCGTGAGCCACTTCTTCCGCGAATTGGCCGAGGAGAAGCGCGAGGGCTACGAGCGTCT
CCTGAAGATGCAAAACCAGCGTGGCGGCCGCGCTCTCTTCCAGGACATCAAGAAGCCAGC
TGAAGATGAGTGGGGTAAAACCCCAGACGCCATGAAAGCTGCCATGGCCCTGGAGAAAAA
GCTGAACCAGGCCCTTTTGGATCTTCATGCCCTGGGTTCTGCCCGCACGGACCCCCATCT
CTGTGACTTCCTGGAGACTCACTTCCTAGATGAGGAAGTGAAGCTTATCAAGAAGATGGG
TGACCACCTGACCAACCTCCACAGGCTGGGTGGCCCGGAGGCTGGGCTGGGCGAGTATCT
CTTCGAAAGGCTCACTCTCAAGCACGACTAA AGGGTCAAGAC AATTCTGC
AGATATCCAGCACAGTGGCGGCC GCTCGAGTCTAGA

KID-LF

GGTACCGAGCTCGGATCCACC**ATGGGTTCTTCCTGTAAGGACTTAAAAAGACTTTTCTCCGGAACTC**
AGATTTCAACTATTGCAGAAAGTGAAGATTCACAGGAGTCTGTGGATAGTGTAACTGATTCCCAAA
AACGAAGGGAAATCCTTTCAAGGAGGCCTTCCTACAGGAAAATTTTGAATGACTTATCTTCTGATG
CACCAGGGGTGCCAAGGATTGAAGAAGAAAAATCAGAAGAAGAGACTGGAACCAGCAGCGAA
TTCATGAGCTCCCAGATTCGTCAGAATTATTCCACCGACGTGGAGGCAGCCGTCAACAGC
CTGGTCAATTTGTACCTGCAGGCCTCCTACACCTACCTCTCTCTGGGCTTCTATTTCGAC
CGCGATGATGTGGCTCTGGAAGGCGTGAGCCACTTCTTCCGCGAATTGGCCGAGGAGAAG
CGCGAGGGCTACGAGCGTCTCCTGAAGATGCAAAACCAGCGTGGCGGCCGCGCTCTCTTC
CAGGACATCAAGAAGCCAGCTGAAGATGAGTGGGGTAAAACCCCAGACGCCATGAAAGCT
GCCATGGCCCTGGAGAAAAAGCTGAACCAGGCCCTTTTGGATCTTCATGCCCTGGGTTCT
GCCCGCACGGACCCCCATCTCTGTGACTTCCTGGAGACTCACTTCCTAGATGAGGAAGTG
AAGCTTATCAAGAAGATGGGTGACCACCTGACCAACCTCCACAGGCTGGGTGGCCCGGAG
GCTGGGCTGGGCGAGTATCTCTTCGAAAGGCTCACTCTCAAGCACGACTAA AGGGTCAAGAC
AATTCTGC AGATATCCAGCACAGTGGCGGCC GCTCGAGTCTAGA

KIX-LF

GGTACCGAGCTCGGATCCACC**TGAGCACGATACCTACAGCAGCGCCTCCTTCCAGCACTGGTGTTCG**
AAAAGGCTGGCATGAACATGTGACTCAGGACCTACGGAGTCATCTAGTCCATAAACTCGTTCAAGC
CATCTTCCCAACTCCAGACCCTGCAGCTCTGAAAGATCGCCGCATGGAGAACCTGGTTGCCTATGC
TAAGAAAGTGGAGGGAGACATGTATGAGTCTGCTAATAGCAGGGATGAATACTATCATTTA
TTAGCAGAGAAAATCTATAAAATACAAAAAGAACTAGAAGAAAAGCGGAGGTCACGTTTA
CATAAGCAAGGCATCCTGGGTAACCAGCCAGCTTTACCAGCGGGAACCAGCAGCGAATTC
ATGAGCTCCCAGATTCGTCAGAATTATTCCACCGACGTGGAGGCAGCCGTCAACAGCCTG
GTCAATTTGTACCTGCAGGCCTCCTACACCTACCTCTCTCTGGGCTTCTATTTCGACCGC
GATGATGTGGCTCTGGAAGGCGTGAGCCACTTCTTCCGCGAATTGGCCGAGGAGAAGCGC
GAGGGCTACGAGCGTCTCCTGAAGATGCAAAACCAGCGTGGCGGCCGCGCTCTCTTCCAG
GACATCAAGAAGCCAGCTGAAGATGAGTGGGGTAAAACCCCAGACGCCATGAAAGCTGCC
ATGGCCCTGGAGAAAAAGCTGAACCAGGCCCTTTTGGATCTTCATGCCCTGGGTTCTGCC
CGCACGGACCCCCATCTCTGTGACTTCCTGGAGACTCACTTCCTAGATGAGGAAGTGAAG
CTTATCAAGAAGATGGGTGACCACCTGACCAACCTCCACAGGCTGGGTGGCCCGGAGGCT
GGGCTGGGCGAGTATCTCTTCGAAAGGCTCACTCTCAAGCACGACTAA AGGGTCAAGAC
AATTCTGC AGATATCCAGCACAGTGGCGGCC GCTCGAGTCTAGA

Vector: pCWori

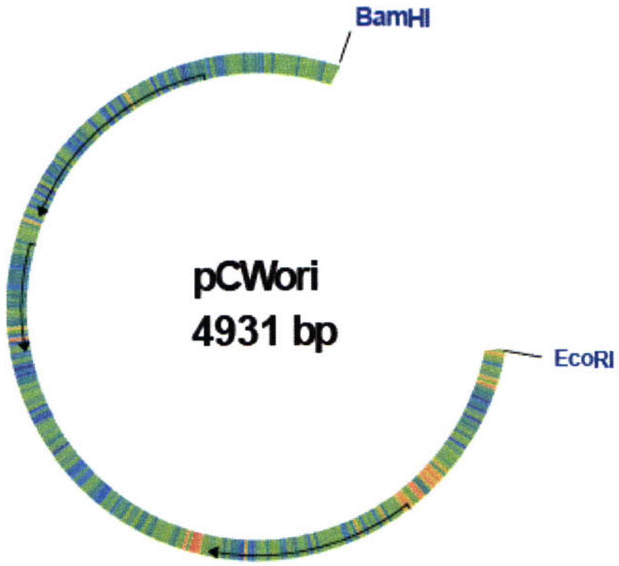

```
GAATTCATCGATGATAAGCTGTCAAACATGAGCAGATCTGAGCCCGCCTAATGAGCGGGC
TTTTTTTTCAGATCTGCTTGAAGACGAAAGGGCCTCGTGATACGCCTATTTTTATAGGTT
AATGTCATGATAATAATGGTTTCTTAGCGTCAAAGCAACCATAGTACGCGCCCTGTAGCG
GCGCATTAAGCGCGGCGGGTGTGGTGGTTACGCGCAGCGTGACCGCTACACTTGCCAGCG
CCCTAGCGCCCGCTCCTTTCGCTTTCTTCCCTTCCTTTCTCGCCACGTTCGCCGGCTTTC
CCCGTCAAGCTCTAAATCGGGGGCTCCCTTTAGGGTTCCGATTTAGTGCTTTACGGCACC
TCGACCCCAAAAAACTTGATTTGGGTGATGGTTCACGTAGTGGGCCATCGCCCTGATAGA
CGGTTTTTCGCCCTTTGACGTTGGAGTCCACGTTCTTTAATAGTGGACTCTTGTTCCAAA
CTGGAACAACACTCAACCCTATCTCGGGCTATTCTTTTGATTTATAAGGGATTTTGCCGA
TTTCGGCCTATTGGTTAAAAAATGAGCTGATTTAACAAAAATTTAACGCGAATTTTAACA
AAATATTAACGTTTACAATTTCAGGTGGCACTTTTCGGGGAAATGTGCGCGGAACCCCTA
TTTGTTTATTTTTCTAAATACATTCAAATATGTATCCGCTCATGAGACAATAACCCTGAT
AAATGCTTCAATAATATTGAAAAAGGAAGAGTATGAGTATTCAACATTTCCGTGTCGCCC
TTATTCCCTTTTTTGCGGCATTTTGCCTTCCTGTTTTTGCTCACCCAGAAACGCTGGTGA
AAGTAAAAGATGCTGAAGATCAGTTGGGTGCACGAGTGGGTTACATCGAACTGGATCTCA
ACAGCGGTAAGATCCTTGAGAGTTTTCGCCCCGAAGAACGTTTTCCAATGATGAGCACTT
TTAAAGTTCTGCTATGTGGCGCGGTATTATCCCGTGTTGACGCCGGGCAAGAGCAACTCG
GTCGCCGCATACACTATTCTCAGAATGACTTGGTTGAGTACTCACCAGTCACAGAAAAGC
ATCTTACGGATGGCATGACAGTAAGAGAATTATGCAGTGCTGCCATAACCATGAGTGATA
ACACTGCGGCCAACTTACTTCTGACAACGATCGGAGGACCGAAGGAGCTAACCGCTTTTT
TGCACAACATGGGGGATCATGTAACTCGCCTTGATCGTTGGGAACCGGAGCTGAATGAAG
CCATACCAAACGACGAGCGTGACACCACGATGCCTGCAGCAATGGCAACAACGTTGCGCA
AACTATTAACTGGCGAACTACTTACTCTAGCTTCCCGGCAACAATTAATAGACTGGATGG
AGGCGGATAAAGTTGCAGGACCACTTCTGCGCTCGGCCCTTCCGGCTGGCTGGTTTATTG
CTGATAAATCTGGAGCCGGTGAGCGTGGGTCTCGCGGTATCATTGCAGCACTGGGGCCAG
ATGGTAAGCCCTCCCGTATCGTAGTTATCTACACGACGGGGAGTCAGGCAACTATGGATG
AACGAAATAGACAGATCGCTGAGATAGGTGCCTCACTGATTAAGCATTGGTAACTGTCAG
ACCAAGTTTACTCATATATACTTTAGATTGATTTAAAACTTCATTTTTAATTTAAAAGGA
TCTAGGTGAAGATCCTTTTTGATAATCTCATGACCAAAATCCCTTAACGTGAGTTTTCGT
TCCACTGAGCGTCAGACCCCGTAGAAAAGATCAAAGGATCTTCTTGAGATCCTTTTTTTC
TGCGCGTAATCTGCTGCTTGCAAACAAAAAAACCACCGCTACCAGCGGTGGTTTGTTTGC
CGGATCAAGAGCTACCAACTCTTTTTCCGAAGGTAACTGGCTTCAGCAGAGCGCAGATAC
CAAATACTGTCCTTCTAGTGTAGCCGTAGTTAGGCCACCACTTCAAGAACTCTGTAGCAC
CGCCTACATACCTCGCTCTGCTAATCCTGTTACCAGTGGCTGCTGCCAGTGGCGATAAGT
CGTGTCTTACCGGGTTGGACTCAAGACGATAGTTACCGGATAAGGCGCAGCGGTCGGGCT
```

GAACGGGGGGTTCGTGCACACAGCCCAGCTTGGAGCGAACGACCTACACCGAACTGAGAT
ACCTACAGCGTGAGCTATGAGAAAGCGCCACGCTTCCCGAAGGGAGAAAGGCGGACAGGT
ATCCGGTAAGCGGCAGGGTCGGAACAGGAGAGCGCACGAGGGAGCTTCCAGGGGGAAACG
CCTGGTATCTTTATAGTCCTGTCGGGTTTCGCCACCTCTGACTTGAGCGTCGATTTTTGT
GATGCTCGTCAGGGGGGCGGAGCCTATGGAAAAACGCCAGCAACGCGGCCTTTTTACGGT
TCCTGGCCTTTTGCTGGCCTTTTGCTCACATGTTCTTTCCTGCGTTATCCCCTGATTCTG
TGGATAACCGTATTACCGCCTTTGAGTGAGCTGATACCGCTCGCCGCAGCCGAACGACCG
AGCGCAGCGAGTCAGTGAGCGAGGAAGCGGAAGAGCGCCTGATGCGGTATTTTCTCCTTA
CGCATCTGTGCGGTATTTCACACCGCATATATGGTGCACTCTCAGTACAATCTGCTCTGA
TGCCGCATAGTTAAGCCAGTATACACTCCGCTATCGCTACGTGACTGGGTCATGGCTGCG
CCCCGACACCCGCCAACACCCGCTGACGCGCCCTGACGGGCTTGTCTGCTCCCGGCATCC
GCTTACAGACAAGCTGTGACCGTCTCCGGGAGCTGCATGTGTCAGAGGTTTTCACCGTCA
TCACCGAAACGCGCGAGGCAGAACGCCATCAAAAATAATTCGCGTCTGGCCTTCCTGTAG
CCAGCTTTCATCAACATTAAATGTGAGCGAGTAACAACCCGTCGGATTCTCCGTGGGAAC
AAACGGCGGATTGACCGTAATGGGATAGGTTACGTTGGTGTAGATGGGCGCATCGTAACC
GTGCATCTGCCAGTTTGAGGGGACGACGACAGTATCGGCCTCAGGAAGATCGCACTCCAG
CCAGCTTTCCGGCACCGCTTCTGGTGCCGGAAACCAGGCAAAGCGCCATTCGCCATTCAG
GCTGCGCAACTGTTGGGAAGGGCGATCGGTGCGGGCCTCTTCGCTATTACGCCAGCTGGC
GAAAGGGGGATGTGCTGCAAGGCGATTAAGTTGGGTAACGCCAGGGTTTTCCCAGTCACG
ACGTTGTAAAACGACGGCCAGTGAATCCGTAATCATGGTCATAGCTGTTTCCTGTGTGAA
ATTGTTATCCGCTCACAATTCCACACAACATACGAGCCGGAAGCATAAAGTGTAAAGCCT
GGGGTGCCTAATGAGTGAGCTAACTCACATTAATTGCGTTGCGCTCACTGCCCGCTTTCC
AGTCGGGAAACCTGTCGTGCCAGCTGCATTAATGAATCGGCCAACGCGCGGGGAGAGGCG
GTTTGCGTATTGGGCGCCAGGGTGGTTTTTCTTTTCACCAGTGAGACGGGCAACAGCTGA
TTGCCCTTCACCGCCTGGCCCTGAGAGAGTTGCAGCAAGCGGTCCACGCTGGTTTGCCCC
AGCAGGCGAAAATCCTGTTTGATGGTGGTTAACGGCGGGATATAACATGAGCTGTCTTCG
GTATCGTCGTATCCCACTACCGAGATATCCGCACCAACGCGCAGCCCGGACTCGGTAATG
GCGCGCATTGCGCCCAGCGCCATCTGATCGTTGGCAACCAGCATCGCAGTGGGAACGATG
CCCTCATTCAGCATTTGCATGGTTTGTTGAAAACCGGACATGGCACTCCAGTCGCCTTCC
CGTTCCGCTATCGGCTGAATTTGATTGCGAGTGAGATATTTATGCCAGCCAGCCAGACGC
AGACGCGCCGAGACAGAACTTAATGGGCCCGCTAACAGCGCGATTTGCTGGTGACCCAAT
GCGACCAGATGCTCCACGCCCAGTCGCGTACCGTCTTCATGGGAGAAAATAATACTGTTG
ATGGGTGTCTGGTCAGAGACATCAAGAAATAACGCCGGAACATTAGTGCAGGCAGCTTCC
ACAGCAATGGCATCCTGGTCATCCAGCGGATAGTTAATGATCAGCCCACTGACGCGTTGC
GCGAGAAGATTGTGCACCGCCGCTTTACAGGCTTCGACGCCGCTTCGTTCTACCATCGAC
ACCACCACGCTGGCACCCAGTTGATCGGCGCGAGATTTAATCGCCGCGACAATTTGCGAC
GGCGCGTGCAGGGCCAGACTGGAGGTGGCAACGCCAATCAGCAACGACTGTTTGCCCGCC
AGTTGTTGTGCCACGCGGTTGGGAATGTAATTCAGCTCCGCCATCGCCGCTTCCACTTTT
TCCCGCGTTTTCGCAGAAACGTGGCTGGCCTGGTTCACCACGCGGGAAACGGTCTGATAA
GAGACACCGGCATACTCTGCGACATCGTATAACGTTACTGGTTTCACATTCACCACCCTG
AATTGACTCTCTTCCGGGCGCTATCATGCCATACCGCGAAAGGTTTTGCGCCATTCGATG
GTGTCCTGGCACGACAGGTTTCCCGACTGGAAAGCGGGCAGTGAGCGCAACGCAATTAAT
GTGAGTTAGCTCACTCATTAGGCACCCCAGGCTTTACACTTTATGCTTCCGGCTCGTATA
ATGTGTGGAATTGTGAGCGGATAACAATTTCACACAGGAAACAGGATCGATCCATCGATG
AGCTTACTCCCCATCCCCCTGTTGACAATTAATCATCGGCTCGTATAATGTGTGGAATTG
TGAGCGGATAACAATTTCACACAGGAAACAGGATCAGCTTACTCCCCATCCCCCTGTTGA
CAATTAATCATCGGCTCGTATAATGTGTGGAATTGTGAGCGGATAACAATTTCACACAGG
AAACAGGATCC

Vector: pCMV-SPORT

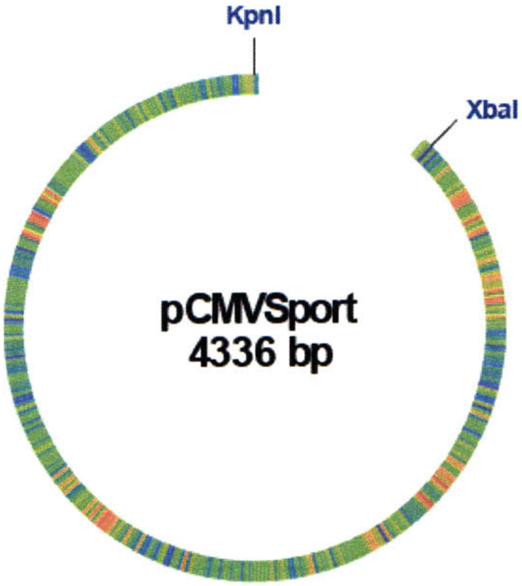

```
TCTAGAGGATCCCTCGAGGGGCCCAAGCTTACGCGTGCATGCGACGTCATAGCTCTCTCC
CTATAGTGAGTCGTATTATAAGCTAGCTTGGGATCTTTGTGAAGGAACCTTACTTCTGTG
GTGTGACATAATTGGACAAACTACCTACAGAGATTTAAAGCTCTAAGGTAAATATAAAAT
TTTTAAGTGTATAATGTGTTAAACTAGCTGCATATGCTTGCTGCTTGAGAGTTTTGCTTA
CTGAGTATGATTTATGAAAATATTATACACAGGAGCTAGTGATTCTAATTGTTTGTGTAT
TTTAGATTCACAGTCCCAAGGCTCATTTCAGGCCCCTCAGTCCTCACAGTCTGTTCATGA
TCATAATCAGCCATACCACATTTGTAGAGGTTTTACTTGCTTTAAAAAACCTCCCACACC
TCCCCCTGAACCTGAAACATAAAATGAATGCAATTGTTGTTGTTAACTTGTTTATTGCAG
CTTATAATGGTTACAAATAAAGCAATAGCATCACAAATTTCACAAATAAAGCATTTTTTT
CACTGCATTCTAGTTGTGGTTTGTCCAAACTCATCAATGTATCTTATCATGTCTGGATCG
ATCCTGCATTAATGAATCGGCCAACGCGCGGGGAGAGGCGGTTTGCGTATTGGCTGGCGT
AATAGCGAAGAGGCCCGCACCGATCGCCCTTCCCAACAGTTGCGCAGCCTGAATGGCGAA
TGGACGCGCCCTGTAGCGGCGCATTAAGCGCGGCGGGTGTGGTGGTTACGCGCAGCGTGA
CCGCTACACTTGCCAGCGCCCTAGCGCCCGCTCCTTTCGCTTTCTTCCCTTCCTTTCTCG
CCACGTTCGCCGGCTTTCCCCGTCAAGCTCTAAATCGGGGGCTCCCTTTAGGGTTCCGAT
TTAGTGCTTTACGGCACCTCGACCCCAAAAAACTTGATTAGGGTGATGGTTCACGTAGTG
GGCCATCGCCCTGATAGACGGTTTTTCGCCCTTTGACGTTGGAGTCCACGTTCTTTAATA
GTGGACTCTTGTTCCAAACTGGAACAACACTCAACCCTATCTCGGTCTATTCTTTTGATT
TATAAGGGATTTTGCCGATTTCGGCCTATTGGTTAAAAAATGAGCTGATTTAACAAAAAT
TTAACGCGAATTTTAACAAAATATTAACGTTTACAATTTCAGGTGGCACTTTTCGGGGAA
ATGTGCGCGGAACCCCTATTTGTTTATTTTTCTAAATACATTCAAATATGTATCCGCTCA
TGCCAGGTCTTGGACTGGTGAGAACGGCTTGCTCGGCAGCTTCGATGTGTGCTGGAGGGA
GAATAAAGGTCTAAGATGTGCGATAGAGGGAAGTCGCATTGAATTATGTGCTGTGTAGGG
ATCGCTGGTATCAAATATGTGTGCCCACCCCTGGCATGAGACAATAACCCTGATAAATGC
TTCAATAATATTGAAAAAGGAAGAGTATGAGTATTCAACATTTCCGTGTCGCCCTTATTC
CCTTTTTTGCGGCATTTTGCCTTCCTGTTTTTGCTCACCCAGAAACGCTGGTGAAAGTAA
AAGATGCTGAAGATCAGTTGGGTGCACGAGTGGGTTACATCGAACTGGATCTCAACAGCG
GTAAGATCCTTGAGAGTTTTCGCCCCGAAGAACGTTTTCCAATGATGAGCACTTTTAAAG
TTCTGCTATGTGGCGCGGTATTATCCCGTATTGACGCCGGGCAAGAGCAACTCGGTCGCC
GCATACACTATTCTCAGAATGACTTGGTTGAGTACTCACCAGTCACAGAAAAGCATCTTA
CGGATGGCATGACAGTAAGAGAATTATGCAGTGCTGCCATAACCATGAGTGATAACACTG
CGGCCAACTTACTTCTGACAACGATCGGAGGACCGAAGGAGCTAACCGCTTTTTTGCACA
ACATGGGGGATCATGTAACTCGCCTTGATCGTTGGGAACCGGAGCTGAATGAAGCCATAC
CAAACGACGAGCGTGACACCACGATGCCTGTAGCAATGGCAACAACGTTGCGCAAACTAT
TAACTGGCGAACTACTTACTCTAGCTTCCCGGCAACAATTAATAGACTGGATGGAGGCGG
ATAAAGTTGCAGGACCACTTCTGCGCTCGGCCCTTCCGGCTGGCTGGTTTATTGCTGATA
AATCTGGAGCCGGTGAGCGTGGGTCTCGCGGTATCATTGCAGCACTGGGGCCAGATGGTA
AGCCCTCCCGTATCGTAGTTATCTACACGACGGGGAGTCAGGCAACTATGGATGAACGAA
ATAGACAGATCGCTGAGATAGGTGCCTCACTGATTAAGCATTGGTAACTGTCAGACCAAG
TTTACTCATATATACTTTAGATTGATTTAAAACTTCATTTTTAATTTAAAAGGATCTAGG
```

TGAAGATCCTTTTTGATAATCTCATGCCATAACTTCGTATAATGTATGCTATACGAAGTT
ATGGCATGACCAAAATCCCTTAACGTGAGTTTTCGTTCCACTGAGCGTCAGACCCCGTAG
AAAAGATCAAAGGATCTTCTTGAGATCCTTTTTTTCTGCGCGTAATCTGCTGCTTGCAAA
CAAAAAAACCACCGCTACCAGCGGTGGTTTGTTTGCCGGATCAAGAGCTACCAACTCTTT
TTCCGAAGGTAACTGGCTTCAGCAGAGCGCAGATACCAAATACTGTCCTTCTAGTGTAGC
CGTAGTTAGGCCACCACTTCAAGAACTCTGTAGCACCGCCTACATACCTCGCTCTGCTAA
TCCTGTTACCAGTGGCTGCTGCCAGTGGCGATAAGTCGTGTCTTACCGGGTTGGACTCAA
GACGATAGTTACCGGATAAGGCGCAGCGGTCGGGCTGAACGGGGGGTTCGTGCACACAGC
CCAGCTTGGAGCGAACGACCTACACCGAACTGAGATACCTACAGCGTGAGCATTGAGAAA
GCGCCACGCTTCCCGAAGGGAGAAAGGCGGACAGGTATCCGGTAAGCGGCAGGGTCGGAA
CAGGAGAGCGCACGAGGGAGCTTCCAGGGGGAAACGCCTGGTATCTTTATAGTCCTGTCG
GGTTTCGCCACCTCTGACTTGAGCGTCGATTTTTGTGATGCTCGTCAGGGGGGCGGAGCC
TATGGAAAAACGCCAGCAACGCGGCCTTTTTACGGTTCCTGGCCTTTTGCTGGCCTTTTG
CTCACATGTTCTTTCCTGCGTTATCCCCTGATTCTGTGGATAACCGTATTACCGCCTTTG
AGTGAGCTGATACCGCTCGCCGCAGCCGAACGACCGAGCGCAGCGAGTCAGTGAGCGAGG
AAGCGGAAGAGCGCCCAATACGCAAACCGCCTCTCCCCGCGCGTTGGCCGATTCATTAAT
GCAGAGCTTGCAATTCGCGCGTTTTTCAATATTATTGAAGCATTTATCAGGGTTATTGTC
TCATGAGCGGATACATATTTGAATGTATTTAGAAAAATAAACAAATAGGGGTTCCGCGCA
CATTTCCCCGAAAAGTGCCACCTGACGTCTAAGAAACCATTATTATCATGACATTAACCT
ATAAAAATAGGCGTGATACGAGGCCCTTTCACTCATTAGGCACCCCAGGCTTTACACTTT
ATAGCTTCCGGCTCGTATAATGTGTGGAATTGTGAGCGGATAACAATTTCACACAGGAAA
CAGCATCGTGCAGGTCGTTACATAACTTACGGTAAATGGCCCGCCTGGCTGACCGCCCAA
CGACCCCCGCCCATTGACGTCAATAATGACGTATGTTCCCATAGTAACGCCAATAGGGAC
TTTCCATTGACGTCAATGGGTGGAGTATTTACGGTAAACTGCCCACTTGGCAGTACATCA
AGTGTATCATATGCCAAGTACGCCCCCTATTGACGTCAATGACGGTAAATGGCCCGCCTG
GCATTATGCCCAGTACATGACCTTATGGGACTTTCCTACTTGGCAGTACATCTACGTATT
AGTCATCGCTATTACCATGGTGATGCGGTTTTGGCAGTACATCAATGGGCGTGGATAGCG
GTTTGACTCACGGGGATTTCCAAGTCTCCACCCCATTGACGTCAATGGGAGTTTGTTTTG
GCACCAAAATCAACGGGACTTTCCAAAATGTCGTAACAACTCCGCCCCATTGACGCAAAT
GGGCGGTAGGCGTGTACGGTGGGAGGTCTATATAAGCAGAGCTCGTTTAGTGAACCGTCA
GATCGCCTGGAGACGCCATCCACGCTGTTTGACCTCCATAGAAGACACCGGGACCGATC
CAGCCTCCGGACTCTAGCCTAGGCTTTTGCAAAAAGCTATTTAGGTGACACTATAGAAGG
TACGCCTGCAGGTACC

---

[i] Li M et al. Organization of inorganic nanoparticles using biotin-streptavidin connectors. *Chem Mater.* 11, 23-6 (1999).